Interactions of the Amyloid-forming Peptide $PAP_{248-286}$ with Lipid Membranes: Relating Biophysical Mechanism to Biological Activities

Eleanor Vane

A dissertation

submitted in partial fulfillment of the

requirements for the degree of

Doctor of Philosophy

University of Washington

2021

Reading Committee:

Abhinav Nath, Chair

Kelly K. Lee

Libin Xu

Program Authorized to Offer Degree:

Medicinal Chemistry

University of Washington

Abstract

Interactions of the Amyloid-forming Peptide $PAP_{248-286}$ with Lipid Membranes: Relating Biophysical Mechanism to Biological Activities

Eleanor Vane

Chair of the Supervisory Committee:
Professor Abhinav Nath
Medicinal Chemistry

The interactions of membrane active peptides with lipid membranes are critical to both normal biological function and to the pathogenesis of many debilitating diseases. Antimicrobial peptides (AMPs), important players in innate immunity, provide protection from microbial infection through a variety of mechanisms, including membrane disruption and bacterial agglutination. On the other hand, lipid membranes can both accelerate amyloid formation and be the targets of toxic amyloid-forming peptides that have been implicated in diseases like Alzheimer's and Parkinson's diseases. Interestingly, AMPs and amyloid-forming peptides may exhibit some physiologically relevant functional overlap. Both classes of peptides share physicochemical properties that allow them to interact with lipid membranes in a similar manner. These interactions with lipid membranes are thought to drive each peptide's specific biological activities. This dissertation

explores the ways in which $PAP_{248-286}$, an amyloid-forming seminal peptide that also displays antimicrobial activities, interacts with lipid membranes. Chapter Two characterizes a co-assembly formed by $PAP_{248-286}$ and lipid membranes that is distinct from, and forms more readily than, *bona fide* $PAP_{248-286}$ amyloid fibrils. This species may account for some, if not all, of the biological activities attributed to its amyloid fibrils. Chapter Three elucidates the mechanism by which $PAP_{248-286}$ disrupts lipid membranes, perhaps providing an explanation for the lack of direct antimicrobial activity observed for the peptide, while furthering the development of a powerful fluorescence lifetime technique for use in future studies. Finally, Chapter Four includes additional experiments and open questions related to the membrane interactions and antimicrobial activity of $PAP_{248-286}$.

TABLE OF CONTENTS

LIST OF FIGURES

LIST OF TABLES

ACKNOWLEDGEMENTS

There are many people who have gotten me to the point I am at today. First, I would like to thank Abhi for allowing me to join his lab. I want to thank him for giving me the freedom to explore new directions in the lab and his patience and understanding over the years. Under his mentorship I have grown into an independent, thoughtful, and math-tolerating biophysicist. I would also like to thank my committee members, Lutz Maibaum, Brian Werth, Libin Xu, Kelly Lee, and Rachel Klevit for all of their insightful comments and advice during my time here.

I also really appreciate all of the advice, help, and discussions with all members of the Nath lab, past and present, inside and outside of lab. Eri Nakatani-Webster, David Ortiz, David Baggett, Shay Higgins, Hau Pham, Hayli Larsen, Supriya Ravishankar, Ellie James, and Elena Arroyo-Holland have been wonderful lab mates over the years. I would especially like to thank my lab-mate and friend, Hannah Baughman. We have had great discussions about science and life outside of science and I am so grateful for her advice, support, and friendship over the years.

I was lucky enough to be part of two great communities here at the University of Washington; the Biological Physics, Structure, and Design (BPSD) Program and the Department of Medicinal Chemistry. Being a member of the BPSD umbrella program has introduced me to new and exciting science and has taught me how to present my work to people outside of my field. I have also been happy to have Medicinal Chemistry as my home base. I have made many great friends, and always enjoyed running into them in the hallways and catching up.

To my BPSD and Biochemistry cohort friends: Domnita Rusnac, Bobby Langan, Lexi Walls, Rachel Hutto (and Sean Gillespie), and Gülsima Usluer, I cannot put into words how thankful I am for your friendships, encouragement, and support over the years. We have done so

many fun things together and your friendships have gotten me through. I feel so lucky to have started graduate school with such a great group of people and I am so honored and proud to call all of you my friends.

Despite being on the other side of the country, I am grateful to my family for all of the love, support, and encouragement they have shown me throughout my time here. First, I would like to thank my grandparents: Papa, Grandma Vane, Pappap, and Grandma Loechner. Thank you for always supporting my academic and extracurricular endeavors. I really wanted to make you all proud. To my mom, dad, and brother, Ethan. Ethan, thank you for introducing me to new things and challenging me on what I think is true. Mom and Dad, thank you for always being my biggest supporters in everything I choose to do. Thank you for your unconditional love, kindness, support, and always picking up your phone and talking to me when I need help or I need advice. I love you all and appreciate everything you have done for me.

Lastly I would like to thank my fiancée, Sean. Having you by my side this whole time has meant the world to me. Graduate school has been extremely challenging, and without your patience, support, and love I do not know if I would have made it through. You are my biggest cheerleader, my best friend, and my other half. Thank you for being you.

Chapter 1. INTRODUCTION

Abstract:

Membrane active peptides and proteins interact with lipid membranes, displaying a variety of membrane-disrupting and -remodeling activities. These activities can include induction of membrane leakage, vesicle fusion, and vesicle aggregation. This class of peptides has been historically subdivided into antimicrobial peptides (AMPs), amyloid-forming peptides, and cell-penetrating peptides based on their originally discovered function. However, the peptides in these sub-groups have similar physicochemical properties and activities that transcend the historic classification system (1). This chapter focuses on two of the subgroups of membrane active peptides; amyloid-forming peptides and AMPs. First, AMPs and amyloid-forming peptides will be introduced and the different ways in which these peptides interact with lipid membranes and the biological relevance of these interactions will be discussed. Next, the overlapping properties and activities of this diverse group of peptides will be explored. Finally, background on my primary model system, the membrane active peptide fragment of the protein prostatic acid phosphatase ($PAP_{248-286}$) found to form amyloid in seminal fluid that enhances HIV infectivity and displays antimicrobial activity will be given, followed by an overview of the work covered in this thesis.

1.1 ANTIMICROBIAL PEPTIDES

1.1.1 *Biological Significance of Antimicrobial Peptides*

Antimicrobial Peptides (AMPs), a class of membrane active peptides, are ubiquitous. 3,100 naturally occurring AMPs have been identified since 2020 and have been found in bacteria, plants, insects, and mammals (2). They often display broad-spectrum activity, with some AMPs displaying activity against multiple pathogens, including Gram-positive and -negative bacteria, enveloped viruses, fungi, and even unicellular parasites (2–7). In humans, AMPs play an important role in innate immunity, which is the immune system's first line of defense. As of 2014, 103 AMPs were identified in humans (3). They are commonly expressed in tissues or surfaces that are likely to be exposed to microbes, including the skin, mouth, intestine, and urinary tract by epithelial and immune cells. While some AMPs are constitutively expressed, most are inducible upon microbial infection (3, 8, 9). Many AMPs are expressed or stored as an inactive precursor and processed by proteases into their active form while other peptides are derived from large proteins with unrelated function (4, 9, 10).

There is great diversity amongst the sequences and structures of AMPs. AMPs can be separated into different classes based on their secondary structures: α-helical, β-sheet, αβ, and extended (3, 11). Short, linear α-helical AMPs are often disordered in solution and form their helical structure upon binding to a membrane. β-sheet AMPs are often stabilized by disulfide bonds, giving them more structure in solution, while αβ contain both secondary structures (3, 5). Extended AMPs are rich in structure breaking amino acids and are rare (5). Except for extended AMPs, each of the other categories of AMPs are represented in humans (3).

AMPs can provide protection through many different mechanisms. The most well-studied mechanism of action is their ability to disrupt membranes. The loss in membrane integrity can result in leakage of ions or larger molecules, resulting in bacterial killing (4, 5, 9, 12). Specific disruption models will be discussed more in depth in the next section. AMPs are also able to protect from infection through an agglutination mechanism. In this mechanism, AMPs agglutinate on or around pathogens, trapping them and disrupting their ability to infect their hosts. This can make pathogens better targets for processes such as phagocytosis (13–15). The formation of so-called "nanonets" were first described by Chu and colleagues for the intestinal human AMP α-defensin 6 (HD-6) (16, 17). The inducible insect AMP thanatin (18), human β-defensin 1 (hBD1) (19), and the oyster AMP big defensin-1 (BigDef1), also agglutinate some bacterial pathogens, with BigDef1 forming bactericidal nanonets (20). More recently, it has been suggested that the amyloid-forming peptide associated with Alzheimer's disease, amyloid-β (Aβ), is an AMP (21). At physiological concentrations, Aβ fibrils were shown to inhibit bacterial infection in worm and mouse models by agglutinating the pathogens and preventing their adherence to the host-cell (14, 22). Indeed, there is an interesting intersection between amyloid formation and antimicrobial activities that will be explored more in section 1.3 (23).

Additionally, some AMPs have been suggested to cross the cellular membrane of the pathogen and act on intracellular targets, including chaperone proteins, nucleic acids, and fungal mitochondria (5, 6, 24). Other AMPs exert immunomodulatory activities that include recruitment, activation, and differentiation of multiple different immune cells. Some AMPs, like the well-studied human AMP, LL-37, can translocate into innate immune cells, induce the expression of many different genes, including proinflammatory cytokines/chemokines, and modulate the response of the cell to different ligands. They have also been shown to influence subsequent

adaptive immunity (9, 25). Indeed a great strength of AMPs is that they can employ multiple mechanisms and work synergistically to fight infection (2, 5).

Aside from their prevalence in nature, there has also been great interest in AMPs because of their therapeutic potential against antibiotic resistant bacteria. The problem of multiple drug resistant bacterial strains continues to be a great threat to public health. The benefit of AMPs is that they often exert their action through mechanisms distinct from many other antibiotics, giving them activity against most antibiotic-resistant bacteria (9). It also seems to be harder for bacteria to develop resistance mechanisms to them (26). Some reasons that AMPs are associated with less antibacterial resistance is because they kill more quickly than antibiotics, their mechanisms are nonspecific, and they have a steep concentration dependence meaning that there is a smaller window of intermediate concentrations where bacteria can mutate and gain tolerance (2, 26, 27). However, it is possible for bacteria to develop resistance to AMPs through non-specific mechanisms such as secreting proteases, activating efflux pumps, increasing biofilm formation, and altering cell surface and lipid metabolism to decrease the negative charges on the bacterial envelope and lipid membrane (9, 27). Still there are many AMPs in clinical trials and there is interest in developing AMPs as a new class of antibiotics. In fact, some AMPs and AMP-like drugs have already been approved by the US Food and Drug Administration (FDA) (26). This includes gramicidin, which is one of the active ingredients in “Neosporin” eyedrops (28) and the lipopeptide antibiotic daptomycin (Cubicin®), which is approved to treat skin infections by gram-positive bacteria and *Staphylococcus aureus* bloodstream infections (29). Importantly, like natural AMPs, the mechanism of action given by the FDA for many of these drugs is their ability to porate or lyse membranes (30). However, challenges remain for therapeutic AMPs. They are more expensive to make, have short half-lives due to their pronounced degradation by proteases, and can have

problems with off-target cytotoxicity against host cells due to their non-specific membrane activities (26, 30). Because of this, development of AMPs pose interesting protein engineering challenges. Increasing our understanding of their mechanisms of action will be important in the rational design of effective AMPs.

1.1.2 *Antimicrobial Peptides and Lipid Membranes*

Despite the great amount of diversity, AMPs share some general features. They are small, with lengths usually ranging between 10 and 50 amino acid residues (1). They are also commonly cationic, with net charges ranging between +2 and +9 and an average net charge of +3.2. This is thought to help them distinguish between bacterial membranes, which contain mostly anionic lipids within the outer leaflet of their cytoplasmic membrane, and host cellular membranes, which contain mostly zwitterionic lipids in their cellular membrane (7, 24). About 30-50% of their amino acid residues are hydrophobic (7). Many of these hydrophobic residues are segregated to one face of the peptide while polar and charged residues are segregated to the other face, making these peptides amphipathic (1, 5, 11, 31). This property gives the peptides their ability to interact with membranes, which is, in many cases, critical to their antimicrobial activities.

While membrane disruption is expected to be important to the direct killing of bacteria by many AMPs, the exact mechanism for this activity is not known. Figure 1.1 highlights different models that have been proposed for this activity. Pores have been proposed to take on either a Barrel-Stave or Toroidal structure. In the Barrel-Stave model, the pore is lined with peptides oriented with their hydrophobic side interacting with the lipid tails and the hydrophilic side facing the aqueous pore (32, 33). This type of pore is more rare than toroidal pores, which are caused by the peptides bending the lipid headgroups into the membrane, making a peptide-lipid headgroup pore. Toroidal pores can be stable or chaotic, meaning that they form disorganized pores that cause

temporary leakage and then close (1, 33). The carpeting model occurs when the peptide adsorbs to the membrane, laying parallel to the plane of the membrane, and covering it. At very high (perhaps not physiologically relevant) concentrations, the carpeting mechanism can lead to disintegration of the membrane through a detergent-like mechanism, where the peptides strip lipids from the membrane into a peptide-lipid micelle (1, 5, 31, 32). Other proposed mechanisms of peptide-induced membrane disruption include leakage upon translocation of the AMP across the bilayer, such as in the sinking raft model, loss of membrane integrity through membrane thinning and weakening, and clustering of anionic lipids that results in the disturbance of lipid domains (5, 32).

Further complicating the determination of the peptide-induced leakage mechanism is the fact that this activity is highly dependent on the experimental conditions used to study the mechanism. The concentration of the peptide, the peptide:lipid ratio, the lipid composition of the membrane, the pH and ionic strength of the buffer, and the temperature can all affect the mechanism (1, 11). Many different mechanisms have been proposed in the literature for the same peptide. Another more general way to describe membrane disruption is to characterize it in terms of kinetic leakage mechanism rather than relying on assignment of a structural model. One common framework used for this characterization is the distinction between all-or-none and graded leakage mechanisms (11, 32). Weak and transient leakage events cause graded leakage, which results in partial leakage of all vesicles simultaneously. Strong leakage events cause all-or-none leakage, which results in complete leakage from some vesicles while other liposomes remain intact (34). These mechanisms will be discussed more in depth in Chapter 3.

1.2 AMYLOID-FORMING PEPTIDES

1.2.1 *Amyloid Background and Biology*

Amyloid-forming peptides are another class of membrane active peptides. In the strictest sense, amyloid is an ordered, insoluble fibrillar (fiber-like) protein aggregate with an extended β-sheet, or cross-β, structure. In this cross-β structure, β-sheets run perpendicular to the fibril axis and are stabilized by hydrogen bonds between peptide backbones of the β-sheets along the fibril axis and hydrophobic and electrostatic interactions between residue side chains perpendicular to the fibril axis (35, 36). Many different soluble proteins and peptides with diverse sequences and structures are capable of forming this thermodynamically favorable state (37). In fact, amyloid is such a ubiquitous structure in nature that it has been postulated that any polypeptide chain is capable of forming amyloid *in vitro* under optimized, potentially non-biologically relevant conditions (38, 39).

Amyloid formation is most often associated with neurodegeneration, as it has been implicated in neurodegenerative disorders including Alzheimer's and Parkinson's diseases. Amyloid formation has also been associated with as many as 40-50 other severe and debilitating diseases, such as type II diabetes and rheumatoid arthritis (40, 41). These diseases present a huge public health challenge. Alzheimer's disease alone, is currently the 6th leading cause of death in the U.S. and as many as 5.8 million people, 10% of the population over 65, has Alzheimer's (42). These numbers are expected to grow as the population ages. However, even though the prevalence of amyloid in disease has linked amyloid formation to disease and disorder, many recent studies have shown that amyloid can also play essential functional roles in prokaryotic organisms and beyond (43–45). For example, *E. coli* and *Salmonella* form extracellular amyloid known as curli,

which is a major component of their biofilm (44). In humans, many peptide hormones are stored in the secretory granules of the pituitary gland as amyloid (46). Amyloid has also been linked to the functioning of the innate immune system and antimicrobial activity, which will be discussed more extensively in section 1.3.

It should be noted that some caution should be exercised when reading the literature surrounding functional amyloids as some studies are not rigorous in their use of the term "amyloid". Experimentally, x-ray crystallography on microcrystals (36) and recent cryoEM (47, 48) structures that give atomic or near atomic resolution of amyloid fibers are the best methods for confirming and gaining a more detailed understanding about the fibril structure. Outside of these structural techniques, the gold standard to verify amyloid formation is through x-ray fiber diffraction, where two reflections, one at ~4.8 Å and one at ~8-11 Å, corresponds to the distance between β-sheets in parallel and perpendicular to the plane of the fibril, respectively (36). Additional biophysical techniques to assess the presence of amyloid includes fluorescence in the presence of the amyloid sensitive dye thioflavin T (ThT) *in vitro* or thioflavin S (ThS) *in situ*, "apple-green" birefringence of Congo red under polarized light, and visualization of fibrils by transmission electron microscopy or atomic force microscopy (49–51). Yet another technique to assess amyloid formation is to test whether the observed species is able to "seed" itself in a ThT kinetic assay. Since amyloid formation is a nucleation-dependent process, it displays sigmoidal formation kinetics. However, in the presence of a nucleating seeds, or amyloid fiber fragments, the lag phase is decreased or eliminated and the kinetics of amyloid formation will look more logarithmic (35). In some studies, a single technique, such as ThT binding or Congo red absorbance shift assay will be used to classify an aggregate or fibril as amyloid or "amyloid-like". While ThT is selective for amyloid, it is not specific and will fluoresce in the presence of other non-amyloid

aggregates (49, 52, 53). Further adding to the confusion, a 2017 study described the formation of cytotoxic, ThT-positive, "amyloid-like" fibers by the virulence peptide of *S. aureus*, phenol-soluble modulin PSMα3. However, the authors of this study showed that these "amyloid-like" fibrils had a cross-α structure, where α-helices, and not β-sheets, oriented perpendicular to the fibril axis are stacked along the fibril axis. Thus, this would expand the definition of amyloid to cover fibrils with a cross-α structure as well (54). Consensus in the amyloid community on terminology surrounding amyloid and amyloid-like may clarify these concepts for those outside of the field.

1.2.2 *Amyloid-forming Peptides and Lipid Membranes*

The interactions of amyloid-forming peptides with cellular membranes are important in the pathology of amyloid-associated diseases. Since amyloid is present in all amyloid-associated diseases, it was assumed to be the pathological species in these diseases. This may be the case for systemic amyloidoses, where large deposits of amyloid in vital organs and tissues hinder their proper functioning (35). However, in the case of other degenerative disorders, including type II diabetes and Alzheimer's disease, evidence (e.g., the lack of correlation between amyloid load and disease onset and severity) suggests that the amyloid fibrils are not the toxic species. This led to the "toxic oligomer theory" (55), which states that earlier oligomeric intermediates that are either on- or off- pathway to the formation of amyloid fibrils are the toxic species due to their interactions with and disruption of cellular membranes. In this theory, the amyloid fibrils are thought to either be inert or even protective (56). This is thought to be a common feature for all amyloids since early aggregates, but not fibrils, of proteins that are not associated with amyloid diseases are toxic in cell culture (57).

The toxicity of pre-amyloid oligomers is thought to be mediated by the ability of these oligomers to disrupt membranes and therefore cellular homeostasis. Localization of oligomers to membranes and their toxicity in cell culture has been described for many disease-associated amyloid-forming peptides (58–60). A particularly elegant study with the amyloid-forming protein from Parkinson's disease, alpha-synuclein (α-syn), showed that pre-formed α-syn oligomers bound to primary neuronal and SH-SY5Y cells, induced membrane disruption, and reduced cellular viability. An antibody developed to prevent the oligomer from binding to membranes, rescues membrane disruption and cell viability, thus linking oligomer-membrane interactions to cytotoxicity (61).

Isolating and identifying structural details about *the* pre-amyloid oligomer that is toxic has been challenging because oligomers are metastable, dynamic, display diverse morphologies, and polydisperse (62). Studies with artificial lipid membrane systems have been used to get a more detailed mechanistic understanding of how these peptides disrupt membranes. Formation of an oligomeric amyloid pore in the membrane has been proposed as an attractive explanation for the membrane disrupting activities of amyloid-forming peptides. Atomic force microscopy (AFM) and transmission electron microscopy have shown that many amyloid-forming peptides, including the Alzheimer's disease associated proteins, amyloid-beta (Aβ) and tau, Parkinson's disease associated protein, α-synuclein (α-syn), and the type II diabetes associated protein, amylin (or islet amyloid polypeptide, IAPP), form pore-like structures on a lipid membrane (63–65). These so-called annular protofibrils (APFs) behave similarly to an ion channel, allowing for the movement of ions across the membrane through the pores. Aβ APFs have been prepared in solution and visualized by EM, although interestingly they do not permeabilize membranes. Instead, prefibrillar oligomers are thought to undergo a structural rearrangement into APFs on the

membrane, resulting in permeabilization and toxicity (66). Pore-like structures have also been observed by isolation from or visualization on neuronal membranes in post-mortem tissue from brains affected by neurodegeneration (67–70).

In addition to the formation of a structured pore, the carpet mechanism, toroidal pore formation, and the detergent mechanism have been borrowed from the antimicrobial peptide literature and invoked to explain membrane disruption induced by amyloid-forming peptides. It has been suggested that IAPP forms toroidal pores (71, 72). However, a detergent mechanism, where the peptides disrupt membranes by disintegrating the vesicles, is the most commonly invoked mechanism for amyloid-forming peptides. It is often coupled with fibril growth on the membrane, with fibrils sometimes incorporating lipids or causing gross deformations, like distortion, tubulation, and fragmentation, of the membranes (73–81).

Conversely, lipid membranes are known to affect the formation of amyloid fibrils. Lipid membranes have demonstrated the ability to both catalyze and inhibit fibril formation of many amyloid-forming peptides including IAPP, Aβ, α-syn, and tau. This activity is complex as it is highly dependent on many factors, including membrane lipid composition and ratio of peptide to lipid. Membrane charge, thickness, and fluidity have all been suggested to affect amyloid formation kinetics (82, 83). For example, many studies have shown that lipid membranes with anionic lipids promote fibril formation (84–87). However, studies with IAPP and α-syn showed that while anionic liposomes generally promote aggregation, in some cases they can also inhibit aggregation depending on the peptide:lipid ratio (84, 86, 88). As described above, there is an interplay between amyloid formation and lipid membranes. Lipid membranes are not simply “observers” or “victims” of amyloid formation. Their involvement in the amyloid formation pathway can also alter the morphology of fibrils (80, 87–89). Amyloid-forming peptides can also

co-assemble with lipid membranes, resulting in structures such as stable peptide/lipid oligomers and lipopeptide nanoparticles that are distinct from canonical amyloid fibrils and have been proposed to be important in disease pathogenesis (90, 91).

1.3 Antimicrobial Amyloids

1.3.1 *Similarities Between Antimicrobial and Amyloid-forming Peptides*

AMPs and amyloid-forming peptides are subgroups of a class of peptides known as membrane active peptides. As was highlighted in the antimicrobial peptide section (1.1), these peptides can have very diverse sequences but share some physicochemical properties. Generally, these peptides are shorter than 50 amino acids (with α-syn and tau as exceptions) and many are disordered in solution but gain either α-helical or β-sheet structure upon binding to a membrane. However, the key property of membrane active peptides is that they are amphipathic, giving them the ability to bind membranes. There is also limited evidence that the toxic membrane-interacting oligomers of amphipathic amyloid-forming peptides, like Aβ and α-syn, are also amphipathic (61, 66). One of the functional outcomes of the amphipathic nature of these peptides is that they are able to disrupt membranes, often through pore formation. Another similarity is that, in many cases, pore formation by both AMPs and amyloid-forming peptides is enhanced in membranes containing anionic lipids (1). As can be appreciated from the previous sections detailing the interactions of AMPs (1.1.2) and amyloid-forming peptides (1.2.2), pore formation, as well as the preference to form pores in anionic membranes, is important to both antimicrobial and pathological activities of these peptides.

1.3.2 *Antimicrobial Activities of Amyloid-forming Peptides*

In addition to the similarities in physicochemical properties, membrane active peptides also display functional similarities. Direct antimicrobial activities, such as membrane disruption, have been assessed for many different amyloid-forming pathogens with a wide variety of bacteria. For example, α-syn and Aβ display membrane disrupting activities against bacteria and fungi (92, 93). Serum amyloid A 1 (SAA1)- known for forming amyloid in systemic amyloidosis- and IAPP display antimicrobial activity against gram-negative bacteria that is thought to be due to membrane disruption through pore formation (72, 94). Interestingly, the self-assembly of the dipeptide FF into nanotubes, which display most of the characteristics of amyloid (95), also display antimicrobial activity against gram-positive and -negative bacteria through a membrane disruption mechanism (96).

As with AMPs, amyloid-forming peptides may provide protection against microbial infection through various mechanisms. The capacity of amyloid-forming peptides to self-assemble into fibrillar structures, especially in the presence of anionic lipid membranes, allows for these peptides to utilize an agglutination antimicrobial mechanism. This was shown in a 2016 paper from the groups of Moir and Tanzi, which is perhaps one of the most pivotal papers to show a link between amyloid formation and antimicrobial activity. In this work, Kumar *et. al.* demonstrate that low, physiologically relevant concentrations of Aβ amyloid fibrils are able to protect mouse and worm models from infection by bacteria and fungi through an agglutination mechanism (97). Aβ is also active against viruses, as it has been shown to prevent the replication of herpes simplex virus 1 (HSV-1), though the mechanism was unknown (98). Moir, Tanzi, and colleagues showed that Aβ amyloid protects mice and cultured neuronal cells from HSV-1 infection through an agglutination mechanism. Interestingly, Aβ amyloid is seeded by the presence of HSV-1 and

herpesvirus 6A (HHV6A), which in turn provides protection against infection (99). This demonstrates the interplay between amyloid formation and subsequent toxicity of those amyloids observed in *in vitro* experiments. Additionally, semen-derived enhancer of viral infection (SEVI), an amyloid found in seminal fluid, also displays antimicrobial activities through a bacterial agglutination mechanism and will be discussed more in section 1.4.

It is worth mentioning that study of the antimicrobial activities of amyloid disease-associated peptides and the link between amyloid formation and innate immunity is a new and growing field. In Alzheimer's disease, a connection between Aβ amyloid and the oral and gut microbiome has been observed (100, 101). Multiple studies have also shown a connection between α-syn aggregation in Parkinson's disease with the gut microbiome and CNS viral infection (101, 102). These studies, along with others on the antimicrobial activities of these peptides have led to the hypothesis that Aβ and α-syn are AMPs with important roles in innate immunity. Furthermore, although many amyloids display antimicrobial activities, the exact mechanism has not yet been resolved. While this is an exciting area of research, it is beyond the scope of this thesis.

1.3.3 *Formation of Amyloid or Amyloid-like Fibrils by Antimicrobial Peptides*

Many known AMPs are able to form amyloid or amyloid-like fibrils and fibril formation is sometimes thought to be important to their antimicrobial mechanism. For example, a recent study from the Landau group discovered that uperin 3.5, an AMP from an Australian toadlet forms fibrils with cross-α structure in the presence of membrane mimetics and bacterial cells but is also able to form amyloid fibrils with a cross-β structure in the absence of membranes. Here, an interplay between amyloid formation and membrane disruption is observed again, as the bacteria are able to induce the formation of the cross-α fibrils, which are then toxic to the bacteria through membrane disruption (103). Membrane mimetics containing acidic phospholipids were shown to

induce the formation of amyloid-like fibrils and subsequent membrane disruption by the human AMP LL-37 (104). Further work by the Landau group showed that LL-37 can form helical fibrils that interact with bacteria and are essential to the antimicrobial activity of LL-37 against gram-positive *Micrococcus luteus* (105). ThT fluorescence was used to show eosinophil cationic peptide (ECP) forms amyloid-like fibrils in the presence of *E. coli*, leading to their agglutination and leakage (106). Other AMPs, including protegrin-1 (107), dermaseptin S9 (108), and even magainin were also suggested to form amyloid-like fibrils on membranes (109), although it is not known if fibril formation is important to their antimicrobial mechanism. Care should be taken when interpreting the AMPs as amyloid as discussed in section 1.2.1. Some studies on the formation of amyloids by AMPs use only ThT or congo red birefringence to assess the presence of amyloid. It is the best practice to use multiple techniques to confirm the presence of amyloid, and when this is not done, use of the term amyloid-like is more appropriate.

1.4 PROSTATIC ACID PHOSPHATASE ($PAP_{248-286}$)

1.4.1 *Biological Significance of $PAP_{248-286}$*

$PAP_{248-286}$ is an amyloid-forming peptide fragment of the protein prostatic acid phosphatase found in seminal fluid. It is a 39 amino acid residue, highly cationic peptide, carrying a net charge of +6 at a neutral pH (Figure 1.2a). It was identified in a screen of proteins and peptides from human semen as the predominant peptide to enhance HIV infection up to five orders of magnitude in a limiting dilution assay. The amyloid form of $PAP_{248-286}$ is thought to be responsible for increasing the infectivity of HIV and was therefore named semen-derived enhancer of viral infection (SEVI) (110). Subsequent studies have detected the presence of endogenous SEVI fibrils in semen (111) and enhancement of HIV infectivity by semen was found to be correlated to the

amount of SEVI in semen from donors, although there was a strong dependence on donor (112), perhaps due to different amyloid morphologies (113). The proposed mechanism for enhancement of HIV infectivity is that the negative charges on HIV particles and on the surface of target cells that normally cause repulsion are neutralized by the highly cationic, bridge-like SEVI amyloid fibrils, similar to what has been observed for the cationic polymer, polybrene (114). The cationic nature of these amyloid fibrils is important, as mutation of all of the positively charged residues in the sequence to alanine (SEVIala), while still forming amyloid, lacks the ability to enhance HIV infection. Anionic polymers also inhibit infection enhancement and prevent binding to virions (115). Later studies have found that amyloids formed by other cationic peptides released from a major component of semen, the semenogelin proteins, are also able to enhance HIV infection, suggesting a common mechanism (116).

In addition to HIV, SEVI amyloid has also been shown to enhance the infectivity of other enveloped viruses, including cytomegalovirus (117), herpes simplex virus type 1 and 2 (118), and Ebola virus (119). In addition to its virus enhancing activities, more recent studies have suggested that SEVI may be a functional amyloid. One study has suggested that SEVI could function as an antimicrobial amyloid since seminal fluid has antibacterial properties and contains many other AMPs that protect the infection-prone urogenital tract (120). Indeed, SEVI displays antimicrobial activity against *E. coli* and *S. aureus*, not through direct membrane disruption but through an agglutination mechanism. It was shown to increase their uptake and the uptake of *N. gonorrhoeae* into macrophages, and decrease bacterial load of *N. gonorrhoeae* in a mouse model of intravaginal infection. In addition, SEVI amyloid increases the release of cytokines from macrophages, displaying immunomodulatory behaviors similar to *bona fide* AMPs (121). As has been previously discussed in section 1.3, amyloid-forming peptides can display a range of antimicrobial activities

so it is therefore possible that this could be a native function of SEVI amyloid. Another study found that SEVI amyloid fibrils bind, entrap, and immobilize spermatozoa. This study also found that the other seminal amyloids enhance the uptake of sperm, especially those that have been damaged, into macrophages, resulting in their clearance. These results suggest that SEVI and other cationic seminal amyloids may play a role in reproduction (122).

1.4.2 *$PAP_{248-286}$-Lipid Membrane Interactions*

While all of the biological activities associated with $PAP_{248-286}$ are assigned to its amyloid form, SEVI, much remains unknown about the $PAP_{248-286}$ monomer. As with other amyloid-forming peptides that may also be AMPs, peptide-lipid interactions are expected to be important to its activities. The Ramamoorthy group has shown that the disordered $PAP_{248-286}$ monomer (Figure 1.2b) forms a partial α-helix with about 30% α-helical content by circular dichroism (CD) spectroscopy upon membrane binding (123). Further NMR studies by this group with SDS micelles showed that while $PAP_{248-286}$ gains more α-helical content in the micelles, it remains largely unstructured and does not penetrate very far into the hydrophobic core of the micelle (124). This superficial binding was supported by work from the same group by differential scanning calorimetry (DSC) (125). However, additional NMR studies with trifluoroethanol (TFE), a commonly used membrane mimetic that is used to stabilize underlying secondary structures (126), showed that $PAP_{248-286}$ forms an amphipathic α-helix with a larger membrane-binding interface (Figure 1.2c and 1.2d) (123). Results from sum frequency generation vibrational spectroscopy are in agreement with the NMR structures obtained with TFE (127). Therefore, despite different techniques and membrane mimetics yielding different amounts of α-helical content, $PAP_{248-286}$ always becomes more α-helical upon membrane binding. In addition to binding, an early study by Brender *et. al.* showed that $PAP_{248-286}$ causes aggregation of anionic lipid membranes and

membranes at an acidic pH in a concentration-dependent manner, disrupts membranes in an electrostatic-dependent manner, and promotes the fusion of lipid membranes (123). However, more in-depth details about how specifically $PAP_{248-286}$ causes the aggregation of and disrupts lipid membranes remains unclear.

1.5 THESIS OVERVIEW

The overall goal of this thesis is to interrogate the diverse ways in which amyloid-forming peptides like $PAP_{248-286}$ interact with membranes, in order to get a better mechanistic understanding of their distinct biological activities. Peptide-induced membrane disruption and lipid-induced peptide assembly are relevant to both the beneficial actions of antimicrobial peptides and to the pathogenesis of amyloid-associated diseases. Chapter Two explores the capacity of lipid membranes to catalyze the assembly of $PAP_{248-286}$, which results in the subsequent agglutination of these membranes. It shows that under certain conditions $PAP_{248-286}$ is able to quickly form co-assemblies with lipids that are distinct from *bona fide* SEVI amyloid and may be important to the *in vivo* activities ascribed to SEVI. Chapter Three elucidates the kinetic mechanism of membrane disruption by $PAP_{248-286}$ monomer while also improving the methodology of fluorescence lifetime analysis to account for sample heterogeneity. Understanding the mechanism of membrane disruption could be used to explain why $PAP_{248-286}$ lacks direct antimicrobial activity and to better understand the activity of other pathological amyloid-forming peptides, AMPs, and cytolytic antibiotics. Chapter Four discusses open questions related to the membrane interactions and antimicrobial activity of $PAP_{248-286}$ that could be interesting avenues of research to pursue in the future.

1.6 FIGURES

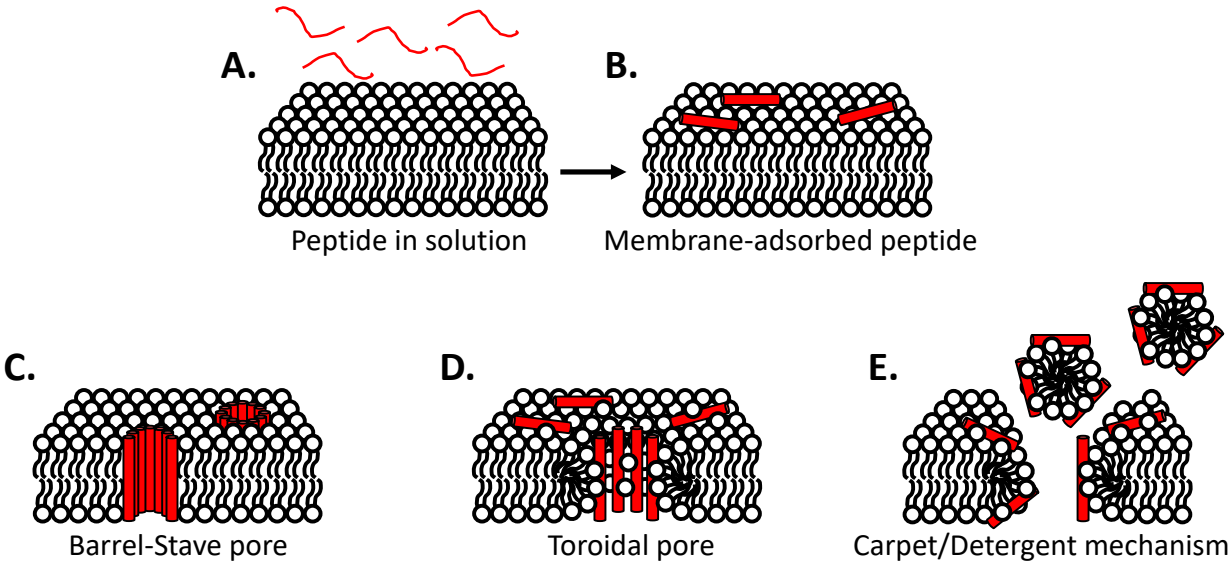

Figure 1.1: Illustration of different membrane disruption mechanisms.

In solution linear α-helical AMPS (red squiggles) are often disordered (A). Upon binding and adsorption to the membrane, the AMP forms an α-helix (red cylinder) (B) and can form Barrel-Stave (C) or toroidal (D) pores. At high AMP concentrations, the carpet/detergent mechanism can strip lipids from the bilayer into AMP/lipid micelles (E).

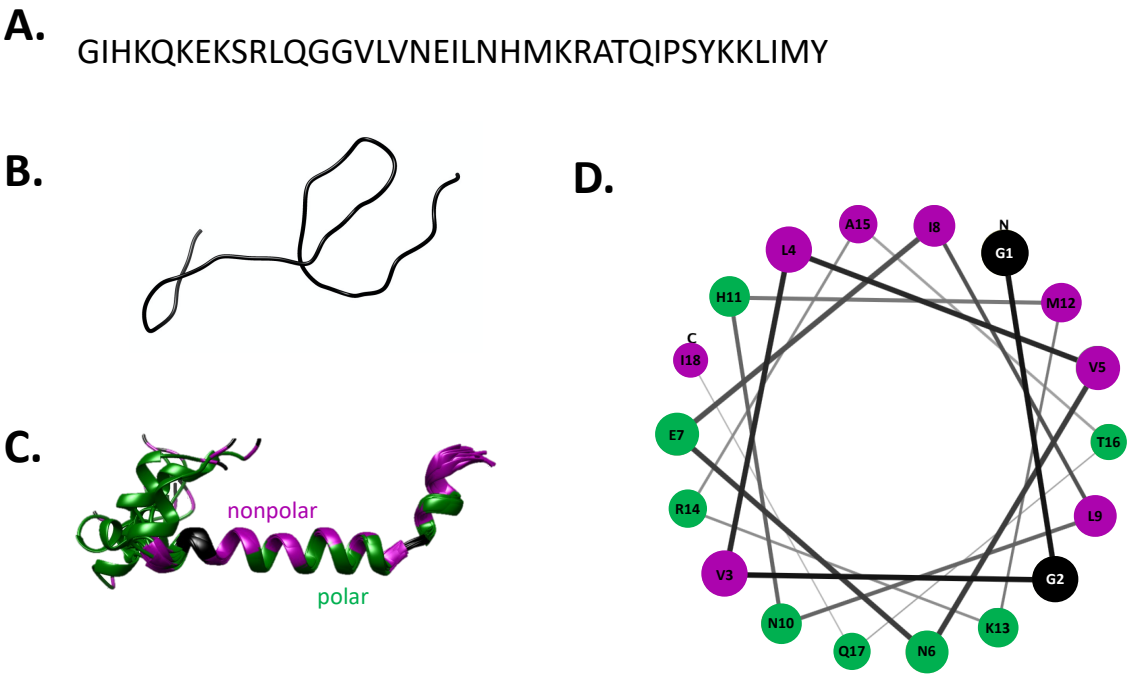

Figure 1.2: $PAP_{248-286}$ sequence and structure.

(A) The sequence of $PAP_{248-286}$. (B) A frame from an MD simulation of $PAP_{248-286}$ in solution. (C) High resolution NMR structure of $PAP_{248-286}$ in 50% TFE (PDB: 2L77) from (123). (D) Helical wheel projection of the amphipathic section of $PAP_{248-286}$ starting from G260 and ending with I277. In (C) and (D), the nonpolar residues are purple, polar residues are green, and proline and glycine residues are black. The helical wheel diagram was created with MPEx (128) and modified to match the color scheme.

1.7 REFERENCES

1. Last, N.B., D.E. Schlamadinger, and A.D. Miranker. 2013. A common landscape for membrane active peptides. *Protein Sci.* 22:870–882.
2. Lazzaro, B.P., M. Zasloff, and J. Rolff. 2020. Antimicrobial peptides: Application informed by evolution. *Science (80-.).* 368.
3. Wang, G. 2014. Human antimicrobial peptides and proteins. *Pharmaceuticals*. 7:545–594.
4. Zasloff, M. 2002. Antimicrobial Peptides of Multicellular Organisms. *Nature*. 415:389–395.
5. Nguyen, L.T., E.F. Haney, and H.J. Vogel. 2011. The expanding scope of antimicrobial peptide structures and their modes of action. *Trends Biotechnol.* 29:464–472.
6. Hancock, R.E. 2001. Cationic peptides: Effectors in innate immunity and novel antimicrobials. *Lancet Infect. Dis.* 1:156–164.
7. Hancock, R.E.W., K.L. Brown, and N. Mookherjee. 2006. Host defence peptides from invertebrates - emerging antimicrobial strategies. *Immunobiology*. 211:315–322.
8. Hancock, R.E.W., and G. Diamond. 2000. The role of cationic antimicrobial peptides in innate host defences. *Trends Microbiol.* 8:402–410.
9. Lai, Y., and R.L. Gallo. 2009. AMPed up immunity: how antimicrobial peptides have multiple roles in immune defense. *Trends Immunol.* 30:131–141.
10. Zhang, L.J., and R.L. Gallo. 2016. Antimicrobial peptides. *Curr. Biol.* 26:R14–R19.
11. Guha, S., J. Ghimire, E. Wu, and W.C. Wimley. 2019. Mechanistic Landscape of Membrane-Permeabilizing Peptides. *Chem. Rev.* 119:6040–6085.
12. Shai, Y. 1999. Mechanism of the binding, insertion and destabilization of phospholipid bilayer membranes by ??-helical antimicrobial and cell non-selective membrane-lytic peptides. *Biochim. Biophys. Acta - Biomembr.* 1462:55–70.
13. White, M.R., R. Kandel, S. Tripathi, D. Condon, L. Qi, J. Taubenberger, and K.L. Hartshorn. 2014. Alzheimer's associated β-Amyloid protein inhibits influenza a virus and modulates viral interactions with phagocytes. *PLoS One*. 9:1–9.
14. Kumar, D.K. V., S.H. Choi, K.J. Washicosky, W.A. Eimer, S. Tucker, J. Ghofrani, A. Lefkowitz, G. McColl, L.E. Goldstein, R.E. Tanzi, and R.D. Moir. 2016. Amyloid-B peptide protects against microbial infection in mouse and worm models of Alzheimers disease. *Sci. Transl. Med.* 8:340ra72-340ra72.
15. Tecle, T., M.R. White, D. Gantz, E.C. Crouch, and K.L. Hartshorn. 2007. Human neutrophil defensins increase neutrophil uptake of influenza A virus and bacteria and modify virus-induced respiratory burst responses. *J. Immunol.* 178:8046–52.
16. Chu, H., M. Pazgier, G. Jung, S. Nuccio, P.A. Castillo, M.F. de Jong, M.G. Winter, S.E. Winter, J. Wehkamp, B. Shen, N.H. Salzman, M.A. Underwood, R.M. Tsolis, G.M. Young, W. Lu, R.I. Lehrer, A.J. Bäumler, and C.L. Bevins. 2012. Human α-defensin 6 promotes mucosal innate immunity through self-assembled peptide nanonets. *Science*. 337:477–81.
17. Chairatana, P., and E.M. Nolan. 2014. Molecular basis for self-assembly of a human host-defense peptide that entraps bacterial pathogens. *J. Am. Chem. Soc.* 136:13267–13276.

18. Fehlbaum, P., P. Bulet, S. Chernysh, J.P. Briand, J.P. Roussel, L. Letellier, C. Hetru, and J.A. Hoffmann. 1996. Structure-activity analysis of thanatin, a 21-residue inducible insect defense peptide with sequence homology to frog skin antimicrobial peptides. *Proc. Natl. Acad. Sci.* 93:1221–1225.

19. Raschig, J., D. Mailänder-Sánchez, A. Berscheid, J. Berger, A.A. Strömstedt, L.F. Courth, N.P. Malek, H. Brötz-Oesterhelt, and J. Wehkamp. 2017. Ubiquitously expressed Human Beta Defensin 1 (hBD1) forms bacteria-entrapping nets in a redox dependent mode of action. *PLoS Pathog.* 13:1–18.

20. Loth, K., A. Vergnes, C. Barreto, S.N. Voisin, H. Meudal, J. Da Silva, A. Bressan, N. Belmadi, E. Bachère, V. Aucagne, C. Cazevielle, H. Marchandin, R.D. Rosa, P. Bulet, L. Touqui, A.F. Delmas, and D. Destoumieux-Garzón. 2019. The ancestral N-terminal domain of big defensins drives bacterially triggered assembly into antimicrobial nanonets. *MBio*. 10.

21. Moir, R.D., R. Lathe, and R.E. Tanzi. 2018. The antimicrobial protection hypothesis of Alzheimer's disease. *Alzheimer's Dement.* 14:1602–1614.

22. Spitzer, P., M. Condic, M. Herrmann, T.J. Oberstein, M. Scharin-mehlmann, D.F. Gilbert, O. Friedrich, T. Grömer, J. Kornhuber, R. Lang, and J.M. Maler. 2016. Amyloidogenic amyloid- β -peptide variants induce microbial agglutination and exert antimicrobial activity. *Sci. Rep.* 6:1–11.

23. Kagan, B.L., H. Jang, R. Capone, F. Teran Arce, S. Ramachandran, R. Lal, and R. Nussinov. 2012. Antimicrobial properties of amyloid peptides. *Mol. Pharm.* 9:708–717.

24. Wang, G., B. Mishra, K. Lau, T. Lushnikova, R. Golla, and X. Wang. 2015. Antimicrobial peptides in 2014. *Pharmaceuticals*. 8:123–150.

25. Hancock, R.E.W., E.F. Haney, and E.E. Gill. 2016. The immunology of host defence peptides: Beyond antimicrobial activity. *Nat. Rev. Immunol.* 16:321–334.

26. Koo, H.B., and J. Seo. 2019. Antimicrobial peptides under clinical investigation. *Pept. Sci.* 111.

27. Joo, H.S., C.I. Fu, and M. Otto. 2016. Bacterial strategies of resistance to antimicrobial peptides. *Philos. Trans. R. Soc. B Biol. Sci.* 371.

28. Usmani, S.S., G. Bedi, J.S. Samuel, S. Singh, S. Kalra, P. Kumar, A.A. Ahuja, M. Sharma, A. Gautam, and G.P.S. Raghava. 2017. THPdb: Database of FDA-approved peptide and protein therapeutics. *PLoS One*. 12:e0181748.

29. 2017. Cubicin: Highlights of Prescribing Information. Whitehouse Station, NJ: Merck Sharp and Dohme Corp.

30. Chen, C.H., and T.K. Lu. 2020. Development and Challenges of Antimicrobial Peptides for Therapeutic Applications. *Antibiotics*. 9:24.

31. Bahar, A.A., and D. Ren. 2013. Antimicrobial peptides. *Pharmaceuticals*. 6:1543–1575.

32. Almeida, P.F., and A. Pokorny. 2012. Interactions of antimicrobial peptides with lipid bilayers. .

33. Wimley, W.C. 2010. Describing the mechanism of antimicrobial peptide action with the interfacial activity model. *ACS Chem. Biol.* 5:905–917.

34. Braun, S., Š. Pokorná, R. Šachl, M. Hof, H. Heerklotz, and M. Hoernke. 2018. Biomembrane Permeabilization: Statistics of Individual Leakage Events Harmonize the Interpretation of Vesicle Leakage. *ACS Nano*. 12:813–819.

35. Knowles, T.P.J., M. Vendruscolo, and C.M. Dobson. 2014. The amyloid state and its association with protein misfolding diseases. *Nat. Rev. Mol. Cell Biol.* 15:384–96.

36. Sawaya, M.R., S. Sambashivan, R. Nelson, M.I. Ivanova, S.A. Sievers, M.I. Apostol, M.J. Thompson, M. Balbirnie, J.J.W. Wiltzius, H.T. McFarlane, A.Ø. Madsen, C. Riekel, and D. Eisenberg. 2007. Atomic structures of amyloid cross-beta spines reveal varied steric zippers. *Nature*. 447:453–7.

37. Baldwin, A.J., T.P.J. Knowles, G.G. Tartaglia, A.W. Fitzpatrick, G.L. Devlin, S.L. Shammas, C.A. Waudby, M.F. Mossuto, S. Meehan, S.L. Gras, J. Christodoulou, S.J. Anthony-Cahill, P.D. Barker, M. Vendruscolo, and C.M. Dobson. 2011. Metastability of Native Proteins and the Phenomenon of Amyloid Formation. *J. Am. Chem. Soc*. 133.

38. Chiti, F., P. Webster, N. Taddei, A. Clark, M. Stefani, G. Ramponi, and C.M. Dobson. 1999. Designing conditions for in vitro formation of amyloid protofilaments and fibrils. *Proc. Natl. Acad. Sci. U. S. A.* 96:3590–4.

39. Dobson, C.M. 2004. Principles of Dobson, C. M. (2004). Principles of protein folding, misfolding and aggregation. *Semin. Cell Dev. Biol.* 15:3–16.

40. Pulawski, W., U. Ghoshdastider, V. Andrisano, and S. Filipek. 2012. Ubiquitous amyloids. *Appl. Biochem. Biotechnol.* 166:1626–1643.

41. Lu, J., Y. Yu, I. Zhu, Y. Cheng, and P.D. Sun. 2014. Structural mechanism of serum amyloid A-mediated inflammatory amyloidosis. *Proc. Natl. Acad. Sci. U. S. A.* 111:5189–94.

42. 2020. 2020 Alzheimer's disease facts and figures. *Alzheimer's Dement.* 16:391–460.

43. Fowler, D.M., A. V. Koulov, C. Alory-Jost, M.S. Marks, W.E. Balch, and J.W. Kelly. 2006. Functional amyloid formation within mammalian tissue. *PLoS Biol.* 4:0100–0107.

44. Fowler, D.M., A. V. Koulov, W.E. Balch, and J.W. Kelly. 2007. Functional amyloid - from bacteria to humans. *Trends Biochem. Sci.* 32:217–224.

45. Bergman, P., N.R. Roan, U. Römling, C.L. Bevins, and J. Münch. 2016. Amyloid formation: functional friend or fearful foe? *J. Intern. Med.* 280:139–152.

46. Maji, S.K., M.H. Perrin, M.R. Sawaya, S. Jessberger, K. Vadodaria, R.A. Rissman, P.S. Singru, K.P.R. Nilsson, R. Simon, D. Schubert, D. Eisenberg, J. Rivier, P. Sawchenko, W. Vale, and R. Riek. 2009. Functional amyloids as natural storage of peptide hormones in pituitary secretory granules. *Science (80-.).* 325:328–32.

47. Falcon, B., W. Zhang, A.G. Murzin, G. Murshudov, H.J. Garringer, R. Vidal, R.A. Crowther, B. Ghetti, S.H.W. Scheres, and M. Goedert. 2018. Structures of filaments from Pick's disease reveal a novel tau protein fold. *Nature*. 561:137–140.

48. Fitzpatrick, A.W.P., B. Falcon, S. He, A.G. Murzin, G. Murshudov, H.J. Garringer, R.A. Crowther, B. Ghetti, M. Goedert, and S.H.W. Scheres. 2017. Cryo-EM structures of tau filaments from Alzheimer ' s disease. *Nat. Publ. Gr.* 547:185–190.

49. Biancalana, M., and S. Koide. 2010. Molecular mechanism of Thioflavin-T binding to amyloid fibrils. *Biochim. Biophys. Acta - Proteins Proteomics*. 1804:1405–1412.

50. Howie, A.J., D.B. Brewer, D. Howell, and A.P. Jones. 2008. Physical basis of colors seen in Congo red-stained amyloid in polarized light. *Lab. Investig.* 88:232–242.

51. Nilsson, M.R. 2004. Techniques to study amyloid fibril formation in vitro. *Methods*. 34:151–160.

52. Baughman, H.E.R., A.F. Clouser, R.E. Klevit, and A. Nath. 2018. HspB1 and Hsc70 chaperones engage distinct tau species and have different inhibitory effects on amyloid formation. *J. Biol. Chem.* 293:2687–2700.

53. Wolfe, L.S., M.F. Calabrese, A. Nath, D. V Blaho, A.D. Miranker, and Y. Xiong. 2010. Protein-induced photophysical changes to the amyloid indicator dye thioflavin T. *Proc. Natl. Acad. Sci. U. S. A.* 107:16863–16868.

54. Tayeb-fligelman, E., O. Tabachnikov, A. Moshe, O. Goldshmidt-tran, M.R. Sawaya, N. Coquelle, J. Colletier, and M. Landau. The cytotoxic Staphylococcus aureus. 22–25.

55. Hebda, J. a, and A.D. Miranker. 2009. The interplay of catalysis and toxicity by amyloid intermediates on lipid bilayers: insights from type II diabetes. *Annu. Rev. Biophys.* 38:125–52.

56. Caughey, B., and P.T. Lansbury. 2003. Protofibrils , Pores, Fibrils, and Neurodegeneration: Separating the Responsible Protein Aggregates from The Innocent Bystanders. *Annu. Rev. Neurosci.* 26:267–298.

57. Bucciantini, M., E. Giannoni, F. Chiti, F. Baroni, L. Formigli, J. Zurdo, N. Taddei, G. Ramponi, C.M. Dobson, and M. Stefani. 2002. Inherent toxicity of aggregates implies a common mechanism for protein misfolding diseases. *Nature*. 416:507–511.

58. Kayed, R., E. Head, J.L. Thompson, T.M. McIntire, S.C. Milton, C.W. Cotman, and C.G. Glabel. 2003. Common structure of soluble amyloid oligomers implies common mechanism of pathogenesis. *Science (80-.).* 300:486–489.

59. Lambert, M.P., K.L. Viola, B.A. Chromy, L. Chang, T.E. Morgan, J. Yu, D.L. Venton, G.A. Krafft, C.E. Finch, and W.L. Klein. 2001. Vaccination with soluble Aβ oligomers generates toxicity-neutralizing antibodies. *J. Neurochem.* 79:595–605.

60. Flach, K., I. Hilbrich, A. Schiffmann, U. Gärtner, M. Krüger, M. Leonhardt, H. Waschipky, L. Wick, T. Arendt, and M. Holzer. 2012. Tau oligomers impair artificial membrane integrity and cellular viability. *J. Biol. Chem.* 287:43223–43233.

61. Cascella, R., M. Perni, S.W. Chen, G. Fusco, C. Cecchi, M. Vendruscolo, F. Chiti, C.M. Dobson, and A. De Simone. 2019. Probing the Origin of the Toxicity of Oligomeric Aggregates of α-Synuclein with Antibodies. *ACS Chem. Biol.* 14:1352–1362.

62. Ke, P.C., R. Zhou, L.C. Serpell, R. Riek, T.P.J. Knowles, H.A. Lashuel, E. Gazit, I.W. Hamley, T.P. Davis, M. Fändrich, D.E. Otzen, M.R. Chapman, C.M. Dobson, D.S. Eisenberg, and R. Mezzenga. 2020. Half a century of amyloids: Past, present and future. *Chem. Soc. Rev.* 49:5473–5509.

63. Quist, A., I. Doudevski, H. Lin, R. Azimova, D. Ng, B. Frangione, B. Kagan, J. Ghiso, and R. Lal. 2005. Amyloid ion channels: a common structural link for protein-misfolding disease. *Proc. Natl. Acad. Sci. U. S. A.* 102:10427–10432.

64. Patel, N., S. Ramachandran, R. Azimov, B.L. Kagan, and R. Lal. 2015. Ion Channel Formation by Tau Protein: Implications for Alzheimer's Disease and Tauopathies. *Biochemistry*. 54:7320–7325.

65. Lee, J., Y.H. Kim, F. Arce, A.L. Gillman, H. Jang, B.L. Kagan, R. Nussinov, J. Yang, and R. Lal. 2017. Amyloid β Ion Channels in a Membrane Comprising Brain Total Lipid Extracts. *ACS Chem. Neurosci.* 8:1348–1357.

66. Kayed, R., A. Pensalfini, L. Margol, Y. Sokolov, F. Sarsoza, E. Head, J. Hall, and C. Glabe. 2009. Annular protofibrils area structurally and functionally distinct type of amyloid oligomer. *J. Biol. Chem.* 284:4230–4237.

67. Lasagna-Reeves, C. a, U. Sengupta, D. Castillo-Carranza, J.E. Gerson, M. Guerrero-Munoz, J.C. Troncoso, G.R. Jackson, and R. Kayed. 2014. The formation of tau pore-like structures is prevalent and cell specific: possible implications for the disease phenotypes. *Acta Neuropathol. Commun.* 2:56.

68. Butterfield, S.M., and H.A. Lashuel. 2010. Amyloidogenic protein-membrane interactions: Mechanistic insight from model systems. *Angew. Chemie - Int. Ed.* 49:5628–5654.

69. Inoue, S. 2008. In situ Aβ pores in AD brain are cylindrical assembly of Aβ protofilaments. *Amyloid*. 15:223–233.

70. Pountney, D.L., R. Lowe, M. Quilty, J.C. Vickers, N.H. Voelcker, and W.P. Gai. 2004. Annular alpha-synuclein species from purified multiple system atrophy inclusions. *J. Neurochem.* 90:502–512.

71. Last, N.B., E. Rhoades, and A.D. Miranker. 2011. Islet amyloid polypeptide demonstrates a persistent capacity to disrupt membrane integrity. *Proc Natl Acad Sci U S A*. 108:9460–9465.

72. Last, N.B., and A.D. Miranker. 2013. Common mechanism unites membrane poration by amyloid and antimicrobial peptides. *Proc. Natl. Acad. Sci. U. S. A.* 110:6382–7.

73. Sparr, E., M.F.M. Engel, D. V. Sakharov, M. Sprong, J. Jacobs, B. De Kruijff, J.W.M. Höppener, and J. Antoinette Killian. 2004. Islet amyloid polypeptide-induced membrane leakage involves uptake of lipids by forming amyloid fibers. *FEBS Lett.* 577:117–120.

74. Sciacca, M.F.M., S.A. Kotler, J.R. Brender, J. Chen, D.K. Lee, and A. Ramamoorthy. 2012. Two-step mechanism of membrane disruption by Aβ through membrane fragmentation and pore formation. *Biophys. J.* 103:702–710.

75. Engel, M.F.M., L. Khemtémourian, C.C. Kleijer, H.J.D. Meeldijk, J. Jacobs, A.J. Verkleij, B. De Kruijff, J.A. Killian, and J.W.M. Höppener. 2008. Membrane damage by human islet amyloid polypeptide through fibril growth at the membrane. *Proc. Natl. Acad. Sci. U. S. A.* 105:6033–6038.

76. Gellermann, G.P., T.R. Appel, A. Tannert, A. Radestock, P. Hortschansky, V. Schroeckh, C. Leisner, T. Lütkepohl, S. Shtrasburg, C. Röcken, M. Pras, R.P. Linke, S. Diekmann, and M. Fändrich. 2005. Raft lipids as common components of human extracellular amyloid fibrils. *Proc. Natl. Acad. Sci. U. S. A.* 102:6297–6302.

77. Mizuno, N., J. Varkey, N.C. Kegulian, B.G. Hegde, N. Cheng, R. Langen, and A.C. Steven. 2012. Remodeling of lipid vesicles into cylindrical micelles by α-synuclein in an extended α-helical conformation. *J. Biol. Chem.* 287:29301–29311.

78. Jayaraman, S., D.L. Gantz, C. Haupt, and O. Gursky. 2017. Serum amyloid A forms stable oligomers that disrupt vesicles at lysosomal pH and contribute to the pathogenesis of reactive amyloidosis. *Proc. Natl. Acad. Sci. U. S. A.* 114:E6507–E6515.

79. Kollmer, M., K. Meinhardt, C. Haupt, F. Liberta, M. Wulff, J. Linder, L. Handl, L. Heinrich, C. Loos, M. Schmidt, T. Syrovets, T. Simmet, P. Westermark, G.T. Westermark, U. Horn, V. Schmidt, P. Walther, and M. Fändrich. 2016. Electron tomography reveals the fibril structure and lipid interactions in amyloid deposits. *Proc. Natl. Acad. Sci. U. S. A.* 113:5604–5609.

80. Hellstrand, E., A. Nowacka, D. Topgaard, S. Linse, and E. Sparr. 2013. Membrane Lipid Co-Aggregation with α-Synuclein Fibrils. *PLoS One*. 8:1–10.

81. Bode, D.C., M. Freeley, J. Nield, M. Palma, and J.H. Viles. 2019. Amyloid-β oligomers have a profound detergent-like effect on lipid membrane bilayers, imaged by atomic force and electron microscopy. *J. Biol. Chem.* 294:7566–7572.

82. Henderson, J.M., N.S. Iyengar, K.L.H. Lam, E. Maldonado, T. Suwatthee, I. Roy, A.J. Waring, and K.Y.C. Lee. 2019. Beyond electrostatics: Antimicrobial peptide selectivity and the influence of cholesterol-mediated fluidity and lipid chain length on protegrin-1 activity. *Biochim. Biophys. Acta - Biomembr.* 1861:182977.

83. Korshavn, K.J., C. Satriano, Y. Lin, R. Zhang, M. Dulchavsky, A. Bhunia, M.I. Ivanova, Y.H. Lee, C. La Rosa, M.H. Lim, and A. Ramamoorthy. 2017. Reduced lipid bilayer thickness regulates the aggregation and cytotoxicity of amyloid-β. *J. Biol. Chem.* 292:4638–4650.

84. Viennet, T., M.M. Wördehoff, B. Uluca, C. Poojari, H. Shaykhalishahi, D. Willbold, B. Strodel, H. Heise, A.K. Buell, W. Hoyer, and M. Etzkorn. 2018. Structural insights from lipid-bilayer nanodiscs link α-Synuclein membrane-binding modes to amyloid fibril formation. *Commun. Biol.* 1:1–12.

85. Zhao, H., E.K.J. Tuominen, and P.K.J. Kinnunen. 2004. Formation of amyloid fibers triggered by phosphatidylserine-containing membranes. *Biochemistry*. 43:10302–10307.

86. Knight, J.D., and A.D. Miranker. 2004. Phospholipid catalysis of diabetic amyloid assembly. *J. Mol. Biol.* 341:1175–1187.

87. Elbaum-Garfinkle, S., T. Ramlall, and E. Rhoades. 2010. The role of the lipid bilayer in tau aggregation. *Biophys. J.* 98:2722–2730.

88. Terakawa, M.S., Y.H. Lee, M. Kinoshita, Y. Lin, T. Sugiki, N. Fukui, T. Ikenoue, Y. Kawata, and Y. Goto. 2018. Membrane-induced initial structure of α-synuclein control its amyloidogenesis on model membranes. *Biochim. Biophys. Acta - Biomembr.* 1860:757–766.

89. Falke, M., J. Victor, M.M. Wördehoff, A. Peduzzo, T. Zhang, G.F. Schröder, A.K. Buell, W. Hoyer, and M. Etzkorn. 2019. α-Synuclein-derived lipoparticles in the study of α-Synuclein amyloid fibril formation. *Chem. Phys. Lipids*. 220:57–65.

90. Ait-Bouziad, N., G. Lv, A.L. Mahul-Mellier, S. Xiao, G. Zorludemir, D. Eliezer, T. Walz, and H.A. Lashuel. 2017. Discovery and characterization of stable and toxic Tau/phospholipid oligomeric complexes. *Nat. Commun.* 8:1–16.

91. Varkey, J., N. Mizuno, B.G. Hegde, N. Cheng, A.C. Steven, and R. Langen. 2013. A-Synuclein Oligomers With Broken Helical Conformation Form Lipoprotein Nanoparticles. *J. Biol. Chem.* 288:17620–17630.

92. Park, S.C., J.C. Moon, S.Y. Shin, H. Son, Y.J. Jung, N.H. Kim, Y.M. Kim, M.K. Jang, and J.R. Lee. 2016. Functional characterization of alpha-synuclein protein with antimicrobial activity. *Biochem. Biophys. Res. Commun.* 478:924–928.

93. Soscia, S.J., J.E. Kirby, K.J. Washicosky, S.M. Tucker, M. Ingelsson, B. Hyman, M.A. Burton, L.E. Goldstein, S. Duong, R.E. Tanzi, and R.D. Moir. 2010. The Alzheimer's disease-associated amyloid beta-protein is an antimicrobial peptide. *PLoS One*. 5:1–10.

94. Hirakura, Y., I. Carreras, J.D. Sipe, and B.L. Kagan. 2002. Channel formation by serum amyloid A: a potential mechanism for amyloid pathogenesis and host defense. *Amyloid*. 9:13–23.

95. Brahmachari, S., Z.A. Arnon, A. Frydman-Marom, E. Gazit, and L. Adler-Abramovich. 2017. Diphenylalanine as a Reductionist Model for the Mechanistic Characterization of β-Amyloid Modulators. *ACS Nano*. 11:5960–5969.

96. Schnaider, L., S. Brahmachari, N.W. Schmidt, B. Mensa, S. Shaham-Niv, D. Bychenko, L. Adler-Abramovich, L.J.W. Shimon, S. Kolusheva, W.F. Degrado, and E. Gazit. Self-assembling dipeptide antibacterial nanostructures with membrane disrupting activity. .

97. Kumar D.K., Choi S.H., Washicosky K.J., Eimer W.A., Tucker S., Ghofrani J., Lefkowitz A., McColl G., Goldstein L.E., Tanzi R.E., M.R.D. 2016. Amyloid-β peptide protects against microbial infection in mouse and worm models of Alzheimer's disease. *Sci. Transl. Med.* 8:340ra72.

98. Bourgade, K., H. Garneau, G. Giroux, A.Y. Le Page, C. Bocti, G. Dupuis, E.H. Frost, and T. Fülöp. 2015. β-Amyloid peptides display protective activity against the human Alzheimer's disease-associated herpes simplex virus-1. *Biogerontology*. 16:85–98.

99. Eimer, W.A., D.K. Vijaya Kumar, N.K. Navalpur Shanmugam, A.S. Rodriguez, T. Mitchell, K.J. Washicosky, B. György, X.O. Breakefield, R.E. Tanzi, and R.D. Moir. 2018. Alzheimer's Disease-Associated β-Amyloid Is Rapidly Seeded by Herpesviridae to Protect against Brain Infection. *Neuron*. 99:56-63.e3.

100. Dominy, S.S., C. Lynch, F. Ermini, M. Benedyk, A. Marczyk, A. Konradi, M. Nguyen, U. Haditsch, D. Raha, C. Griffin, L.J. Holsinger, S. Arastu-Kapur, S. Kaba, A. Lee, M.I. Ryder, B. Potempa, P. Mydel, A. Hellvard, K. Adamowicz, H. Hasturk, G.D. Walker, E.C. Reynolds, R.L.M. Faull, M.A. Curtis, M. Dragunow, and J. Potempa. 2019. Porphyromonas gingivalis in Alzheimer's disease brains: Evidence for disease causation and treatment with small-molecule inhibitors. *Sci. Adv.* 5:eaau3333.

101. Fung, T.C., C.A. Olson, and E.Y. Hsiao. 2017. Interactions between the microbiota, immune and nervous systems in health and disease. *Nat. Neurosci.* 20:145–155.

102. Beatman, E.L., A. Massey, K.D. Shives, K.S. Burrack, M. Chamanian, T.E. Morrison, and J.D. Beckham. 2016. Alpha-Synuclein Expression Restricts RNA Viral Infections in the Brain. *J. Virol.* 90:2767–2782.

103. Salinas, N., E. Tayeb-Fligelman, M.D. Sammito, D. Bloch, R. Jelinek, D. Noy, I. Usón, and M. Landau. The amphibian antimicrobial peptide uperin 3.5 is a cross-α/cross-β chameleon functional amyloid. .

104. Sood, R., Y. Domanov, M. Pietiäinen, V.P. Kontinen, and P.K.J. Kinnunen. 2008. Binding of LL-37 to model biomembranes: Insight into target vs host cell recognition. *Biochim. Biophys. Acta - Biomembr.* 1778:983–996.

105. Engelberg, Y., and M. Landau. 2020. The Human LL-37(17-29) antimicrobial peptide reveals a functional supramolecular structure. *Nat. Commun.* 11:1–10.

106. Torrent, M., D. Pulido, M.V. Nogués, and E. Boix. 2012. Exploring New Biological Functions of Amyloids: Bacteria Cell Agglutination Mediated by Host Protein Aggregation. *PLoS Pathog.* 8:1–8.

107. Jang, H., F.T. Arce, M. Mustata, S. Ramachandran, R. Capone, R. Nussinov, and R. Lal. 2011. Antimicrobial protegrin-1 forms amyloid-like fibrils with rapid kinetics suggesting a functional link. *Biophys. J.* 100:1775–1783.

108. Auvynet, C., C. El Amri, C. Lacombe, F. Bruston, J. Bourdais, P. Nicolas, and Y. Rosenstein. 2008. Structural requirements for antimicrobial versus chemoattractant activities for dermaseptin S9. *FEBS J.* 275:4134–4151.

109. Zhao, H., A. Jutila, T. Nurminen, S.A. Wickström, J. Keski-Oja, and P.K.J. Kinnunen. 2005. Binding of endostatin to phosphatidylserine-containing membranes and formation of amyloid-like fibers. *Biochemistry*. 44:2857–2863.

110. Münch, J., E. Rücker, L. Ständker, K. Adermann, C. Goffinet, M. Schindler, S. Wildum, R. Chinnadurai, D. Rajan, A. Specht, G. Giménez-Gallego, P.C. Sánchez, D.M. Fowler, A. Koulov, J.W. Kelly, W. Mothes, J.C. Grivel, L. Margolis, O.T. Keppler, W.G. Forssmann, and F. Kirchhoff. 2007. Semen-Derived Amyloid Fibrils Drastically Enhance HIV Infection. *Cell*. 131:1059–1071.

111. Usmani, S.M., O. Zirafi, J.A. Muller, N.L. Sandi-Monroy, J.K. Yadav, C. Meier, T. Weil, N.R. Roan, W.C. Greene, P. Walther, K.P. Nilsson, P. Hammarstrom, R. Wetzel, C.D. Pilcher, F. Gagsteiger, M. Fandrich, F. Kirchhoff, and J. Munch. 2014. Direct visualization of HIV-enhancing endogenous amyloid fibrils in human semen. *Nat Commun*. 5:3508.

112. Kim, K.-A., M. Yolamanova, O. Zirafi, N.R. Roan, L. Staendker, W.-G. Forssmann, A. Burgener, N. Dejucq-Rainsford, B.H. Hahn, G.M. Shaw, W.C. Greene, F. Kirchhoff, and J. Münch. 2010. Semen-mediated enhancement of HIV infection is donor-dependent and correlates with the levels of SEVI. *Retrovirology*. 7:55.

113. Qiao, X., J. Jeon, A.L. Cole, J.O. Matos, S. Bautista, J. Castillo, I. Hung, Z. Gan, S.A. Tatulian, A.M. Cole, and B. Chen. 2015. Morphology-dependent HIV-enhancing effect of semen-derived enhancer of viral infection. *Biophys. J.* 108:2028–2037.

114. Davis, H.E., M. Rosinski, J.R. Morgan, and M.L. Yarmush. 2004. Charged Polymers Modulate Retrovirus Transduction via Membrane Charge Neutralization and Virus Aggregation. *Biophys. J.* 86:1234–1242.

115. Roan, N.R., J. Münch, N. Arhel, W. Mothes, J. Neidleman, A. Kobayashi, K. Smith-McCune, F. Kirchhoff, and W.C. Greene. 2009. The cationic properties of SEVI underlie its ability to enhance human immunodeficiency virus infection. *J. Virol.* 83:73–80.

116. Roan, N.R., H. Liu, S.M. Usmani, J. Neidleman, J.A. Müller, A. Avila-Herrera, A. Gawanbacht, O. Zirafi, S. Chu, M. Dong, S.T. Kumar, J.F. Smith, K.S. Pollard, M. Fändrich, F. Kirchhoff, J. Münch, H.E. Witkowska, and W.C. Greene. 2014. Liquefaction of semen generates and later degrades a conserved semenogelin peptide that enhances HIV infection. *J. Virol.* 88:7221–34.

117. Tang, Q., N.R. Roan, and Y. Yamamura. 2013. Seminal Plasma and Semen Amyloids Enhance Cytomegalovirus Infection in Cell Culture. *J. Virol.* 87:12583–12591.

118. Torres, L., T. Ortiz, and Q. Tang. 2015. Enhancement of herpes simplex virus (HSV) infection by seminal plasma and semen amyloids implicates a new target for the prevention of HSV infection. *Viruses*. 7:2057–2073.

119. Bart, S.M., C. Cohen, J.M. Dye, J. Shorter, and P. Bates. 2018. Enhancement of Ebola virus infection by seminal amyloid fibrils. *Proc. Natl. Acad. Sci.* 115:7410–7415.

120. Nguyen, P. V, J.K. Kafka, V.H. Ferreira, K. Roth, and C. Kaushic. 2014. Innate and adaptive immune responses in male and female reproductive tracts in homeostasis and following HIV infection. *Cell. Mol. Immunol.* 11:410–27.

121. Easterhoff, D., F. Ontiveros, L.R. Brooks, Y. Kim, B. Ross, J.N. Silva, J.S. Olsen, C. Feng, D.J. Hardy, P.M. Dunman, and S. Dewhurst. 2013. Semen-derived enhancer of viral infection (SEVI) binds bacteria, enhances bacterial phagocytosis by macrophages, and can protect against vaginal infection by a sexually transmitted bacterial pathogen. *Antimicrob. Agents Chemother.* 57:2443–2450.

122. Roan, N.R., N. Sandi-Monroy, N. Kohgadai, S.M. Usmani, K.G. Hamil, J. Neidleman, M. Montano, L. Ständker, A. Röcker, M. Cavrois, J. Rosen, K. Marson, J.F. Smith, C.D. Pilcher, F. Gagsteiger, O. Sakk, M. O'Rand, P. V Lishko, F. Kirchhoff, J. Münch, and W.C. Greene. 2017. Semen amyloids participate in spermatozoa selection and clearance. *Elife*. 6:1–22.

123. Brender, J.R., R.P.R. Nanga, N. Popovych, R. Soong, P.M. Macdonald, and A. Ramamoorthy. 2011. The amyloidogenic SEVI precursor, PAP248-286, is highly unfolded in solution despite an underlying helical tendency. *Biochim. Biophys. Acta - Biomembr.* 1808:1161–1169.

124. Nanga, R.P.R., J.R. Brender, S. Vivekanandan, N. Popovych, and A. Ramamoorthy. 2009. NMR structure in a membrane environment reveals putative amyloidogenic regions of the SEVI precursor peptide PAP248-286. *J. Am. Chem. Soc.* 131:17972–17979.

125. Brender, J.R., K. Hartman, L.M. Gottler, M.E. Cavitt, D.W. Youngstrom, and A. Ramamoorthy. 2009. Helical conformation of the SEVI precursor peptide PAP248-286, a dramatic enhancer of HIV infectivity, promotes lipid aggregation and fusion. *Biophys. J.* 97:2474–2483.

126. Roccatano, D., G. Colombo, M. Fioroni, and A.E. Mark. 2002. Mechanism by which 2,2,2-trifluoroethanol/water mixtures stabilize secondary-structure formation in peptides: A molecular dynamics study. *Proc. Natl. Acad. Sci. U. S. A.* 99:12179–12184.

127. Nguyen, K.T. 2016. In Situ Investigation of Peptide–Lipid Interaction Between PAP248–286 and Model Cell Membranes. *J. Membr. Biol.*

128. Snider, C., S. Jayasinghe, K. Hristova, and S.H. White. 2009. MPEx: A tool for exploring membrane proteins. *Protein Sci.* 18:2624–2628.

Chapter 2. RAPID FORMATION OF PEPTIDE/LIPID CO-AGGREGATES BY THE AMYLOIDOGENIC SEMINAL PEPTIDE $PAP_{248-286}$

[Reproduced with permission from Vane, E.W., S. He, L. Maibaum, and A. Nath. 2020. Rapid Formation of Peptide/Lipid Coaggregates by the Amyloidogenic Seminal Peptide $PAP_{248-286}$. *Biophysical Journal.* 119:924–938.]

Abstract:

Protein/lipid co-assembly is an understudied phenomenon that is important to the function of antimicrobial peptides as well as the pathological effects of amyloid. Here we study the co-assembly process of $PAP_{248-286}$, a seminal peptide that displays both amyloid-forming and antimicrobial activity. $PAP_{248-286}$ is a peptide fragment of prostatic acid phosphatase and has been reported to form amyloid fibrils, known as semen-derived enhancer of viral infection (SEVI), that enhance the viral infectivity of HIV. We find that in addition to forming amyloid, $PAP_{248-286}$ much more readily assembles with lipid vesicles into peptide/lipid co-aggregates that resemble amyloid fibrils in some important ways but are a distinct species. The formation of these $PAP_{248-286}$/lipid co-aggregates, which we term "messicles", is controlled by the peptide:lipid (P:L) ratio and by the lipid composition. The optimal P:L ratio is around 1:10 and at least 70% anionic lipid is required for co-aggregate formation. Once formed, messicles are not disrupted by subsequent changes in P:L ratio. We propose that messicles form through a polyvalent assembly mechanism, where a critical surface density of $PAP_{248-286}$ on liposomes enables peptide-mediated particle bridging into larger species. Even at ~50-fold lower $PAP_{248-286}$ concentrations, messicles form at least 10-fold

faster than amyloid fibrils. It is therefore possible that some or all of the biological activities assigned to SEVI, the amyloid form of $PAP_{248-286}$, could instead be attributed to a $PAP_{248-286}$/lipid co-aggregate. More broadly speaking, this work could provide a potential framework for the discovery and characterization of non-amyloid peptide/lipid co-aggregates by other amyloid-forming proteins and antimicrobial peptides.

2.1 Statement of Significance

$PAP_{248-286}$, a fragment of prostatic acid phosphatase, forms amyloid thought to enhance the infectivity of many viruses, including HIV. This amyloid, termed semen-derived enhancer of viral infection (SEVI), has been assigned responsibility for all of $PAP_{248-286}$'s biological activities, while the monomer is thought to be inactive. However, SEVI formation is quite slow and requires very high concentrations of $PAP_{248-286}$. Here, we show that $PAP_{248-286}$ can instead assemble much more rapidly with lipid membranes to form another species that is mechanistically and morphologically distinct from both monomer and SEVI amyloid. We have characterized this species, which could play a role in the biological activities currently ascribed to SEVI. Additionally, similar mechanisms of peptide/lipid co-assembly could apply to other biologically important systems.

2.2 Introduction

Protein self-assembly is ubiquitous in biology – essential for normal function and yet also underlying major diseases. Structural filaments like actin and tubulin microtubules, whose assembly is critical for proper cellular motility, morphology, and transport and division, have been the topics of study for over 70 years (1, 2). Aggregation into amyloid filaments, a hallmark of disorders such as Alzheimer's disease (AD), Parkinson's disease (PD) and type II diabetes, has

been studied for even longer (3). Self-assembly can serve to regulate metabolism, as the assembly of metabolic enzymes into fibers or foci in response to different environmental conditions can affect their activity (4). Recently, there has also been a resurgence of interest in the co-assembly of proteins with other macromolecules (often charged polymers) into phase-separated liquid droplets inside the cell. These membrane-less organelles are able to self-assemble and condense in a tunable, regulated fashion, so as to carry out specific metabolic or regulatory functions (5–7). Here, we focus on a related but distinct phenomenon, which is relevant both to amyloid pathology and to the function of antimicrobial peptides: the co-assembly of proteins and lipids into mixed aggregates.

There are as many as 40–50 amyloid-associated diseases, wherein diverse proteins misfold and self-assemble into characteristic insoluble, fibrillar, β-sheet-rich aggregates (8). Toxicity is generally thought to result from the remodeling or disruption of biological membranes by pre-fibrillar or non-fibrillar oligomeric states rather than mature amyloid fibrils (9–11). Amyloid fibrils are relatively inert once formed, and can play important functional roles including in bacterial biofilm structure, peptide hormone storage, and protection against microbial infection (12–17). Lipid membranes are known to both promote and inhibit aggregation of many amyloid-forming peptides, including islet amyloid polypeptide (IAPP), amyloid β (Aβ), α-synuclein (AS), and tau, in a manner dependent on membrane lipid composition and peptide:lipid ratio (18–27). The effect of lipid is often biphasic, with an optimal peptide:lipid ratio above *or* below which fibril formation is hindered (19, 21, 23). Lipid involvement in amyloidogenesis can alter fibril morphology, yield lipid-containing aggregates, or cause membrane fragmentation and remodeling that can lead to cytotoxicity (21, 22, 24–39). Notably, co-assemblies distinct from canonical amyloid fibrils, such

as stable peptide/lipid oligomers and lipopeptide nanoparticles, have been proposed to be important in pathogenesis (40, 41).

Antimicrobial peptides (AMPs) are an important component of pathogen defense in animals, plants, fungi, and bacteria. Aside from immunomodulatory behavior, AMPs provide protection from pathogens by binding to and penetrating or disrupting pathogen membranes and/or by self-assembling around pathogens and causing them to agglutinate (17, 42–50). Intriguingly, AMPs and amyloid-forming peptides share important physicochemical and functional features (13, 51) and can form strikingly similar fibrillar structures (47, 50), leading to growing interest in the idea that pathological amyloid-forming peptides, like Aβ, confer protection against microbial pathogens (17, 52, 53). Agglutination of pathogens disrupts their ability to infect their hosts and makes them better targets for processes such as phagocytosis (17, 54, 55). Moreover, in certain systems such as plant defensins and designed peptidomimetics, aggregate formation with lipids or on membranes is required for membrane disruption and can improve their antimicrobial activity (56, 57). It is becoming increasingly evident that biologically important modes of antimicrobial activity depend on the co-assembly of AMPs with bacterial membranes.

Thus peptide/lipid co-assembly into a variety of aggregates, some similar to canonical amyloid fibrils and some distinct, impacts both amyloid pathology and AMP activity. These co-assemblies can resemble those formed by other cationic polypeptides or polycations with anionic lipid membranes (58–63). However, comparatively little is understood about the physical processes that drive peptide/lipid co-assembly as a phenomenon in its own right, distinct from amyloid formation. Here, we address this question using a peptide fragment of the seminal protein prostatic acid phosphatase ($PAP_{248\text{-}286}$) as a model system. $PAP_{248\text{-}286}$ is a 39-residue amyloid-forming peptide with a net charge of +6 at neutral pH, that also displays antimicrobial activity

through bacterial agglutination (64). It has been shown to aggregate anionic lipid membranes and membranes at an acidic pH in a concentration dependent manner (65). While disordered in solution, $PAP_{248-286}$ gains α-helical structure upon binding to membranes, with the amount of α-helical content depending on the model membrane used (65–68). Binding to the membrane surface is thought to be driven by electrostatic interactions, as $PAP_{248-286}$ does not seem to penetrate the hydrophobic core of the bilayer to the same extent as other amyloid-forming peptides (65, 67).

$PAP_{248-286}$ forms amyloid fibrils that are thought to be responsible for the large enhancement of HIV infectivity observed in seminal fluid, and thus called semen-derived enhancer of viral infection (SEVI) (69). SEVI fibrils have also been shown to enhance cytomegalovirus, herpes simplex virus type 1 and 2, and Ebola virus infection as well as participate in sperm quality control and agglutinate bacteria (64, 70–73). The exact mechanism for these activities is still unknown, but it has been hypothesized that the SEVI amyloid can act like a bridge, trapping or bringing cells together (74). All of $PAP_{248-286}$'s biological activity has been assigned to SEVI amyloid. However, monomeric $PAP_{248-286}$ (i.e., not assembled into SEVI fibrils) also enhances HIV infection in the presence of seminal fluid (69). Seminal fluid is a complex matrix that contains many different macromolecules including membrane-enclosed extracellular vesicles (EVs), proteins, lipids, and in the case of viral infection, viral particles (75–77). We therefore believe that it is possible that peptide/lipid membrane co-aggregation of the $PAP_{248-286}$ monomer with a component of seminal fluid could be an important, yet overlooked mechanism for $PAP_{248-286}$'s activity.

We show that, in addition to forming amyloid, $PAP_{248-286}$ assembles more readily with lipids into large co-aggregates that we have termed "messicles". In some ways, $PAP_{248-286}$ messicles are reminiscent of other peptide/lipid and polycation/lipid assemblies (58–63). Using

liposomes as a model lipid membrane system and a variety of biophysical techniques including negative stain electron microscopy (EM), dynamic light scattering (DLS), circular dichroism (CD) spectroscopy, and fluorescence correlation spectroscopy (FCS), we explore the particular regime under which messicles form. These experiments reveal that messicle formation is dependent on the $PAP_{248-286}$:lipid ratio, as well as lipid membrane composition. Finally, we describe a formation mechanism by which polyvalent $PAP_{248-286}$-mediated interactions drive co-aggregation at an optimal peptide:lipid ratio. The assembly process and the conditions that favor it may be important in explaining the diverse biological activities observed for $PAP_{248-286}$.

2.3 METHODS

2.3.1 *Materials:*

1-palmitoyl-2-oleoyl-glycero-3-phosphocholine (POPC) and 1-palmitoyl-2-oleoyl-sn-glycero-3-phospho-(1'-rac-glycerol) (POPG) were purchased from Avanti Polar Lipids, Inc. (Alabaster, AL) as a powder. Unless specified otherwise, all other reagents were purchased from Thermo Fisher Scientific (Waltham, MA) and were ACS reagent grade or better.

2.3.2 *$PAP_{248-286}$ preparation:*

Synthetic $PAP_{248-286}$ (sequence: GIHKQKEKSRLQGGVLVNEILNHMKRATQIPSYKK LIMY) was purchased from Genscript (Piscataway, NJ) and New England Peptides (Gardner, MA). Peptide was dissolved as received in either Tris buffer (20 mM Tris, 100 mM NaCl, pH 7.4) or filtered milliQ water, flash frozen, and stored at -80°C. The final concentration of $PAP_{248-286}$ stock was determined by absorbance at 280 nm.

2.3.3 *Liposome preparation:*

LUVs were prepared with either 100% POPG, 7:3 POPG:POPC (mol:mol), 1:1 POPG:POPC (mol:mol), or 100% POPC (Avanti Polar Lipids). Stock lipid solutions were prepared from purchased lipid powders at 19 mg/mL in chloroform and stored at -20°C for 6 months-1 year. The total phosphorous content of the lipid stocks was verified using the "Determination of Total Phosphorus" analytical procedure outlined by Avanti Polar Lipids (78–80) adapted for a Biotek Synergy HTX multi-mode plate reader (Winooski, VT). Briefly, phosphate standards (Sigma-Aldrich, St. Louis, MO) and lipid stocks in chloroform or liposomes were ashed in 225 μL of 8.9 N sulfuric acid, followed by addition of 75 μL of concentrated hydrogen peroxide (30%) and another ashing step as in Reference 78. Samples were then cooled and diluted with 1.95 mL milliQ water, and 50 μL were added to a clear bottom plate. 100 μL of a solution containing 0.5% ammonium molybdate, 3% ascorbic acid, and 0.5 M hydrochloric acid was added to each well and incubated for 5 minutes, followed by the addition of 100 μL of a solution containing 2% sodium-metaarsenite, 2% citric acid, and 2% glacial acetic acid as in Reference 80. The absorbance was measured at 850 nm after a 15 minute incubation at 37°C on a Biotek Synergy HTX multi-mode plate reader (Winooski, VT).

Liposomes were prepared by measuring the appropriate amount of each lipid stock in chloroform and evaporating bulk chloroform with nitrogen gas to form lipid films. These films were left under vacuum for 1-14 hours and then hydrated with Tris buffer. The rehydrated lipid film was then subjected to 10 freeze-thaw cycles, followed by 23 passes through a mini-extruder (Avanti Polar Lipids) with a 0.1 μm polycarbonate membrane (Avanti Polar Lipids). The final concentration of LUVs was determined using the total phosphorous assay, described earlier. Liposomes doped with 3,3'-dihexadecyloxacarbocyanine perchlorate ($DiOC_{16}(3)$) were prepared

in the same manner, except $DiOC_{16}(3)$ in dimethyl sulfoxide (DMSO) was added to the lipid stocks in chloroform at a molar ratio of 1:135 (dye:lipid). Liposomes filled with calcein (MP Biomedicals, Irvine, CA) were prepared in the same manner as unfilled liposomes but were hydrated with the Tris buffer containing 7 mM calcein and 0.3 mM EDTA. The liposomes were then separated from remaining unencapsulated calcein using a 5 mL HiTrap desalting column (GE Healthcare, Marlborough, MA) and eluted with the Tris buffer without calcein. All preparation steps were performed at room temperature.

2.3.4 *Microscope imaging:*

1:1, 1:10, and 1:25 $PAP_{248-286}$:POPG samples were prepared by incubating 10 μM $PAP_{248-286}$ with 10, 100, or 250 μM POPG liposomes for 30 minutes at room temperature. Samples were placed on a coverslip and imaged at room temperature using the 20x objective of a home built, inverted Zeiss Axio Observer D1 confocal microscope (Carl Zeiss Microscopy, White Plains, NY) equipped with an Andor iXon3 camera (Oxford Instruments, South Windsor, CT) and Micro-Manager open source microscopy software (81, 82). Images were further processed with Fiji software (83).

For dissociation in the presence of excess $PAP_{248-286}$, $PAP_{248-286}$ was centrifuged at 21100*g* at 4°C for 30 minutes in a Sorvall Legend 21R microcentrifuge (Thermo Fisher Scientific) to remove any aggregates. "Dissociation" and "dilution control" samples were prepared by incubating 20 μL of 20 μM messicles (20 μM $PAP_{248-286}$ and 200 μM POPG liposomes in Tris buffer) for 4 minutes. After incubation, 80 μL of 20 μM $PAP_{248-286}$ was added to the "dissociation" sample, bringing the final concentration to 20 μM $PAP_{248-286}$ and 40 μM POPG. 80 μL of Tris buffer was added to the "dilution control", bringing the final concentration to 4 μM $PAP_{248-286}$ and 40 μM POPG. The "fresh 1:2" sample was prepared as a concentration match to the dissociation

sample. It was prepared by incubating 100 µL of 20 µM $PAP_{248-286}$ with 40 µM POPG for 4 minutes. For dissociation in the presence of excess POPG, the "dissociation" sample was prepared by adding 80 µL of 200 µM POPG to 20 µL of 20 µM messicle, bringing the final concentration to 4 µM $PAP_{248-286}$ and 200 µM POPG. The concentration match for this dissociation sample, called "fresh 1:50", was prepared by incubating 100 µL of 4 µM $PAP_{248-286}$ with 200 µM POPG for 4 minutes. All samples were prepared, incubated, and imaged at room temperature. Samples were imaged 4, 30, and 60 minutes after the final solution was prepared. Data presented are representative of seven different images collected throughout different *x* and *y* coordinates in the sample droplet.

2.3.5 *Electron microscopy:*

300 mesh carbon-coated copper grids (Electron Microscopy Sciences, Hatfield, PA) were glow-discharged on an EMS100x (Electron Microscopy Sciences) and spotted with 3 µL of buffer, 22 µM $PAP_{248-286}$, 10 µM $PAP_{248-286}$ with 10 µM POPG, 100 µM POPG, 100 µM 7:3 POPG:POPC, or 250 µM POPG, and 250 µM POPG liposomes after a 4 minute incubation at room temperature, and SEVI amyloid diluted to 0.01 mg/mL. Samples adsorbed for 60 seconds, then were blotted by filter paper, rinsed with filtered milliQ water, blotted with filter paper, and then floated on a drop of NanoW stain (NanoProbes, Yaphank, NY) for 60 seconds. Stain was blotted with filter paper, and grids were allowed to dry on filter paper then stored in a container at room temperature. Grids were visualized on a FEI Morgagni 268 100kV transmission electron microscope (FEI, Hillsboro, OR) equipped with a Gatan Orius Camera (Gatan, Pleasanton, CA).

2.3.6 *Sedimentation assay:*

20 μM messicles (20 μM $PAP_{248-286}$ and 200 μM POPG), 200 μM POPG liposomes, and 20 μM $PAP_{248-286}$ were incubated at room temperature for 1 hour. Each solution was split in half and the samples were centrifuged in a Sorvall Legend Micro 21R microcentrifuge (Thermo Fisher Scientific) at 9000*g* for 10 minutes. The supernatant for each sample was removed and the pellet was resuspended in Tris buffer. The concentration of lipid in the pellet and supernatant was determined using a total phosphorus assay (78–80). The fraction of the total inorganic phosphate (P_i) for each sample was calculated by dividing the lipid concentration in either the pellet or supernatant by the sum of the two. Data presented are the average of 2 independent experiments.

Messicle disruption assays were conducted in a similar manner, except that calcein-filled liposomes were used and after the supernatant was separated from the pellet, the absorbance and fluorescence of both fractions were measured at room temperature. Supernatant and pellet were spotted onto a Take3 micro-volume plate (BioTek). The plate was placed into a BioTek Synergy HTX plate reader and the calcein absorbance spectra were collected from 450- 550 nm. Calcein fluorescence was then measured using 460 nm and 528 nm filters for excitation and emission, respectively. Data presented are representative of 2 independent experiments.

2.3.7 *Dynamic light scattering (DLS):*

$PAP_{248-286}$ was first centrifuged at 21100*g* at 4°C for 30 minutes (Sorvall Legend 21R) to remove any large aggregates. DLS titrations of 10 μM $PAP_{248-286}$ with 10, 50, 100, 150, or 200 μM of 100% POPG, 7:3 POPG:POPC, 1:1 POPG:POPC, or 100% POPC were prepared in Tris buffer and incubated for 4 minutes at room temperature. Samples were added into a 1 μL Quartz Cuvette (Wyatt Technology, Goleta, CA) and measurements were collected with a DynaPro NanoStar (Wyatt Technology). Ten to fifteen 10-second acquisitions were measured at 25°C and averaged.

The diffusion coefficient (D_t), in $nm^2/\mu s$, of each sample was determined by re-fitting the average autocorrelation curve with a single component fit using GraphPad Prism (GraphPad, San Diego, CA):

$$G^2(\tau) = 1 + \beta e^{-2D_t q^2 \tau}, \tag{2.1}$$

where β is the intercept and τ is the delay time. The scattering vector, q, is constant for the instrumental setup,

$$q = \frac{4\pi n_0}{\lambda_0} \sin\frac{\theta}{2}, \tag{2.2}$$

where the refractive index of the solution, n_0, is set to 1.33, the wavelength of the laser, λ_0, is set to 661 nm, and the scattering angle, θ, is set to 90°. The Stokes radius (R_h) was then calculated using the Stokes- Einstein relation,

$$D_t = \frac{kT}{6\pi\eta R_h}, \tag{2.3}$$

where k is Boltzmann's constant, T is temperature, and the solution viscosity, η, is set to 0.89 mPa·s (84).

For dissociation in the presence of excess $PAP_{248\text{-}286}$, $PAP_{248\text{-}286}$ was centrifuged at 21100*g* at 4°C for 30 minutes (Sorvall Legend 21R). "Dissociation", "dilution control", and "fresh 1:2" samples were prepared in the same manner as they were for the microscope dissociation experiment. Measurements were collected as described above at 4 minutes and 30 minutes after the final solution was prepared and in the same manner as previously stated. Analysis was performed as described above.

2.3.8 *Circular dichroism (CD):*

CD samples of 10 μM $PAP_{248-286}$ with 0, 50, 100, 150, 200, or 1000 μM of 100% POPG, 1:1 POPG:POPC, or 100% POPC liposomes were prepared in Tris buffer and incubated at room temperature for 4 minutes. Samples were measured in a 1 mm cuvette and spectra were collected on a Jasco J-1500 CD spectrometer (Jasco, Oklahoma City, OK). Measurements were taken at 25°C from 250-155 nm in continuous scanning mode with a scanning rate of 100 nm/min, data integration time of 1 second, and bandwidth of 1 nm. Data presented are an average of 5-7 scans after subtraction of the liposome background spectra for each sample. Secondary structure determination was done using the BeStSel algorithm (85, 86).

2.3.9 *ThT kinetic assays:*

A 500 μM solution of Thioflavin T (ThT) was prepared in Tris buffer and filtered through a 0.22 μm syringe filter. Tris buffer was added to a 96-well plate (Corning 3651, Corning, NY). $PAP_{248-286}$ was centrifuged at 21100*g* at 4°C for 30 minutes (Sorvall Legend 21R) and added to each well, followed by ThT and either 1:1 POPG:POPC or POPG liposomes, bringing the final volume to 200 μL. The final concentration of ThT, $PAP_{248-286}$, and 1:1 POPG:POPC or POPG in each well was 25 μM, 10 μM, and 100 μM, respectively. Additional wells were prepared with ThT and 1:1 POPG:POPC or POPG as a lipid background. Samples were prepared at room temperature. The plate was covered with clear polyolefin sealing tape (Thermo Fisher Scientific) to prevent evaporation and placed in a Biotek Synergy HTX multi-mode plate reader. Samples were held at 25°C and fluorescence was measured every 5 minutes using 440 nm and 485 nm filters for excitation and emission, respectively. Immediately before each read, the plate was shaken for 10-60 seconds. Since liposomes enhance ThT fluorescence, the lipid background control was first subtracted from each time point. The fluorescence signal at time 0 was then subtracted from the

background subtracted values, yielding the ΔFluorescence over time. The average of two independent experiments was plotted using GraphPad Prism.

For the SEVI fibril ThT kinetics, a 2.5 mM solution of ThT was prepared in PBS buffer (137 mM NaCl, 2.7 mM KCl, 10 mM Na_2HPO_4, 1.8 mM KH_2PO_4, pH adjusted to 7.4 with HCl), filtered through a 0.22 μm syringe filter, and stored at 4°C for up to 1 week. 1.1 mM $PAP_{248-286}$ in PBS buffer was centrifuged at 21100*g* at 4°C for 30 minutes (Sorvall Legend 21R). 7% (v/v) of Tris buffer was added to bring the final volume to 107 μL and the final concentration of $PAP_{248-286}$ to 1 mM. Fibril formation reactions were carried out at 37ºC with agitation at 1200 RPM on an Eppendorf Thermomixer C (Eppendorf North America, Hauppauge, NY). For each time point, 25 μM ThT in PBS was prepared from the 2.5 mM stock and filtered through a 0.22 μm syringe filter, and 200 μL aliquots were added to a 96-well plate (Corning 3651). To establish a background signal, the fluorescence of this solution was measured using a 440 nm excitation and 485 nm emission filter on a Biotek Synergy HTX multi-mode plate reader. A 2 μL aliquot of the fibril formation reaction was then added to each well, bringing the final concentration to 10 μM $PAP_{248-286}$. The plate was placed in the Biotek plate reader and shaken linearly at 567 cpm for one minute and the ThT fluorescence in the presence of $PAP_{248-286}$ was measured again. Samples were prepared and measured at room temperature. For analysis, the background ThT fluorescence was subtracted from the ThT fluorescence in the presence of $PAP_{248-286}$ and plotted using GraphPad Prism.

2.3.10 *Messicle seeding experiments:*

2.2 mM $PAP_{248-286}$ was dissolved in 0.22 μm syringe filtered milliQ water and centrifuged at 21100*g* at 4°C for 30 minutes (Sorvall Legend 21R). After centrifugation, the 2.2 mM $PAP_{248-286}$ was added to five separate tubes to be used for seeding experiments. An equal volume of syringe

filtered milliQ water was added to five separate tubes to serve as negative controls. The concentration of the remaining solution was determined by its absorbance at 280 nm to account for loss of peptide during sample preparation, and was used for preparation of messicle and $PAP_{248-286}$ stock solutions.

Seed, messicle, $PAP_{248-286}$, POPG, and buffer control stock solutions were prepared at room temperature at twice the desired concentrations, by mixing 0.22 μm syringe filtered PBS, POPG liposomes in Tris, Tris buffer, and/or $PAP_{248-286}$ as appropriate. Days prior to the seeding experiment, SEVI fibrils were prepared by shaking 1.1 mM $PAP_{248-286}$ at 1200 RPM on an Eppendorf Thermomixer C at 37°C until the solution became cloudy. Fibril formation was confirmed by an increase in ThT fluorescence, and fibril samples were stored at 4°C. Seeds were prepared by vortexing SEVI fibrils for 4 minutes. One part of each seed or stock solution was added to one part 2x $PAP_{248-286}$ stock solution or milliQ control, bringing the final solutions to 1x $PAP_{248-286}$ or 1x PBS with 5% Tris buffer.

Samples were incubated at 37ºC with agitation at 1200 RPM on an Eppendorf Thermomixer C. At each time point, 25 μM ThT was prepared from the 2.5 mM stock and filtered through a 0.22 μm syringe filter, followed by the addition of 200 μL aliquots to a 96-well plate (Corning 3651). To establish a background signal, the fluorescence of this solution was measured using 440 nm excitation and 482 nm emission wavelengths on a Molecular Devices Spectramax Gemini EM plate reader (Molecular Devices, San Jose, CA). 2 μL of each sample or control was then added to the wells, diluting the samples about 100-fold. The plate was shaken linearly at 567 cpm for one minute and the ThT fluorescence was measured again. All samples were prepared and measured at room temperature. For analysis, the background ThT fluorescence was subtracted from the ThT fluorescence in the presence of $PAP_{248-286}$ and plotted using GraphPad Prism.

2.3.11 *Fluorescence correlation spectroscopy (FCS):*

Alexa Fluor 488 (A488) NHS Ester (Life Technologies, Carlsbad, CA) was conjugated to 100 μM $PAP_{248-286}$ in a sodium phosphate buffer (20 mM sodium phosphate, 50 mM NaCl, pH 6.1) by incubating ~3-fold excess dye at room temperature for 3 hours or overnight at 4°C. The reaction was quenched with the addition of a pH 8.0 buffer containing 40 mM Tris and 50 mM NaCl at room temperature. Labeled $PAP_{248-286}$ was separated from unlabeled $PAP_{248-286}$ and free dye on a 250 mm x 10 mm BDS Hypersil C18 column (Thermo Fisher Scientific) run with a water/methanol gradient in the presence of 0.1% TFA on a Dionex Ultimate 3000 HPLC (Thermo Fisher Scientific). Fractions containing labeled protein were collected, and solvent was evaporated with a Savant SC210A SpeedVac Concentrator with in-line Savant RVT5105 Ultra-low Temp Refrigerated Vapor Trap (Thermo Fisher Scientific). Aliquots of dried, labeled $PAP_{248-286}$ were stored at -80°C until immediately prior to use.

FCS measurements were collected at room temperature on a home-built instrument consisting of an inverted Zeiss Axio Observer D1 (Carl Zeiss Microscopy) microscope equipped with a Picoquant PDL 828 Sepia II pulsed laser driver (PicoQuant GmbH, Berlin, Germany), Hydra-Harp 400 detection electronics (PicoQuant), and a Tau-SPAD photon counting detector (PicoQuant). The laser was passed through a 488 nm/10 nm excitation filter and collected by a 488 nm dichroic mirror and 535 nm/70 nm emission filter (all filters from Chroma Technology Corp., Bellows Falls, VT).

50 μL samples containing 2 μM unlabeled $PAP_{248-286}$, a fixed nanomolar concentration of A488-labeled $PAP_{248-286}$ resuspended in a Tris buffer (20 mM Tris, 100 mM NaCl, pH 7.4), and different concentrations of 100% POPG, 7:3 POPG:POPC, or 1:1 POPG:POPC liposomes were prepared in the Tris buffer and incubated for two minutes at room temperature. 5-7 consecutive 30

second measurements were collected and autocorrelation and time-correlated single-photon counting of the fluorescence signal from the detector were performed using the HydraHarp 400 and SymphoTime 64 software (PicoQuant). Liposomes were fluorescently labeled by incubating them with Nile Red (Acros Organics, Fair Lawn, NJ) in MeOH at a 1:100 (dye:lipid) molar ratio for at least half an hour at room temperature. Nile Red-labeled liposomes were run in the same manner as the binding titration samples to determine the diffusion time of a liposome.

Autocorrelation curves were fit using GraphPad Prism to the following equation for free diffusion of two fluorescently labeled components:

$$G(\tau) = \frac{1}{N}\left[F_B\left(1+\frac{\tau}{\tau_B}\right)^{-1}\left(1+\frac{\tau}{s^2\tau_B}\right)^{-1/2} + (1-F_B)\left(1+\frac{\tau}{\tau_{UB}}\right)^{-1}\left(1+\frac{\tau}{s^2\tau_{UB}}\right)^{-1/2}\right], \quad (2.4)$$

where $G(\tau)$ is the autocorrelation given lag time τ, N is average number of particles in the focal volume, F_B and τ_B are the fraction and diffusion time of liposome-bound $PAP_{248\text{-}286}$, respectively, τ_{UB} is the diffusion time of unbound $PAP_{248\text{-}286}$, and s (the ratio of the radial to axial dimension of the focal volume) is fixed to 0.2 based on calibration measurements. τ_B and τ_{UB} were fixed, while N and F_B were allowed to float. A one site binding model from GraphPad Prism was used to extract an apparent binding affinity, $K_{D,app}$, from a plot of the fraction bound, F_B, against the lipid concentration, $[L]$:

$$F_B = \frac{[L]}{K_{D,app} + [L]}. \quad (2.5)$$

2.3.12 *Fluorescence burst analysis:*

Samples for dissociation in the presence of excess POPG liposomes were prepared in the same manner as they were for microscope imaging, except each sample contained ~15 nM $DiOC_{16}(3)$-labeled lipids. Here, the "dissociation" and "dilution control" samples were prepared

by adding unlabeled POPG or buffer to 20 μM messicles containing $DiOC_{16}(3)$-doped POPG. Messicle, fresh 1:50, and lipid only controls were prepared as previously discussed, but contained an equivalent concentration of $DiOC_{16}(3)$-labeled lipids. After a 5-minute incubation of the final solution, the samples were placed onto the home-built Zeiss Axio Observer D1 microscope and 3 consecutive 10-minute fluorescence intensity time traces were recorded. Samples were prepared and measured at room temperature. Sample preparation and fluorescence intensity time trace collection was repeated twice for each sample, yielding an hour of time traces for each sample. A Python script was used to extract the sizes of fluorescence bursts from the intensity time traces above a defined threshold size. The size of each fluorescent burst for each sample was plotted as a frequency histogram using GraphPad Prism. A threshold of 200 photons/burst was selected because it yielded the best signal-to-noise ratio. The data presented are representative of two independent experiments.

2.3.13 *Computer simulations:*

Molecular Dynamics computer simulations were performed by Shushan He and Lutz Maibaum using the Gromacs 5.1.4 software package (87). Interactions were modeled using the all-atom Charmm36 force field, which accurately describes both lipids (88) and proteins, including weakly structured peptides (89), and which has been successfully used to study interactions between peptides and both neutral and charged lipid bilayers (see, for example, Ref. 90). Simulations were performed at a temperature of 303 K and at constant pressure and zero surface tension. The initial configuration of the phospholipid bilayer was constructed with the help of the Charmm-GUI web server (91). The bilayer contains 100 POPC and 100 POPG lipids, and was solvated in 150 mM KCl solution. The starting conformation of the peptide was an experimental structure (PDB entry 2L77 (67)), which was equilibrated under the same solvent conditions. The

peptide was then placed above the phospholipid bilayer. Within approximately 50 ns the peptide absorbed onto the bilayer. The data analyzed in this work was obtained by averaging the trajectory from 100 ns up to 2000 ns of simulation time. We calculated the number of lipid molecules in contact with the peptide, defined as any lipid that has at least one atom within 2.5 Å of any peptide atom.

2.4 RESULTS

2.4.1 *$PAP_{248-286}$ rapidly forms large co-aggregates at specific peptide:lipid ratios*

To understand its self-assembly in the presence of lipid membranes, $PAP_{248-286}$ was incubated with 100 nm lipid vesicles with varying ratios of the anionic lipid POPG. A solution containing 10 μM $PAP_{248-286}$ and 100 μM POPG (1:10 P:L ratio) became visibly cloudy within 15 minutes, while solutions at 1:1 or 1:25 P:L ratios remained clear (Figure 2.1a). Light microscopy showed that this cloudiness is due to the formation of micron-scale cloud-like or flocculent aggregates. These aggregates were not observed at the 1:1 P:L ratio, and are much less abundant at 1:25 than at 1:10 (Figure 2.1b). At 14,000x magnification, negative stain transmission electron microscopy (TEM) showed that aggregates at the 1:10 ratio look like masses of striated protein that appear somewhat fibrillar (Figure 2.1c). It should be noted that aggregates were sometimes observed at a 1:1 and 1:25 P:L ratio. The aggregates at 1:1 P:L seemed smaller, while aggregates at 1:25 P:L seemed thinner and more ribbon-like (Figure 2.1c and 2.2a). A large mass with a diameter of about 4 μm was also observed on the 1:10 P:L ratio grid, showing how heterogenous this species is (Figure 2.1d). This species is not formed by $PAP_{248-286}$ or LUVs alone, showing that this aggregation is specific to peptide/lipid co-assembly (Figure 2.2b-d). For convenience, we refer

to this mixed $PAP_{248-286}$/lipid co-aggregated species as a "messicle" (an abbreviation for "*m*ultiple *e*ntrapped ve*sicles*" or for a "*mes*s of ve*sicles*").

To verify that messicles are indeed a peptide/lipid co-assembly, they were pelleted by centrifugation for 10 minutes at 9000*g*, and the concentration of phospholipids in solution vs. pelleted was determined using a total phosphorus assay. About 96% of phospholipid was pelleted with the messicles, while pelleted phospholipids were not detected in a control sample of POPG without $PAP_{248-286}$ (Figure 2.1e). We also tested whether liposomes were disrupted upon incorporation into messicles, since $PAP_{248-286}$ is known to disrupt lipid membranes at micromolar concentrations (65). POPG liposomes were filled with 7 mM of calcein, which results in partial self-quenching of this dye's fluorescence. Messicles or control liposomes were again pelleted by centrifugation, the pellet was resuspended, and the calcein absorbance and fluorescence of the pellet and supernatant was measured. Calcein absorbance was not detected in either pellet, but both supernatants showed similar calcein absorbance, suggesting that the liposomes in the messicles have leaked and released their calcein contents into solution. Fluorescence is higher for the messicle supernatant than the liposome control, indicating the liposomes in the control are intact and the encapsulated calcein remains partially quenched (Figure 2.3a and 2.3b). Beyond the observation that liposomes in vesicles have leaked their contents, the structure or arrangement of lipids in messicles remains unclear.

2.4.2 *Messicle formation depends on liposome charge*

We wanted to determine whether messicles form with liposomes of other lipid compositions. A distinguishing characteristic of messicles is that they are large, which allowed the use of particle sizing by dynamic light scattering (DLS) to quickly assay co-assembly under a variety of different lipid compositions and peptide:lipid ratios. In agreement with imaging at

various magnifications (Figure 2.1), the largest particles in a titration of POPG into $PAP_{248-286}$ form at the 1:10 P:L ratio. Moving away from that ratio yields smaller particles. Interestingly, messicle formation was not detectable when doing the same measurements with liposomes composed of 1:1 POPC:POPG, which carry a 50% negative charge, instead of the 100% negatively charged POPG liposomes. Messicle formation was also not observed with neutral POPC liposomes (Figure 2.4a). We therefore determined that, under our experimental conditions, messicles will not form with liposomes that contain less than 50% anionic lipids.

$PAP_{248-286}$ seems to adopt an unusual secondary structure in messicles. The shape of a far-UV circular dichroism (CD) spectrum can give information about the secondary structure of a protein (92). Disordered or random-coil proteins and peptides display negative ellipticity with a single, well-defined minimum around 195 nm; α-helical peptides display positive ellipticity around 193 nm and a broad negative band with two minima at 208 nm and 222 nm; and β-sheet structure yields a maximum around 190 nm and a single minimum around 216 nm (92). $PAP_{248-286}$ displays the expected random coil spectrum in solution, and partial α-helical content at P:L ratios of 1:25 or greater (Figure 2.5c), consistent with previous reports (65). However, at the 1:10 P:L ratio with POPG, a large, distinctive signal with a minimum at 208 nm was observed after a 4-minute incubation (Figure 2.4b). The unusual spectral shape did not correspond to a single secondary structure, but could perhaps be due to a mixture of α-helix and β-sheet (93), β-sheet and random coil (94), or a combination of all three (95). The mean residue ellipticity (MRE) at 208 nm was used to monitor the population of this secondary structure over different lipid compositions and P:L ratios (Figure 2.4c). A minimum at 208 nm is only observed with POPG and not with POPC or 1:1 POPC:POPG liposomes (Figure 2.5a and 2.5b), again suggesting that messicles form near the 1:10 $PAP_{248-286}$:lipid ratio but only for liposomes with > 50% negative charge.

2.4.3 *Messicles are amyloid-like, but distinct from bona fide SEVI amyloid*

Because $PAP_{248-286}$ forms amyloid fibrils (69) and anionic liposomes can promote amyloidogenesis of other proteins (25, 26, 37), we explored the possibility that messicles are, in fact, merely amyloid aggregates. Like most amyloid aggregates, messicles bind to and enhance the fluorescence of the diagnostic dye, Thioflavin T (ThT), as much as or more than $PAP_{248-286}$-derived SEVI amyloid. This by itself does not establish that messicles are a variety of amyloid aggregate, since some non-amyloid states can also enhance ThT fluorescence (96, 97). Importantly, the formation kinetics are different: while $PAP_{248-286}$ aggregation displays the characteristic sigmoidal formation kinetics when forming SEVI amyloid, messicle formation lacks a lag phase and instead displays exponential kinetics (Figure 2.6a). SEVI amyloid formation is relatively slow, taking ≥ 10 hours, even at ~1 mM peptide concentration under optimal conditions (when shaken at 37ºC in phosphate buffered saline (PBS)). In fact, in our hands SEVI amyloid did not form reliably in Tris buffer, even over several days. By contrast, messicles form much more readily, taking ≤ 5 minutes at room temperature with just 10 μM peptide, whether in PBS, Tris, or HEPES buffer. When visualized by negative stain EM, messicles were clearly more heterogenous and wider than the bundled SEVI fibrils, suggesting that messicles also have a distinct morphology from *bona fide* SEVI amyloid (Figure 2.6b).

Another characteristic feature of amyloid is that the addition of a small amount of aggregate seed to a solution of amyloid-competent protein monomers will nucleate the amyloid formation process, bypassing the lag phase in the sigmoidal kinetics (11). Regardless of the variability observed for SEVI amyloid kinetics (98), messicles were unable to seed SEVI amyloid formation to the same extent as an equivalent concentration of SEVI seeds. As controls, the two components of messicles, $PAP_{248-286}$ and POPG, were also unable to seed amyloid formation (Figure 2.6c and

Figure 2.7). This suggests that messicles have a distinct molecular conformation from *bona fide* SEVI amyloid, or that inclusion into messicles in some way occludes $PAP_{248-286}$ from participating in the interactions necessary for the growth of SEVI fibrils. Therefore, although they are ThT-positive, messicles seem to be mechanistically and structurally distinct from amyloid fibrils.

2.4.4 *Messicle formation is not driven by charge neutralization*

Given its strong dependence on liposome charge, one possibility is that messicle formation could be occurring through a charge neutralization mechanism, as seen in some flocculation phenomena (99). According to this mechanism, messicles form at the optimal $PAP_{248-286}$:POPG ratio of 1:10 because the cationic peptide molecules exactly neutralize the negative charges on the outer leaflet of each liposome. Electrostatic repulsion between cationic particles at P:L ratios > 1:10, or between anionic particles at P:L ratios < 1:10, would disfavor condensation at other ratios. Aggregation due to charge neutralization has been proposed for a variety of cationic peptides and polyelectrolytes with anionic liposomes that display qualitatively similar biphasic dose response relationships (58–60).

This model predicts that messicles formed with 7:3 POPG:POPC liposomes would require ~1.4-fold less $PAP_{248-286}$ to neutralize charge, since the surface charge is 30% less negative. In fact, the optimal ratio for messicle formation, assessed by DLS in six independent trials, was essentially identical whether using POPG or 7:3 POPG:POPC liposomes (Figure 2.8a). While the precise optimal P:L ratio varied between 1:10 and 1:14 from day to day (presumably due to minor inconsistencies in liposome preparations), in every case the fold-change in the optimal ratio was much closer to 1 than the 1.4 predicted by the charge neutralization mechanism (Figure 2.8b). Messicles produced using POPG or 7:3 POPG:POPC liposomes are thus identical in both P:L ratio

and morphology (Figure 2.8c). Because the optimal P:L ratio does not change with a changing liposome charge, a charge neutralization model is inconsistent with the data.

2.4.5 *Messicle formation is consistent with a polyvalent assembly model*

Another general coagulation mechanism is interparticle bridging wherein a flocculant mediates the condensation of larger particles through multiple weak interactions (99). Similar principles have been used to engineer the directed self-assembly of functionalized liposomes and nanoparticles (100–103). An optimal P:L ratio between 1:10 and 1:14 corresponds to each $PAP_{248-286}$ molecule making contacts with 5–7 lipid molecules (since the outer leaflet of a liposome contains roughly half of the total lipid). Molecular dynamics simulations of a single $PAP_{248-286}$ molecule bound to a lipid bilayer (Figure 2.9a) show between 4 and 14 lipid contacts, meaning that a lipid contact number in the 5–7 range is consistent with the formation of a peptide monolayer surrounding each vesicle. Under these conditions, peptide-peptide interactions could bridge different liposomes, with multiple weak peptide-peptide interactions leading to condensation. An increase in lipid content would dilute the membrane-bound peptide so that the monolayers are incomplete, and make these bridging interactions less likely. Excess peptide would bind to $PAP_{248-286}$-coated liposomes and passivate them, competitively blocking interactions with other peptide-coated liposomes and slowing down messicle formation (Figure 2.9b).

In this model, $PAP_{248-286}$ needs to have a high enough binding affinity (K_D) for the liposome to form a monolayer under the experimental concentrations. Fluorescence correlation spectroscopy (FCS) was used to assess liposome binding by measuring the change in diffusion time of fluorescently labeled $PAP_{248-286}$ with liposomes of varying concentrations and compositions (Figure 2.10). The apparent K_D values of $PAP_{248-286}$ for POPG, 7:3 POPG:POPC and 1:1 POPG:POPC were determined to be 0.02, 0.08 and 2 mM, respectively (Figure 2.9c). Binding was

not observed with POPC liposomes (data not shown). The large difference in binding affinity of $PAP_{248-286}$ for 7:3 and 1:1 POPG:POPC liposomes could explain why messicles form with the former and not the latter; in our hypothesized model, the weaker affinity of $PAP_{248-286}$ for 1:1 liposomes would disfavor monolayer formation, and therefore messicle assembly, under experimental conditions.

Under a polyvalent assembly model, with many weak interactions driving co-aggregation, messicles would dissociate slowly relative to the timescale of a single peptide dissociating from the membrane. To monitor messicle disassembly, we used DLS to measure particle size after the addition of excess $PAP_{248-286}$ to pre-formed messicles, to bring the final P:L ratio to 1:2. If these messicles dissociated, their hydrodynamic radius would match that of freshly prepared 1:2 P:L; if not, the hydrodynamic radius would match that of a "dilution control" to which a matched amount of buffer has been added. The hydrodynamic radius of the "dissociated" samples matched the dilution controls at both 4 and 30 minutes, indicating that messicle dissociation is negligible on this timescale (Figure 2.9d). Note that the freshly prepared 1:2 P:L ratio sample continues to grow over 30 minutes, approaching the size of the other samples. This is in agreement with the observation that some messicle assembly can be observed at large P:L ratios (Figures 2.1c and 2.4a), albeit more slowly than at the optimal 1:10 ratio. These results are also in agreement with light microscopy (Figure 2.11a), where over the course of an hour, the dissociated species looks similar to the dilution control but the freshly prepared 1:2 sample continues to grow.

Unfortunately, DLS could not be used to test if addition of excess liposomes can cause messicle dissociation, because of interference from light scattered by the added liposomes. Instead, we applied confocal single-particle fluorescence burst analysis using liposomes doped with fluorescent lipids. In this experiment, the fluorescence intensity of a dilute solution of labeled

particles is monitored using a confocal microscope and continuously binned (Figure 2.12a). One or more consecutive bins that exceed a defined background fluorescence are summed to yield the intensity of the overall fluorescent burst, assumed to represent a single particle diffusing across the observation volume of the microscope. Larger particles like messicles will yield, on average, longer and more intense fluorescence bursts than smaller particles, like individual liposomes, because larger particles will diffuse more slowly through the observation volume, and they may contain multiple labeled liposomes. We monitored messicles after the addition of POPG to bring the final P:L ratio to 1:50 ("dissociation"), and compared them to a freshly prepared 1:50 sample and to a "dilution control" of messicles to which buffer volume had been matched. Comparing the distribution of burst sizes collected over 30 minutes, the messicle and "dissociation" samples resemble the dilution control, while the "fresh 1:50" sample resembles POPG liposomes alone (Figures 2.9e and 2.12). This result also agrees with light microscopy of each species over the course of an hour at a 20x magnification (Figure 2.11b). These results again indicate that once messicles have formed, they are resistant to disruption by excess peptide or lipid. This kinetic stability is consistent with a polyvalent interaction model.

2.5 Discussion

We have described a previously uncharacterized higher-order species of $PAP_{248-286}$ that, while similar in some ways to the well-studied SEVI amyloid, has important structural and mechanistic differences. While $PAP_{248-286}$ messicles are ThT positive, they are more heterogeneous than SEVI fibrils, and are unable to seed amyloid formation. They are also able to form at much lower concentrations (10 μM vs. > 500 μM), more rapidly (< 30 minutes vs. ~8–48 hours), and with non-sigmoidal kinetics. Moreover, they have a distinct secondary structure. Under our

experimental conditions, we determined that messicles form most quickly near a 1:10 P:L ratio and require vesicles with at least 70% anionic lipids. However, once formed, messicles are not quickly dispersed by subsequent changes in P:L ratio, consistent with a mechanism involving polyvalent assembly or interparticle bridging of lipid vesicles by $PAP_{248-286}$.

We believe it is possible that some or all of the biological activity assigned to $PAP_{248-286}$–derived SEVI amyloid is in fact due to a messicle-like species. Semen enhances ThT fluorescence, an effect thought to indicate the presence of endogenous seminal amyloids including SEVI (104). However, it is also possible that some ThT fluorescence is due to the formation of amyloid-like messicles, since the *in vitro* ThT fluorescence of messicles is similar to that of SEVI amyloid (Figure 2.6a). Therefore, messicles may be involved in the best-studied activity of $PAP_{248-286}$: its ability to enhance HIV infection. *In vitro*, SEVI amyloid enhances HIV infection while freshly dissolved $PAP_{248-286}$ monomer was inactive. The ability to enhance HIV infection was therefore assigned to SEVI amyloid and not monomeric $PAP_{248-286}$. However, in the presence of seminal fluid, $PAP_{248-286}$ also enhances HIV infection (69). It is therefore possible that enhancement of HIV infectivity is due to the co-assembly of $PAP_{248-286}$ into a messicle or messicle-like species with a component of seminal fluid. Intriguingly, seminal fluid is abundant in extracellular vesicles (EVs), historically called prostasomes, which are negatively charged vesicles with a diameter of 40–500 nm, and could potentially serve as a component for messicle formation *in vivo* (75, 105, 106).

Similarly, the beneficial activities proposed for $PAP_{248-286}$ could also depend on lipid-mediated co-assembly. It has been proposed that SEVI is an antimicrobial peptide, and that it may participate in sperm quality control and removal. Like other self-assembling AMPs, SEVI fibrils can agglutinate bacteria and promote their phagocytosis (64). Via a similar mechanism, it was

demonstrated that SEVI fibrils trap spermatozoa and increase their uptake by macrophages (72). However, the formation of a messicle-like species presents a mechanism by which non-amyloid $PAP_{248-286}$ could exert similar biological activities. Given our *in vitro* results, an agglutination mechanism driven by co-assembly would result in an atypical, highly biphasic dose-response curve. Experiments carried out at a single concentration of $PAP_{248-286}$ would fail to detect such activity unless both the peptide concentration and the ratio of peptide to target cells or vesicles happened to fall close to optimal values. Future work testing different peptide concentrations is required to reveal whether the $PAP_{248-286}$ monomer can co-assemble with spermatozoa, pathogenic bacteria, or other constituents of seminal fluid to form messicle-like species.

It is also possible that many other factors could affect how easily and quickly messicles form. While we have determined a relatively narrow set of conditions under which messicles form, it is possible that they can also form in more complex systems. We have determined that both P:L ratio and lipid charge are important to the polyvalent co-assembly model that we have proposed. In agreement with the work from Ramamoorthy and co-workers (65, 107), our results have demonstrated the importance of electrostatic interactions to the interaction of $PAP_{248-286}$ monomer with membranes. It remains to be seen if lipid compositions enriched in EVs, spermatozoa, or bacterial cell membranes (105, 108–112), including proportions of species like sphingomyelins, phosphatidylinositols, and cardiolipins, would impact $PAP_{248-286}$/membrane interactions and therefore messicle formation. It is also possible that the negative charges associated with acidic sugars could drive co-assembly with $PAP_{248-286}$ to form messicle-like structures. For example, spermatozoa and EVs are coated with proteoglycans, glycoproteins, and glycolipids rich in sulfated sugars and acidic sugars like sialic acid, likely contributing to their negative surface potentials (113–115). Meanwhile, Gram-positive and -negative bacteria are highly decorated with

techoic acid polymers and lipopolysaccharide (LPS), respectively, and changes in these constituents are thought to contribute to AMP resistance (116, 117). Changes in the glycocalyx could affect the propensity of cells or vesicles to self-assemble with $PAP_{248-286}$ or similar peptides.

While we have hypothesized that formation of a monolayer of peptide around liposomes results in interparticle bridging of these coated liposomes, we do not know the exact nature of the co-assembly. Another possible mechanism is one where peptides form a multimeric (perhaps amyloid-like) structure on the lipid membrane and these multimers are able to mediate interactions with other peptide-bound liposomes. It is also possible that these messicles are, at least in part, composed of dramatically restructured liposomes. A third possibility is that many individual $PAP_{248-286}$ monomers are each able to bridge the distance between the two liposomes. Regardless of which of the proposed mechanisms is responsible for messicle formation, we would expect that polyvalent assembly is required. The relative stability of messicles to changes in P:L ratio (Figure 2.9) provides evidence for a polyvalent mechanism of co-assembly. It is possible that this formation mechanism is generally applicable to many of the other systems where antimicrobial and amyloid-forming peptides bind to membranes and self-assemble (22, 25, 26–33, 40, 41, 56–63), and that many of the other biological functions and pathologies associated with these peptides could in fact involve messicle formation.

2.6 FIGURES

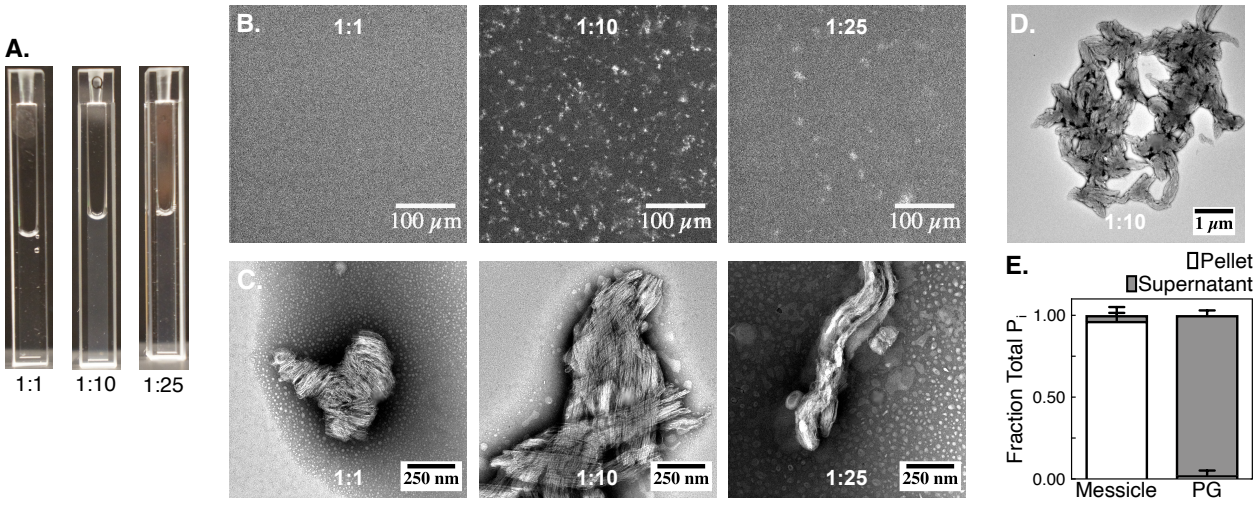

Figure 2.1: Large peptide-lipid co-aggregates, termed messicles, are preferentially formed at a 1:10 ratio of $PAP_{248-286}$:POPG.

(A) After a 15 minute incubation, 10 μM $PAP_{248-286}$ mixed with 100 μM POPG liposomes is visibly cloudier than with 10 μM or 250 μM POPG. (B) After a 30 minute incubation, 20 μM $PAP_{248-286}$ mixed with 200 μM POPG liposomes yields more numerous micron-scale aggregates than with 20 μM or 500 μM POPG. Images of the slide surface are at 20x magnification, and represent seven different fields of view taken at different positions on the slide surface. Scale bars indicate 100 μm. (C) Negative stain transmission electron microscopy (TEM) of 10 μM $PAP_{248-286}$ incubated with 10, 100, and 250 μM POPG for 4 minutes shows that the 1:10 ratio also yields larger nanometer-scale aggregates. Scale bars indicate 250 nm. (D) TEM micrograph of a larger aggregate formed with 10 μM $PAP_{248-286}$ and 100 μM POPG, present on the same grid as the 1:10 image from panel C. Scale bar indicates 1 μm. (E) Fraction of recovered phosphate (Pi) in pellet (white) or supernatant (gray) upon sedimentation of 20 μM messicle (20 μM $PAP_{248-286}$ + 200 μM POPG) or 200 μM POPG liposomes after an hour-long incubation, indicating that the lipid has been almost entirely incorporated into the messicle co-aggregate. Bars represent the mean and standard deviation of two independent experiments conducted on different days.

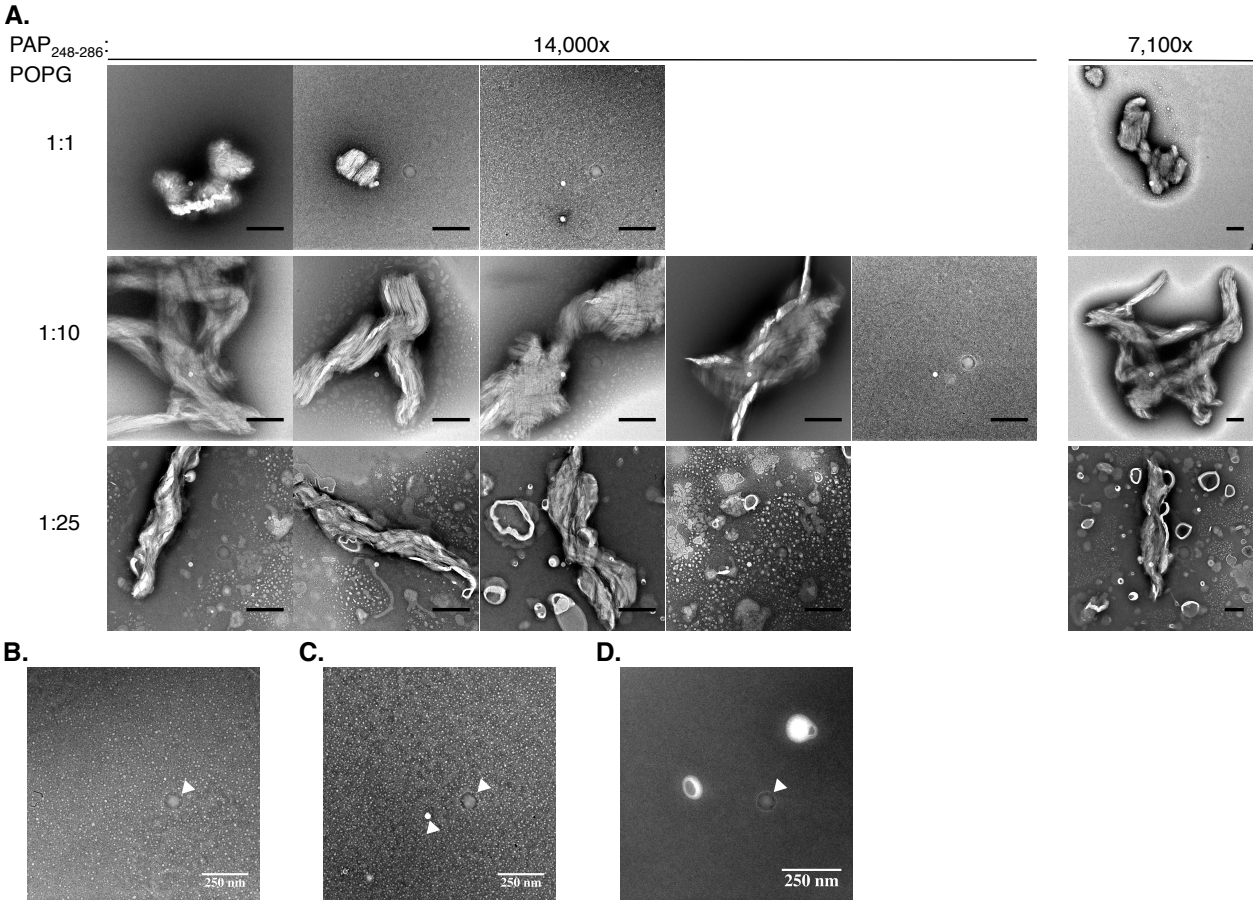

Figure 2.2: TEM controls and additional fields.

(A) Additional TEM micrograph fields of 10 μM $PAP_{248-286}$ incubated with 10, 100, and 250 μM POPG for 4 minutes. To avoid bias, these micrographs were collected in a blinded protocol where the experimenter did not know the identity of the grids used. Additional fields emphasize presence of the largest, more amorphous aggregates at a P:L ratio of 1:10, small aggregates at 1:1 P:L, and more ribbon-like aggregates at 1:25 P:L. Magnification of 14,000x or 7,100x is indicated above micrographs. All scale bars indicate 250 nm. Aggregates are not observed on grids with (B) buffer, (C) 22 μM SEVI, or (D) 250 μM POPG**.** Representative micrographs (B) and (C) are at a magnification 14,000x and (D) is at 18,000x magnification. Arrows denote camera artifacts.

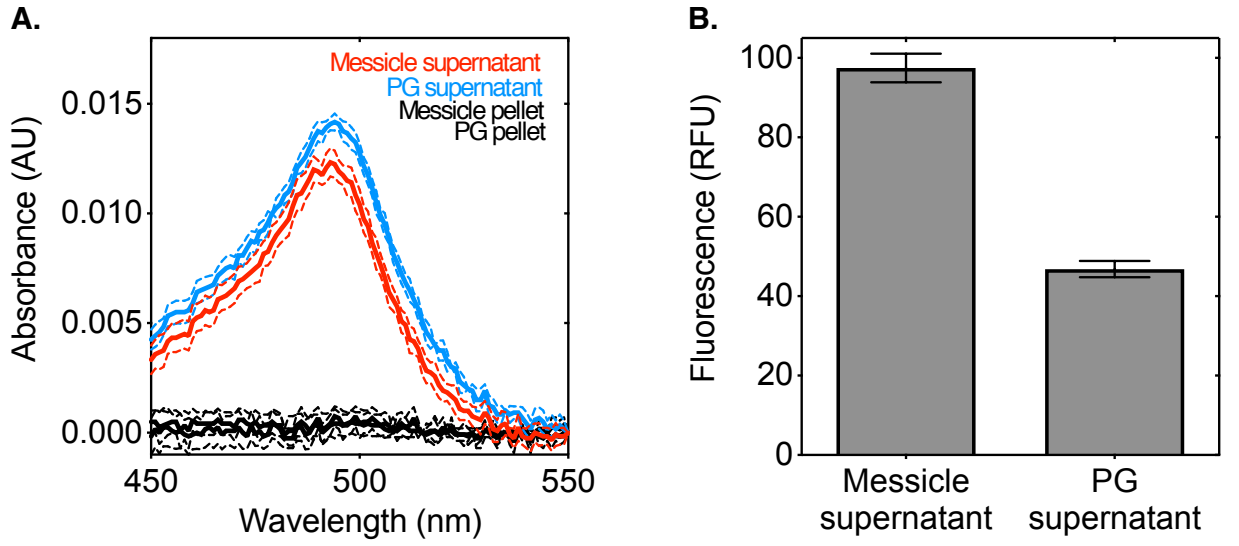

Figure 2.3: Liposomes within the messicle have leaked their contents.

(A) Baseline-subtracted calcein absorbance of 20 μM messicle (20 μM $PAP_{248-286}$ + 200 μM of calcein-filled POPG, *red*) and 200 μM of calcein-filled POPG liposome (*blue*) supernatant and pellet after centrifugation (10 minutes at 9000*g*). Under these conditions, messicles are pelleted but liposomes remain in solution. Calcein remains in the messicle supernatant, indicating it has not been pelleted along with the lipids and has instead been released into solution. Lines represent the mean and standard deviation of 12 technical replicates. (B) Calcein fluorescence of the messicle and liposome supernatants after centrifugation. The increased fluorescence of the messicle supernatant confirms that calcein has been released into solution upon messicle formation. Error bars represent the mean and standard deviation of 11 technical replicates. All data are representative of two independent experiments.

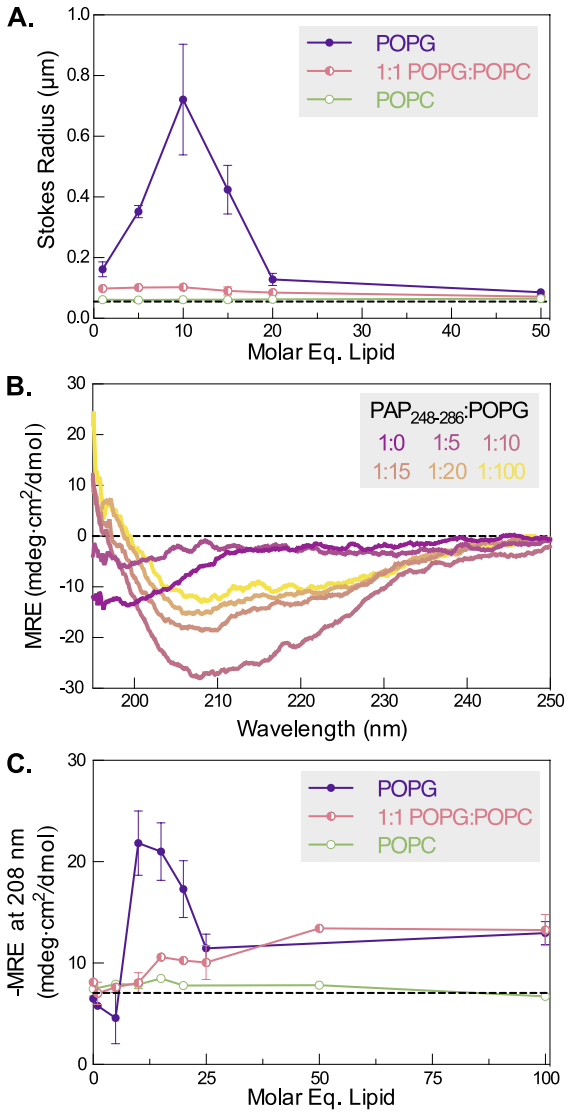

Figure 2.4: Messicle formation depends on lipid charge.

(A) Average particle size of 10 μM $PAP_{248-286}$ incubated with 1, 5, 10, 15, 20, and 50 molar equivalents of POPG (*purple*), 1:1 POPG:POPC (*pink*), and POPC liposomes (*green*) for 4 minutes as determined by dynamic light scattering. Error bars represent the mean and standard deviation of two independent experiments for 1:1 POPG:POPC and POPC liposomes and four independent experiments for POPG liposomes. The black dashed line indicates the average Stokes radius measured for liposomes with 100 nm nominal diameter. (B) Representative overlay of far-UV circular dichroism (CD) spectra for 10 μM $PAP_{248-286}$ incubated with varying concentrations of POPG liposomes for 4 minutes (*purple* to *yellow*). (C) The CD-derived negative mean residue ellipticity (-MRE) at 208 nm as a function of lipid concentration, for 10 μM $PAP_{248-286}$ incubated for 4 minutes with POPG (*purple*), 1:1 POPG:POPC (*pink*), or POPC liposomes (*green*). Error bars represent the mean and standard deviation of two independent experiments for 1:1 POPG:POPC and POPC liposomes and four independent experiments for POPG liposomes. The black dashed line indicates the average signal at 208 nm for $PAP_{248-286}$ alone.

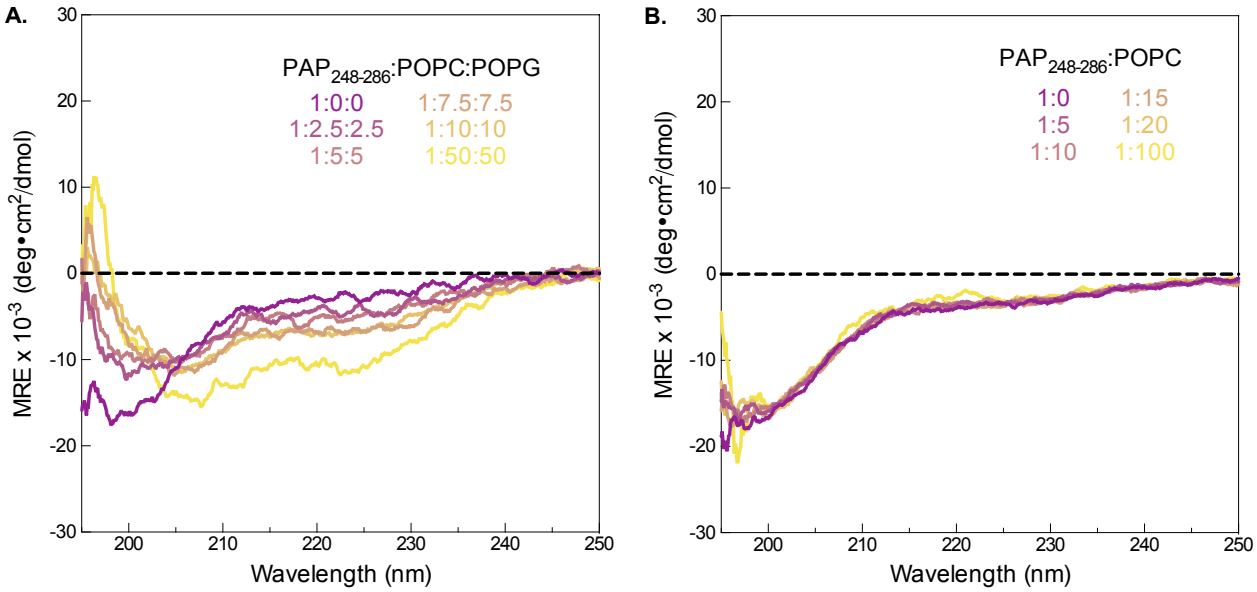

C.

Lipid Composition	POPG						1:1 POPC:POPG					
$PAP_{248-286}$:lipid ratio	1:0	1:5	1:10	1:15	1:20	1:100	1:0	1:5	1:10	1:15	1:20	1:100
% α-helix	0	2	32	31	28	24	0	4	17	15	16	24
% Antiparallel β-sheet*	23	12	29	10	4	5	26	18	19	12	16	8
% Parallel β-sheet	0	0	0	0	0	5	0	0	0	4	3	3
% Turn	19	24	2	12	13	15	17	20	18	18	19	16
% Others**	58	62	37	47	55	51	57	59	47	52	46	49

*in the BeStSel algorithm, highly disordered sequences can also contribute to this signal

**includes 3_{10}-helix, α-helix, β-bridge, bend, and loop/irregular

Figure 2.5: Messicle secondary structure not observed with 1:1 POPG:POPC or POPC liposomes.

Representative overlay of far-UV circular dichroism spectra for 10 μM $PAP_{248-286}$ incubated with varying molar equivalents of (A) 1:1 POPC:POPG and (B) POPC liposomes for 4 minutes (*purple* to *yellow*). There is no change in secondary structure indicative of binding to neutral liposomes, while $PAP_{248-286}$ assumes a predominantly α-helical structure upon binding to 1:1 POPC:POPG but does not show a component with a trough at 208 nm. Data are representative of two independent experiments. (C) Determination of secondary structure from the CD spectra in Figures 2.4b and 2.5a, respectively, using the BeStSel algorithm.

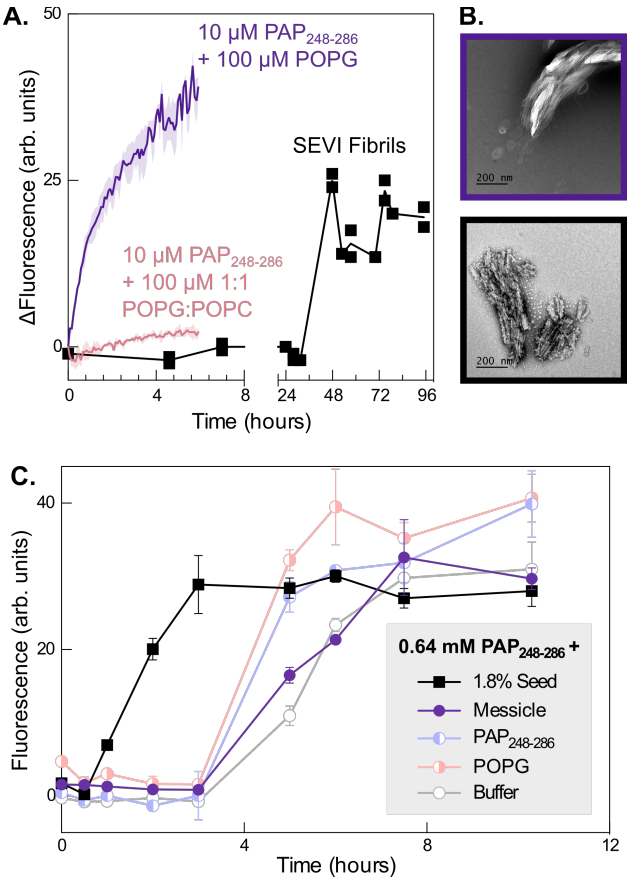

Figure 2.6: Messicles are kinetically and morphologically distinct from *bona fide* SEVI amyloid.

(A) ThT fluorescence of 10 μM $PAP_{248-286}$ with 100 μM POPG (messicle, *purple*) or 100 μM 1:1 POPG:POPC liposomes (*pink*), and 10 μM SEVI fibrils (*black*). The fluorescence signal was corrected for background from buffer, lipid and ThT, and baseline-subtracted (DFluorescence). For the 10 μM $PAP_{248-286}$ + 100 μM POPG or 1:1 POPG:POPC results, the error bands represent the mean and standard deviation of two independent experiments conducted on separate days. For SEVI fibrils, the points indicate two technical replicates, and the results are representative of four independent experiments conducted on separate days. (B) Representative negative stain EM micrographs of 10 μM messicles incubated for 1.5 hours (top, *purple*) and SEVI fibrils diluted to 2.1 μM (bottom, *black*), showing that messicles are more amorphous and less structured than amyloid fibrils. The magnification of both micrographs is 18,000x and the scale bars indicate 200 nm. (C) Representative seeding experiment containing 0.64 mM $PAP_{248-286}$ with ThT and either 1.8% SEVI fibril seeds (~20 μM $PAP_{248-286}$, *black*), 20 μM messicle (20 μM $PAP_{248-286}$ + 200 μM POPG, *purple*), 20 μM $PAP_{248-286}$ (*blue*), 200 μM POPG (*pink*), or buffer (*grey*), showing that messicles are unable to seed amyloid formation as effectively as SEVI fibrils. The fluorescence signal was background corrected using analogous samples lacking the 0.64 mM $PAP_{248-286}$. The error bars represent the standard deviation of three technical replicates. Figure 2.7 shows additional independent seeding experiments conducted on different days.

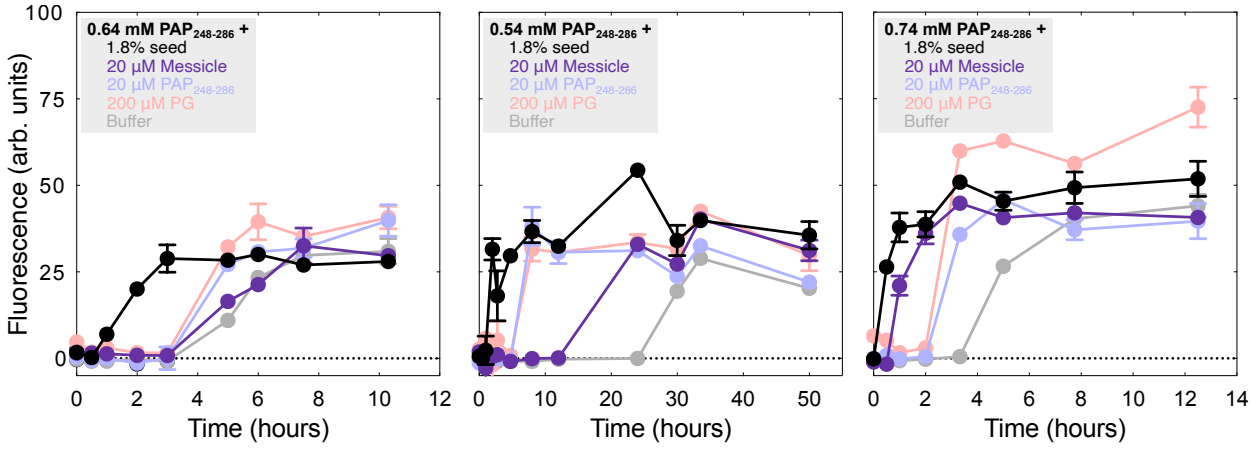

Figure 2.7: Messicles do not seed SEVI fibril formation to the same extent as SEVI fibril seeds, regardless of variability in formation kinetics.

Fibril formation kinetics of three independent experiments. The data in the left graph are the same as Figure 2.6c. Each experiment contains 0.54-0.74 mM $PAP_{248-286}$ with ThT and either 1.8% seed (~20 μM SEVI fibril seeds, *black*), 20 μM messicle (20 μM SEVI + 200 μM POPG, *purple*), 20 μM $PAP_{248-286}$ (*blue*), 200 μM POPG (*purple*), or buffer (*grey*). The same samples were prepared without the 0.54-0.74 mM $PAP_{248-286}$ as background and subtracted. The error bars represent the standard deviation of 3 technical replicates. In addition to the great variability generally observed in unseeded amyloid formation kinetics, it should be noted that different experiments used slightly different concentrations of $PAP_{248-286}$ and different synthesized batches of $PAP_{248-286}$, both of which may contribute to the observed differences in kinetics for different experiments.

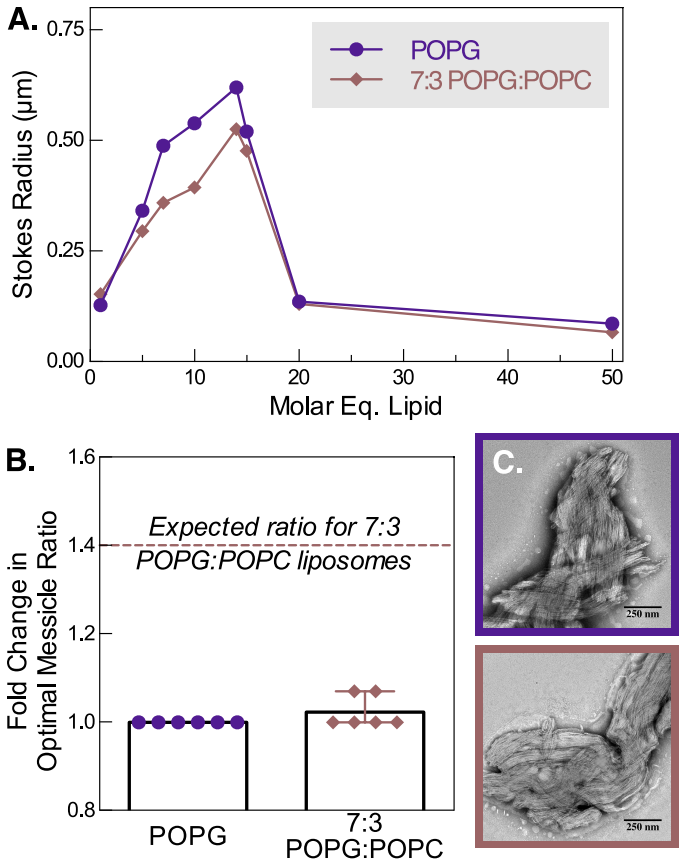

Figure 2.8: Co-assembly is not driven simply by charge neutralization-induced coagulation.

(A) Representative particle size of 10 μM $PAP_{248-286}$ incubated with 1, 5, 7, 10, 14, 15, 20, and 50 molar equivalents of POPG (*purple*) or 7:3 POPG:POPC (*brown*) liposomes for 4 minutes as determined by dynamic light scattering, showing that both lipid compositions have similar optimal ratios for messicle formation. (B) Across independent experiments conducted on six different days with either 10 or 20 μM $PAP_{248-286}$, the optimal P:L ratio for messicle formation for 7:3 POPG:POPC is close to that for POPG, and never approaches the theoretical fold-change predicted by a charge neutralization model (dashed brown line). (C) Representative negative stain EM micrographs of 10 μM $PAP_{248-286}$ incubated with 100 μM of POPG liposomes for 4 minutes (top, *purple*; same image shown in Fig. 2.1c) and 10 μM $PAP_{248-286}$ incubated with 100 μM of 7:3 POPG:POPC liposomes for 4 minutes (bottom, *brown*), showing that both messicle preparations are similar in size and morphology. The magnification of both micrographs is 14,000x and the scale bars indicate 250 nm.

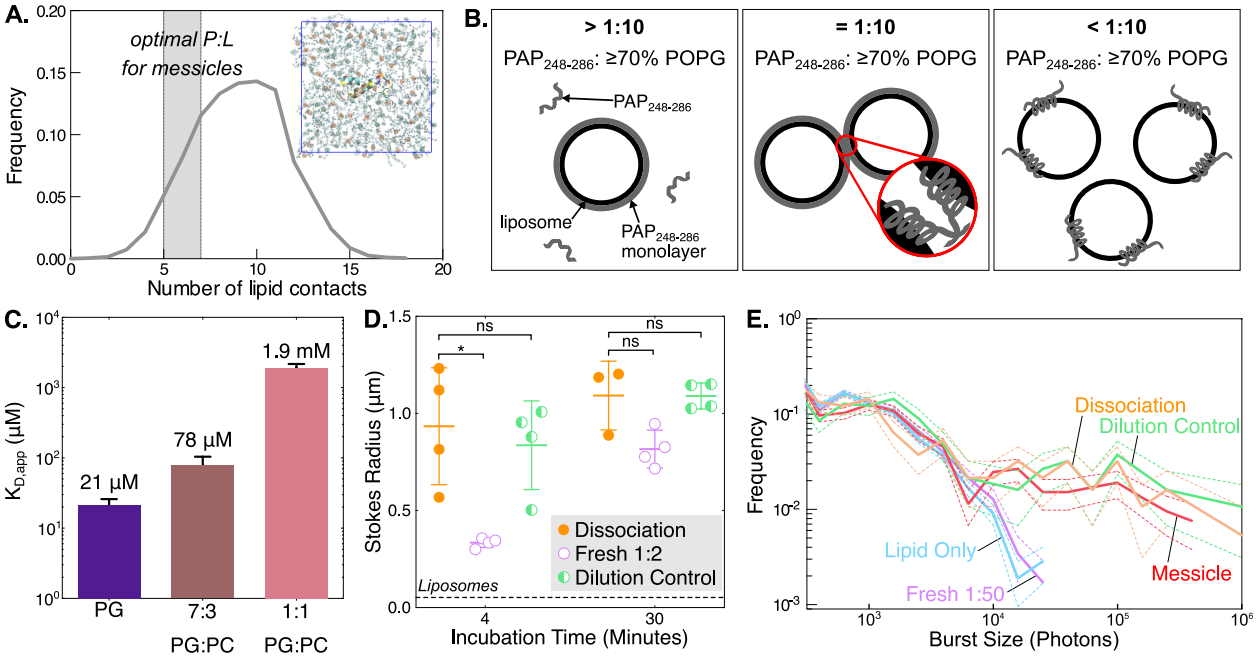

Figure 2.9: Messicle stability is consistent with $PAP_{248-286}$-induced polyvalent assembly of liposomes.

(A) Probability distribution of observed peptide-lipid contacts in a simulation of a single $PAP_{248-286}$ peptide absorbed onto a 1:1 POPG:POPC bilayer spans the range of optimal ratios for messicle formation, indicating that the conditions that drive messicle assembly are consistent with the formation of a peptide monolayer around each liposome. The inset shows a simulation snapshot, with a top-down view of the peptide and the upper bilayer leaflet. Lipids' phosphate atoms are highlighted in orange (POPC) and green (POPG). (B) Schematic of the proposed mechanism. When the $PAP_{248-286}$:lipid ratio is greater than 1:10 (left panel), there are too few liposomes to assemble or the excess $PAP_{248-286}$ acts to passivate liposomes and slow down assembly. Near the optimal 1:10 $PAP_{248-286}$:lipid ratio (center panel), if the anionic content is sufficiently high (≥ 70% POPG), the liposome surface is covered in a monolayer of peptide, allowing for many weak lipid-peptide-peptide-lipid interactions. When the $PAP_{248-286}$:lipid ratio is less than 1:10, excess liposomes bind to and sequester $PAP_{248-286}$. (C) The binding affinity of $PAP_{248-286}$ for liposomes composed of POPG (*purple*), 7:3 POPG:POPC (*brown*), and 1:1 POPG:POPC (*pink*) determined by fluorescence correlation spectroscopy (FCS) lipid titrations (see Figure 2.10). Each bar represents the mean apparent K_D ($K_{D,app}$) and SEM of at least 3 independent titration experiments. (D) Messicle stability upon the addition of excess $PAP_{248-286}$ determined by DLS particle sizing. The sizes of the dissociated messicle, "dissociation" (20 μM $PAP_{248-286}$ + 40 μM POPG, *orange*), the concentration-matched control, "fresh 1:2" (20 μM $PAP_{248-286}$ + 40 μM POPG, *purple*), and "dilution control" (4 μM $PAP_{248-286}$ + 40 μM POPG, *green*) were all measured after a 4 and 30 minute incubation period. The size of the POPG liposome is shown by the broken line. Each point represents an independent experiment, and the bar represents the mean and standard deviation. ns, no statistically significant difference; *P <0.05 (Welch's t test). (E) Messicle stability upon the addition of excess POPG determined by single particle fluorescence. Each sample contained 15 nM $DIOC_{16}(3)$- doped POPG liposomes. Burst size analysis was done for the 20 μM "messicle"

(20 μM $PAP_{248-286}$ + 200 μM POPG, *red*), the dissociated messicle, "dissociation" (4 μM $PAP_{248-286}$ + 200 μM POPG, *orange*), the "lipid only" control (200 μM POPG, *blue*), the "dilution control" (4 μM $PAP_{248-286}$ + 40 μM POPG, *green*), and the concentration-matched control, "fresh 1:50" (4 μM $PAP_{248-286}$ + 200 μM POPG, *purple*). The solid lines represent the observed frequency and the broken lines represent the Poisson uncertainty. The data shown were collected from two 30-minute measurements on a single day and are representative of two independent experiments conducted on separate days.

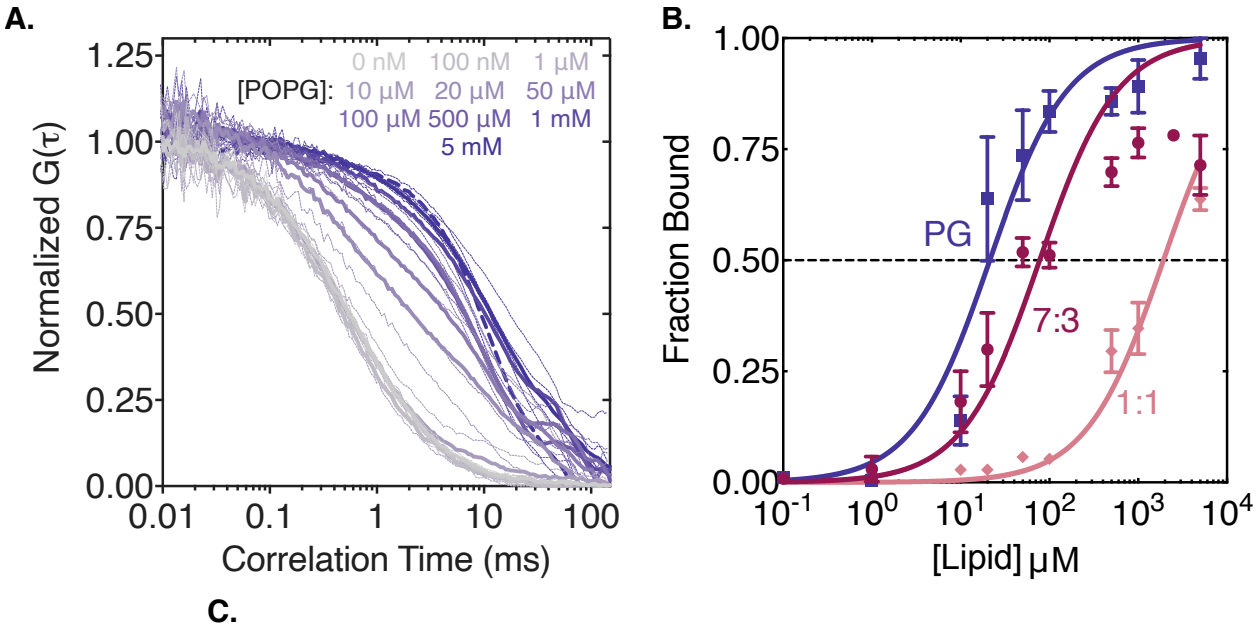

C.

Lipid composition	$K_{D,app}$ (µM)	95% CI (µM)	R-square
POPG	21	10.6 - 31.9	0.9484
7:3 POPG:POPC	78	19.5 – 136	0.8035
1:1 POPG:POPC	1924	1372-2475	0.9568

Figure 2.10: $PAP_{248-286}$-lipid binding affinity determined by FCS.

(A) Representative POPG binding titration created by adding increased concentrations of POPG into a fixed amount of fluorescently labeled $PAP_{248-286}$. A graded color scheme is used to show the autocorrelation curves from 100 nM to 5 mM POPG (*light purple* to *dark purple*). The gray curve and the dashed purple curve show $PAP_{248-286}$ and POPG liposome controls, respectively. The lines represent the mean and standard deviation of 5, 30 second measurements. These autocorrelation curves were fit with a two component fit to determine the fraction of $PAP_{248-286}$ bound at each lipid concentration and used to construct a binding curve. (B) Binding curves constructed from FCS measurements for POPG, 7:3 POPG:POPC, and 1:1 POPG:POPC. The data were fit with a one site binding equation. Data represented as the mean and SEM of at least 3 independent experiments. (C) $K_{D,app}$, 95% confidence interval (CI) of the $K_{D,app}$, and R-square of the fit of the binding curve.

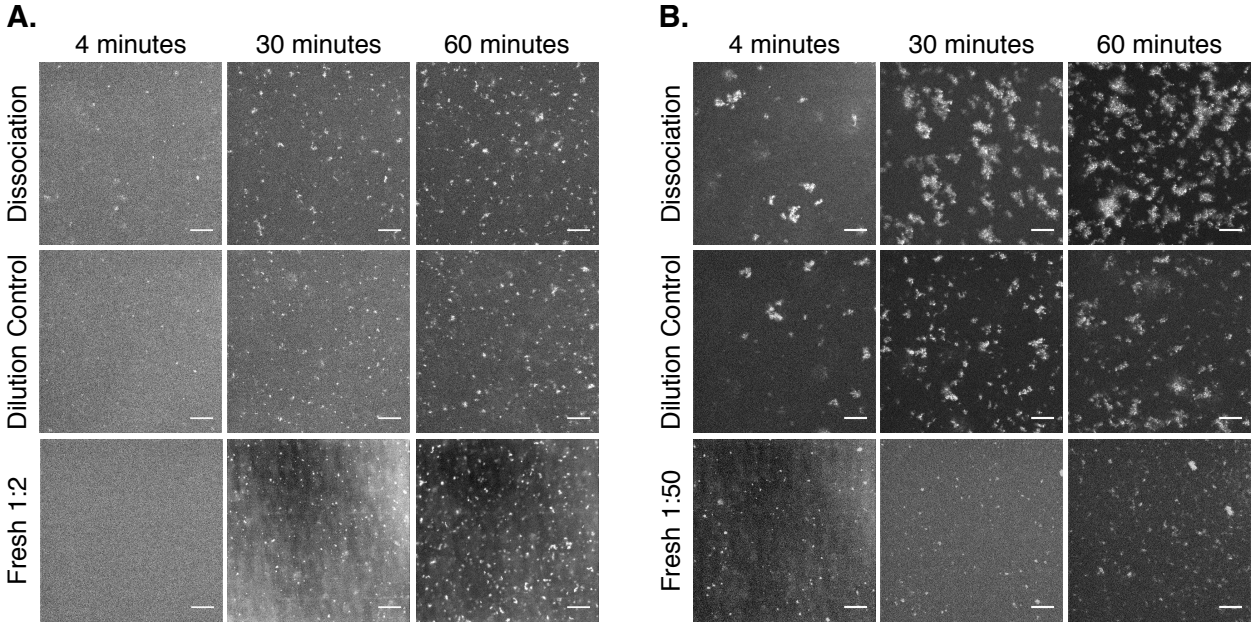

Figure 2.11: Messicle reversibility assessed by imaging at 20x magnification.

(A) Dissociation in the presence of excess $PAP_{248-286}$. Images of the dissociated messicle, "dissociation" (20 μM $PAP_{248-286}$ + 40 μM POPG), the concentration-matched control, "fresh 1:2" (20 μM $PAP_{248-286}$ + 40 μM POPG), and the "dilution control" (4 μM $PAP_{248-286}$ + 40 μM POPG) on the slide surface were collected after 4, 30, and 60 minutes. (B) Dissociation in the presence of excess POPG. Images of the dissociated messicle, "dissociation" (10 μM $PAP_{248-286}$ + 500 μM POPG), the concentration-matched control, "fresh 1:50" (10 μM $PAP_{248-286}$ + 500 μM POPG), and the "dilution control" (10 μM $PAP_{248-286}$ + 100 μM POPG) on the slide surface were collected after 4, 30, and 60 minutes. Each image is representative of seven different images taken for that condition at different positions within the droplet on the slide surface. Scale bars indicate 50 μm.

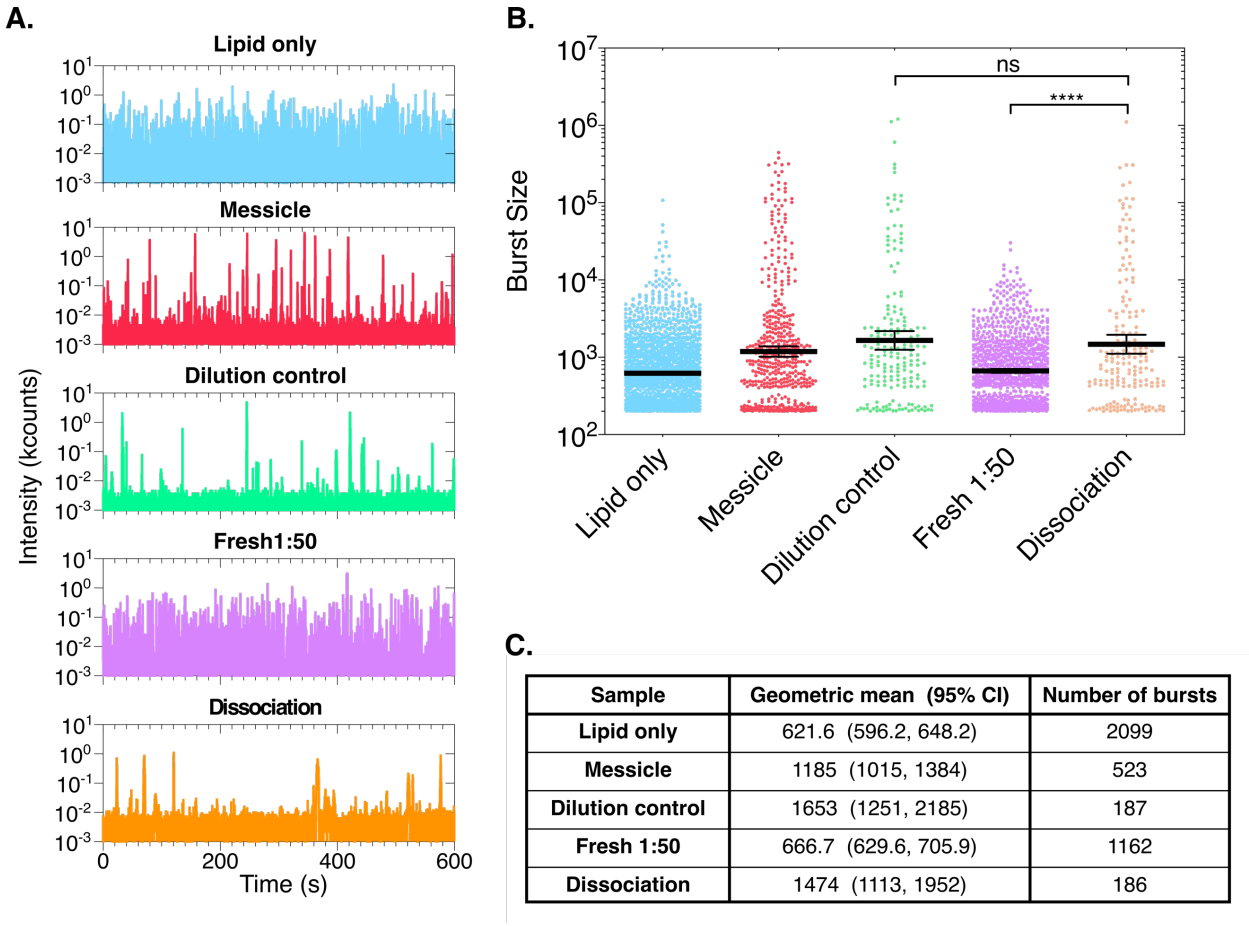

C.

Sample	Geometric mean (95% CI)	Number of bursts
Lipid only	621.6 (596.2, 648.2)	2099
Messicle	1185 (1015, 1384)	523
Dilution control	1653 (1251, 2185)	187
Fresh 1:50	666.7 (629.6, 705.9)	1162
Dissociation	1474 (1113, 1952)	186

Figure 2.12: Fluorescence burst analysis to assess messicle reversibility in the presence of excess POPG.

Each sample contained 15 nM $DIOC_{16}(3)$- doped POPG liposomes. Burst size analysis was done for the 20 μM "messicle" (20 μM $PAP_{248-286}$ + 200 μM POPG, *red*), dissociated messicle, "dissociation" (4 μM $PAP_{248-286}$ + 200 μM POPG, *orange*), "dilution control" (4 μM $PAP_{248-286}$ + 40 μM POPG, *green*), the concentration-matched control, "fresh 1:50" (4 μM $PAP_{248-286}$ + 200 μM POPG, *purple*), and "lipid only" control (200 μM POPG, *blue*). (A) Raw fluorescence intensity traces, collected using a 10 ms binning time over 10 minutes. (B) Each point represents a burst collected over two 30-minute replicate measurements from one day. The results were similar across independent experiments from two separate days. Bars show the geometric mean and 95% confidence intervals (CI), with numerical values and the number of bursts given in (C). ns, no statistically significant difference; ****P <0.0001 (Kolmogorov-Smirnov test).

2.7 REFERENCES

1. Nogales, E. 2000. Structural Insights into Microtubule Function. *Annu. Rev. Biochem.* 69:277–302.
2. Dominguez, R., and K.C. Holmes. 2011. Actin structure and function. *Annu. Rev. Biophys.* 40:169–86.
3. Sipe, J.D., and A.S. Cohen. 2000. Review: History of the amyloid fibril. *J. Struct. Biol.* 130:88–98.
4. O'Connell, J.D., A. Zhao, A.D. Ellington, and E.M. Marcotte. 2012. Dynamic Reorganization of Metabolic Enzymes into Intracellular Bodies. *Annu. Rev. Cell Dev. Biol.* 28:89–111.
5. Hyman, A.A., C.A. Weber, and F. Jülicher. 2014. Liquid-Liquid Phase Separation in Biology. *Annu. Rev. Cell Dev. Biol.* 30:39–58.
6. Alberti, S. 2017. Phase separation in biology. *Curr. Biol.* 27:R1097–R1102.
7. Standart, N., and D. Weil. 2018. P-Bodies: Cytosolic Droplets for Coordinated mRNA Storage. *Trends Genet.* 34:612–626.
8. Pulawski, W., U. Ghoshdastider, V. Andrisano, and S. Filipek. 2012. Ubiquitous amyloids. *Appl. Biochem. Biotechnol.* 166:1626–1643.
9. Caughey, B., and P.T. Lansbury. 2003. Protofibrils , Pores, Fibrils, and Neurodegeneration: Separating the Responsible Protein Aggregates from The Innocent Bystanders. *Annu. Rev. Neurosci.* 26:267–298.
10. Eisenberg, D., and M. Jucker. 2012. The amyloid state of proteins in human diseases. *Cell*. 148:1188–1203.
11. Knowles, T.P.J., M. Vendruscolo, and C.M. Dobson. 2014. The amyloid state and its association with protein misfolding diseases. *Nat. Rev. Mol. Cell Biol.* 15:384–396.
12. Maji, S.K., M.H. Perrin, M.R. Sawaya, S. Jessberger, K. Vadodaria, R.A. Rissman, P.S. Singru, K.P.R. Nilsson, R. Simon, D. Schubert, D. Eisenberg, J. Rivier, P. Sawchenko, W. Vale, and R. Riek. 2009. Functional amyloids as natural storage of peptide hormones in pituitary secretory granules. *Science (80-.).* 325:328–32.
13. Last, N.B., E. Rhoades, and A.D. Miranker. 2011. Islet amyloid polypeptide demonstrates a persistent capacity to disrupt membrane integrity. *Proc Natl Acad Sci U S A*. 108:9460–9465.
14. Hirakura, Y., I. Carreras, J.D. Sipe, and B.L. Kagan. 2002. Channel formation by serum amyloid A: a potential mechanism for amyloid pathogenesis and host defense. *Amyloid*. 9:13–23.
15. Romero, D., C. Aguilar, R. Losick, and R. Kolter. 2010. Amyloid fibers provide structural integrity to Bacillus subtilis biofilms. *Proc. Natl. Acad. Sci.* 107:2230–2234.
16. Chapman, M.R., S. Normark, and S.J. Hultgren. 2009. Amyloid Fiber Formation Role of Escherichia coli Curli Operons in Directing Amyloid Fiber Formation. *Science (80-.).* 851:851–856.
17. Kumar, D.K.V., S.H. Choi, K.J. Washicosky, W.A. Eimer, S. Tucker, J. Ghofrani, A. Lefkowitz, G. McColl, L.E. Goldstein, R.E. Tanzi, and R.D. Moir. 2016. Amyloid-β peptide protects against microbial infection in mouse and worm models of Alzheimer's disease. *Sci. Transl. Med.* 8:340ra72.
18. Korshavn, K.J., C. Satriano, Y. Lin, R. Zhang, M. Dulchavsky, A. Bhunia, M.I. Ivanova, Y.H. Lee, C. La Rosa, M.H. Lim, and A. Ramamoorthy. 2017. Reduced lipid bilayer thickness regulates the aggregation and cytotoxicity of amyloid-β. *J. Biol. Chem.* 292:4638–4650.

19. Viennet, T., M.M. Wördehoff, B. Uluca, C. Poojari, H. Shaykhalishahi, D. Willbold, B. Strodel, H. Heise, A.K. Buell, W. Hoyer, and M. Etzkorn. 2018. Structural insights from lipid-bilayer nanodiscs link α-Synuclein membrane-binding modes to amyloid fibril formation. *Commun. Biol.* 1:1–12.

20. Zhao, H., E.K.J. Tuominen, and P.K.J. Kinnunen. 2004. Formation of amyloid fibers triggered by phosphatidylserine-containing membranes. *Biochemistry*. 43:10302–10307.

21. Knight, J.D., and A.D. Miranker. 2004. Phospholipid catalysis of diabetic amyloid assembly. *J. Mol. Biol.* 341:1175–1187.

22. Elbaum-Garfinkle, S., T. Ramlall, and E. Rhoades. 2010. The role of the lipid bilayer in tau aggregation. *Biophys. J.* 98:2722–2730.

23. Terakawa, M.S., Y.H. Lee, M. Kinoshita, Y. Lin, T. Sugiki, N. Fukui, T. Ikenoue, Y. Kawata, and Y. Goto. 2018. Membrane-induced initial structure of α-synuclein control its amyloidogenesis on model membranes. *Biochim. Biophys. Acta - Biomembr.* 1860:757–766.

24. Falke, M., J. Victor, M.M. Wördehoff, A. Peduzzo, T. Zhang, G.F. Schröder, A.K. Buell, W. Hoyer, and M. Etzkorn. 2019. α-Synuclein-derived lipoparticles in the study of α-Synuclein amyloid fibril formation. *Chem. Phys. Lipids*. 220:57–65.

25. Gorbenko, G.P., and P.K.J. Kinnunen. 2006. The role of lipid-protein interactions in amyloid-type protein fibril formation. *Chem. Phys. Lipids*. 141:72–82.

26. Burke, K.A., E.A. Yates, and J. Legleiter. 2013. Biophysical Insights into How Surfaces, Including Lipid Membranes, Modulate Protein Aggregation Related to Neurodegeneration. *Front. Neurol.* 4:1–17.

27. Brown, J.W.P., G. Meisl, T.P.J. Knowles, A.K. Buell, C.M. Dobson, and C. Galvagnion. 2018. Kinetic barriers to α-synuclein protofilament formation and conversion into mature fibrils. *Chem. Commun.* 54:7854–7857.

28. Gellermann, G.P., T.R. Appel, A. Tannert, A. Radestock, P. Hortschansky, V. Schroeckh, C. Leisner, T. Lütkepohl, S. Shtrasburg, C. Röcken, M. Pras, R.P. Linke, S. Diekmann, and M. Fändrich. 2005. Raft lipids as common components of human extracellular amyloid fibrils. *Proc. Natl. Acad. Sci. U. S. A.* 102:6297–6302.

29. Jayaraman, S., D.L. Gantz, C. Haupt, and O. Gursky. 2017. Serum amyloid A forms stable oligomers that disrupt vesicles at lysosomal pH and contribute to the pathogenesis of reactive amyloidosis. *Proc. Natl. Acad. Sci. U. S. A.* 114:E6507–E6515.

30. Kollmer, M., K. Meinhardt, C. Haupt, F. Liberta, M. Wulff, J. Linder, L. Handl, L. Heinrich, C. Loos, M. Schmidt, T. Syrovets, T. Simmet, P. Westermark, G.T. Westermark, U. Horn, V. Schmidt, P. Walther, and M. Fändrich. 2016. Electron tomography reveals the fibril structure and lipid interactions in amyloid deposits. *Proc. Natl. Acad. Sci. U. S. A.* 113:5604–5609.

31. Galvagnion, C., D. Topgaard, K. Makasewicz, A.K. Buell, S. Linse, E. Sparr, and C.M. Dobson. 2019. Lipid dynamics and phase transition within α-synuclein amyloid fibrils. *J. Phys. Chem. Lett.* 10:7872–7877.

32. Sciacca, M.F.M., S.A. Kotler, J.R. Brender, J. Chen, D.K. Lee, and A. Ramamoorthy. 2012. Two-step mechanism of membrane disruption by Aβ through membrane fragmentation and pore formation. *Biophys. J.* 103:702–710.

33. Engel, M.F.M., L. Khemtémourian, C.C. Kleijer, H.J.D. Meeldijk, J. Jacobs, A.J. Verkleij, B. De Kruijff, J.A. Killian, and J.W.M. Höppener. 2008. Membrane damage by human islet amyloid polypeptide through fibril growth at the membrane. *Proc. Natl. Acad. Sci. U. S. A.* 105:6033–6038.

34. Schauerte, J.A., P.T. Wong, K.C. Wisser, H. Ding, D.G. Steel, and A. Gafni. 2010. Simultaneous single-molecule fluorescence and conductivity studies reveal distinct classes of Aβ species on lipid bilayers. *Biochemistry*. 49:3031–3039.

35. Mizuno, N., J. Varkey, N.C. Kegulian, B.G. Hegde, N. Cheng, R. Langen, and A.C. Steven. 2012. Remodeling of lipid vesicles into cylindrical micelles by α-synuclein in an extended α-helical conformation. *J. Biol. Chem.* 287:29301–29311.

36. Hellstrand, E., A. Nowacka, D. Topgaard, S. Linse, and E. Sparr. 2013. Membrane Lipid Co-Aggregation with α-Synuclein Fibrils. *PLoS One*. 8:1–10.

37. Galvagnion, C., A.K. Buell, G. Meisl, T.C.T. Michaels, M. Vendruscolo, T.P.J. Knowles, and C.M. Dobson. 2015. Lipid vesicles trigger α-synuclein aggregation by stimulating primary nucleation. *Nat. Chem. Biol.* 11:229–234.

38. Sparr, E., M.F.M. Engel, D. V. Sakharov, M. Sprong, J. Jacobs, B. De Kruijff, J.W.M. Höppener, and J. Antoinette Killian. 2004. Islet amyloid polypeptide-induced membrane leakage involves uptake of lipids by forming amyloid fibers. *FEBS Lett.* 577:117–120.

39. Bode, D.C., M. Freeley, J. Nield, M. Palma, and J.H. Viles. 2019. Amyloid-β oligomers have a profound detergent-like effect on lipid membrane bilayers, imaged by atomic force and electron microscopy. *J. Biol. Chem.* 294:7566–7572.

40. Ait-Bouziad, N., G. Lv, A.L. Mahul-Mellier, S. Xiao, G. Zorludemir, D. Eliezer, T. Walz, and H.A. Lashuel. 2017. Discovery and characterization of stable and toxic Tau/phospholipid oligomeric complexes. *Nat. Commun.* 8:1–16.

41. Varkey, J., N. Mizuno, B.G. Hegde, N. Cheng, A.C. Steven, and R. Langen. 2013. A-Synuclein Oligomers With Broken Helical Conformation Form Lipoprotein Nanoparticles. *J. Biol. Chem.* 288:17620–17630.

42. Zasloff, M. 2002. Antimicrobial Peptides of Multicellular Organisms. *Nature*. 415:389–395.

43. Chu, H., M. Pazgier, G. Jung, S. Nuccio, P.A. Castillo, M.F. de Jong, M.G. Winter, S.E. Winter, J. Wehkamp, B. Shen, N.H. Salzman, M.A. Underwood, R.M. Tsolis, G.M. Young, W. Lu, R.I. Lehrer, A.J. Bäumler, and C.L. Bevins. 2012. Human α-defensin 6 promotes mucosal innate immunity through self-assembled peptide nanonets. *Science*. 337:477–81.

44. Fehlbaum, P., P. Bulet, S. Chernysh, J.P. Briand, J.P. Roussel, L. Letellier, C. Hetru, and J.A. Hoffmann. 1996. Structure-activity analysis of thanatin, a 21-residue inducible insect defense peptide with sequence homology to frog skin antimicrobial peptides. *Proc. Natl. Acad. Sci.* 93:1221–1225.

45. Raschig, J., D. Mailänder-Sánchez, A. Berscheid, J. Berger, A.A. Strömstedt, L.F. Courth, N.P. Malek, H. Brötz-Oesterhelt, and J. Wehkamp. 2017. Ubiquitously expressed Human Beta Defensin 1 (hBD1) forms bacteria-entrapping nets in a redox dependent mode of action. *PLoS Pathog.* 13:1–18.

46. Soscia, S.J., J.E. Kirby, K.J. Washicosky, S.M. Tucker, M. Ingelsson, B. Hyman, M.A. Burton, L.E. Goldstein, S. Duong, R.E. Tanzi, and R.D. Moir. 2010. The Alzheimer's disease-associated amyloid beta-protein is an antimicrobial peptide. *PLoS One*. 5:1–10.

47. Torrent, M., D. Pulido, M.V. Nogués, and E. Boix. 2012. Exploring New Biological Functions of Amyloids: Bacteria Cell Agglutination Mediated by Host Protein Aggregation. *PLoS Pathog.* 8:1–8.

48. Jang, H., F.T. Arce, M. Mustata, S. Ramachandran, R. Capone, R. Nussinov, and R. Lal. 2011. Antimicrobial protegrin-1 forms amyloid-like fibrils with rapid kinetics suggesting a functional link. *Biophys. J.* 100:1775–1783.

49. Reddy, K.V.R., R.D. Yedery, and C. Aranha. 2004. Antimicrobial peptides: premises and promises. *Int. J. Antimicrob. Agents*. 24:536–47.

50. Tsai, P.W., C.Y. Yang, H.T. Chang, and C.Y. Lan. 2011. Human antimicrobial peptide LL-37 inhibits adhesion of Candida albicans by interacting with yeast cell-wall carbohydrates. *PLoS One*. 6:1–11.

51. Last, N.B., D.E. Schlamadinger, and A.D. Miranker. 2013. A common landscape for membrane active peptides. *Protein Sci.* 22:870–882.

52. Moir, R.D., R. Lathe, and R.E. Tanzi. 2018. The antimicrobial protection hypothesis of Alzheimer's disease. *Alzheimer's Dement.* 14:1602–1614.

53. Spitzer, P., M. Condic, M. Herrmann, T.J. Oberstein, M. Scharin-mehlmann, D.F. Gilbert, O. Friedrich, T. Grömer, J. Kornhuber, R. Lang, and J.M. Maler. 2016. Amyloidogenic amyloid- β -peptide variants induce microbial agglutination and exert antimicrobial activity. *Sci. Rep.* 6:1–11.

54. White, M.R., R. Kandel, S. Tripathi, D. Condon, L. Qi, J. Taubenberger, and K.L. Hartshorn. 2014. Alzheimer's associated β-Amyloid protein inhibits influenza a virus and modulates viral interactions with phagocytes. *PLoS One*. 9:1–9.

55. Tecle, T., M.R. White, D. Gantz, E.C. Crouch, and K.L. Hartshorn. 2007. Human neutrophil defensins increase neutrophil uptake of influenza A virus and bacteria and modify virus-induced respiratory burst responses. *J. Immunol.* 178:8046–52.

56. Brown, J.S., Z.J. Mohamed, C.M. Artim, D.N. Thornlow, J.F. Hassler, V.P. Rigoglioso, S. Daniel, and C.A. Alabi. 2018. Antibacterial isoamphipathic oligomers highlight the importance of multimeric lipid aggregation for antibacterial potency. *Commun. Biol.* 1:1–11.

57. Kvansakul, M., F.T. Lay, C.G. Adda, P.K. Veneer, A.A. Baxter, T.K. Phan, I.K.H. Poon, and M.D. Hulett. 2016. Binding of phosphatidic acid by NsD7 mediates the formation of helical defensin-lipid oligomeric assemblies and membrane permeabilization. *Proc. Natl. Acad. Sci. U. S. A.* 113:11202–11207.

58. Chieng, Y.Y., and S.B. Chen. 2011. Complexation of cationic polyelectrolyte with anionic phospholipid vesicles: Concentration, molecular weight and salt effects. *J. Colloid Interface Sci.* 354:226–233.

59. Volodkin, D., V. Ball, P. Schaaf, J.C. Voegel, and H. Mohwald. 2007. Complexation of phosphocholine liposomes with polylysine. Stabilization by surface coverage versus aggregation. *Biochim. Biophys. Acta - Biomembr.* 1768:280–290.

60. Yaroslavov, A.A., A.A. Efimova, V.I. Lobyshev, and V.A. Kabanov. 2002. Reversibility of structural rearrangements in the negative vesicular membrane upon electrostatic adsorption/desorption of the polycation. *Biochim. Biophys. Acta - Biomembr.* 1560:14–24.

61. Tsogas, I., D. Tsiourvas, G. Nounesis, and C.M. Paleos. 2005. Interaction of poly-L-arginine with dihexadecyl phosphate/phosphatidylcholine liposomes. *Langmuir*. 21:5997–6001.

62. Kwolek, U., D. Jamróz, M. Janiczek, M. Nowakowska, P. Wydro, and M. Kepczynski. 2016. Interactions of Polyethylenimines with Zwitterionic and Anionic Lipid Membranes. *Langmuir*. 32:5004–5018.

63. Robert, É., T. Lefèvre, M. Fillion, B. Martial, J. Dionne, and M. Auger. 2015. Mimicking and Understanding the Agglutination Effect of the Antimicrobial Peptide Thanatin Using Model Phospholipid Vesicles. *Biochemistry*. 54:3932–3941.

64. Easterhoff, D., F. Ontiveros, L.R. Brooks, Y. Kim, B. Ross, J.N. Silva, J.S. Olsen, C. Feng, D.J. Hardy, P.M. Dunman, and S. Dewhurst. 2013. Semen-derived enhancer of viral infection (SEVI) binds bacteria, enhances bacterial phagocytosis by macrophages, and can protect against vaginal infection by a sexually transmitted bacterial pathogen. *Antimicrob Agents Chemother*. 57:2443–2450.

65. Brender, J.R., K. Hartman, L.M. Gottler, M.E. Cavitt, D.W. Youngstrom, and A. Ramamoorthy. 2009. Helical conformation of the SEVI precursor peptide PAP248-286, a dramatic enhancer of HIV infectivity, promotes lipid aggregation and fusion. *Biophys. J.* 97:2474–2483.

66. Brender, J.R., R.P.R. Nanga, N. Popovych, R. Soong, P.M. Macdonald, and A. Ramamoorthy. 2011. The amyloidogenic SEVI precursor, PAP248-286, is highly unfolded in solution despite an underlying helical tendency. *Biochim. Biophys. Acta - Biomembr.* 1808:1161–1169.

67. Nanga, R.P.R., J.R. Brender, S. Vivekanandan, N. Popovych, and A. Ramamoorthy. 2009. NMR structure in a membrane environment reveals putative amyloidogenic regions of the SEVI precursor peptide PAP248-286. *J. Am. Chem. Soc.* 131:17972–17979.

68. Nguyen, K.T. 2016. In Situ Investigation of Peptide–Lipid Interaction Between PAP248–286 and Model Cell Membranes. *J. Membr. Biol.*

69. Münch, J., E. Rücker, L. Ständker, K. Adermann, C. Goffinet, M. Schindler, S. Wildum, R. Chinnadurai, D. Rajan, A. Specht, G. Giménez-Gallego, P.C. Sánchez, D.M. Fowler, A. Koulov, J.W. Kelly, W. Mothes, J.C. Grivel, L. Margolis, O.T. Keppler, W.G. Forssmann, and F. Kirchhoff. 2007. Semen-derived amyloid fibrils drastically enhance HIV infection. *Cell*. 131:1059–1071.

70. Torres, L., T. Ortiz, and Q. Tang. 2015. Enhancement of herpes simplex virus (HSV) infection by seminal plasma and semen amyloids implicates a new target for the prevention of HSV infection. *Viruses*. 7:2057–2073.

71. Bart, S.M., C. Cohen, J.M. Dye, J. Shorter, and P. Bates. 2018. Enhancement of Ebola virus infection by seminal amyloid fibrils. *Proc. Natl. Acad. Sci.* 115:7410–7415.

72. Roan, N.R., N. Sandi-Monroy, N. Kohgadai, S.M. Usmani, K.G. Hamil, J. Neidleman, M. Montano, L. Ständker, A. Röcker, M. Cavrois, J. Rosen, K. Marson, J.F. Smith, C.D. Pilcher, F. Gagsteiger, O. Sakk, M. O'Rand, P. V Lishko, F. Kirchhoff, J. Münch, and W.C. Greene. 2017. Semen amyloids participate in spermatozoa selection and clearance. *Elife*. 6:1–22.

73. Tang, Q., N.R. Roan, and Y. Yamamura. 2013. Seminal plasma and semen amyloids enhance cytomegalovirus infection in cell culture. *J Virol*. 87:12583–12591.

74. Roan, N.R., J. Münch, N. Arhel, W. Mothes, J. Neidleman, A. Kobayashi, K. Smith-McCune, F. Kirchhoff, and W.C. Greene. 2009. The cationic properties of SEVI underlie its ability to enhance human immunodeficiency virus infection. *J. Virol.* 83:73–80.

75. Ronquist, G., and I. Brody. 1985. The prostasome: its secretion and function in man. *BBA - Rev. Biomembr.* 822:203–218.

76. Huggins, C., W.W. Scott, and J.H. Heinen. 1942. Chemical Composition of Human Semen and of the Secretions of the Prostate and Seminal Vesicles. *Am. J. Physiol. Content*. 136:467–473.

77. Owen, D.H., and D.F. Katz. 2005. A review of the physical and chemical properties of human semen and the formulation of a semen simulant. *J. Androl.* 26:459–469.

78. Chen, P.S., T.Y. Toribara, and H. Warner. 1956. Microdetermination of Phosphorus. *Anal. Chem.* 28:1756–1758.

79. Fiske, C.H., and Y. Subbarow. 1925. The Colorimetric Determination of Phosphorus. *J. Biol. Chem.* 66:374–389.

80. Chifflet, S., A. Torriglia, R. Chiesa, and S. Tolosa. 1988. A method for the determination of inorganic phosphate in the presence of labile organic phosphate and high concentrations of protein: Application to lens ATPases. *Anal. Biochem.* 168:1–4.

81. Edelstein, A.D., M.A. Tsuchida, N. Amodaj, H. Pinkard, R.D. Vale, and N. Stuurman. 2014. Advanced methods of microscope control using μManager software. *J. Biol. Methods*. 1:1–10.

82. Edelstein, A., N. Amodaj, K. Hoover, R. Vale, and N. Stuurman. 2010. Computer Control of Microscopes Using μManager. *Curr. Protoc. Mol. Biol.* 92:14.20.1-14.20.17.

83. Schindelin, J., I. Arganda-carreras, E. Frise, V. Kaynig, M. Longair, T. Pietzsch, S. Preibisch, C. Rueden, S. Saalfeld, B. Schmid, J. Tinevez, D.J. White, V. Hartenstein, K. Eliceiri, P. Tomancak, and A. Cardona. 2012. Fiji : an open-source platform for biological-image analysis. *Nat. Methods*. 9:676–682.

84. Haynes, W.M., D.R. Lide, and T.J. Bruno. CRC Handbook of Chemistry and Physics. 97th ed.

85. Micsonai, A., F. Wien, L. Kernya, Y.H. Lee, Y. Goto, M. Réfrégiers, and J. Kardos. 2015. Accurate secondary structure prediction and fold recognition for circular dichroism spectroscopy. *Proc. Natl. Acad. Sci. U. S. A.* 112:E3095–E3103.

86. Micsonai, A., F. Wien, É. Bulyáki, J. Kun, É. Moussong, Y.H. Lee, Y. Goto, M. Réfrégiers, and J. Kardos. 2018. BeStSel: A web server for accurate protein secondary structure prediction and fold recognition from the circular dichroism spectra. *Nucleic Acids Res.* 46:W315–W322.

87. Abraham, M.J., T. Murtola, R. Schulz, S. Páll, J.C. Smith, B. Hess, and E. Lindah. 2015. Gromacs: High performance molecular simulations through multi-level parallelism from laptops to supercomputers. *SoftwareX*. 1–2:19–25.

88. Klauda, J.B., R.M. Venable, J.A. Freites, J.W. O'Connor, D.J. Tobias, C. Mondragon-Ramirez, I. Vorobyov, A.D. MacKerell, and R.W. Pastor. 2010. Update of the CHARMM All-Atom Additive Force Field for Lipids: Validation on Six Lipid Types. *J. Phys. Chem. B*. 114:7830–7843.

89. Best, R.B., X. Zhu, J. Shim, P.E.M. Lopes, J. Mittal, M. Feig, and A.D. MacKerell. 2012. Optimization of the additive CHARMM all-atom protein force field targeting improved sampling of the backbone φ, ψ and side-chain χ1 and χ2 Dihedral Angles. *J. Chem. Theory Comput.* 8:3257–3273.

90. Wagle, S., V.N. Georgiev, T. Robinson, R. Dimova, R. Lipowsky, and A. Grafmüller. 2019. Interaction of SNARE mimetic peptides with lipid bilayers: Effects of secondary structure, bilayer composition and lipid anchoring. *Sci. Rep.* 9:1–14.

91. Lee, J., X. Cheng, J.M. Swails, M.S. Yeom, P.K. Eastman, J.A. Lemkul, S. Wei, J. Buckner, J.C. Jeong, Y. Qi, S. Jo, V.S. Pande, D.A. Case, C.L. Brooks, A.D. MacKerell, J.B. Klauda, and W. Im. 2016. CHARMM-GUI Input Generator for NAMD, GROMACS, AMBER, OpenMM, and CHARMM/OpenMM Simulations Using the CHARMM36 Additive Force Field. *J. Chem. Theory Comput.* 12:405–413.

92. Greenfield, N. 2007. Using circular dichroism spectra to estimate protein secondary structure. *Nat. Protoc.* 1:2876–2890.

93. Fabrick, J.A., J.E. Baker, and M.R. Kanost. 2004. Innate immunity in a pyralid moth: Functional evaluation of domains from a β-1,3-glucan recognition protein. *J. Biol. Chem.* 279:26605–26611.

94. Poon, C., M. Sarkar, and E.J. Chung. 2017. Synthesis of monocyte-targeting peptide amphiphile micelles for imaging of atherosclerosis. *J. Vis. Exp.* 2017:1–9.

95. Miles, A.J., and B.A. Wallace. 2016. Circular dichroism spectroscopy of membrane proteins. *Chem. Soc. Rev.* 45:4859–4872.

96. Biancalana, M., and S. Koide. 2010. Molecular mechanism of Thioflavin-T binding to amyloid fibrils. *Biochim. Biophys. Acta - Proteins Proteomics*. 1804:1405–1412.

97. Wolfe, L.S., M.F. Calabrese, A. Nath, D. V Blaho, A.D. Miranker, and Y. Xiong. 2010. Protein-induced photophysical changes to the amyloid indicator dye thioflavin T. *Proc. Natl. Acad. Sci. U. S. A.* 107:16863–16868.

98. Hortschansky, P., V. Schroeckh, T. Christopeit, G. Zandomeneghi, and M. Fandrich. 2005. The aggregation kinetics of Alzheimer's B-amyloid peptide is controlled by stochastic nucleation. *Protein Sci.* 14:1753–1759.

99. Gregory, J. 1987. Flocculation by polymers and polyelectrolytes. *Solid/Liquid Dispersions*. 163–180.

100. Dave, N., and J. Liu. 2011. Programmable assembly of DNA-functionalized liposomes by DNA. *ACS Nano*. 5:1304–1312.

101. Vabbilisetty, P., and X.L. Sun. 2014. Liposome surface functionalization based on different anchoring lipids via Staudinger ligation. *Org. Biomol. Chem.* 12:1237–1244.

102. Ding, X., J. Janjanam, A. Tiwari, M. Thompson, and P.A. Heiden. 2014. Peptide-Directed Self-Assembly of Functionalized Polymeric Nanoparticles Part I: Design and Self-Assembly of Peptide-Copolymer Conjugates into Nanoparticle Fibers and 3D Scaffolds. *Macromol. Biosci.* 14:853–871.

103. Si, S., and T.K. Mandal. 2007. pH-controlled reversible assembly of peptide-functionalized gold nanoparticles. *Langmuir*. 23:190–195.

104. Usmani, S.M., O. Zirafi, J.A. Muller, N.L. Sandi-Monroy, J.K. Yadav, C. Meier, T. Weil, N.R. Roan, W.C. Greene, P. Walther, K.P. Nilsson, P. Hammarstrom, R. Wetzel, C.D. Pilcher, F. Gagsteiger, M. Fandrich, F. Kirchhoff, and J. Munch. 2014. Direct visualization of HIV-enhancing endogenous amyloid fibrils in human semen. *Nat Commun*. 5:3508.

105. Yáñez-Mó, M., P.R.-M. Siljander, Z. Andreu, A.B. Zavec, F.E. Borràs, E.I. Buzas, K. Buzas, E. Casal, F. Cappello, J. Carvalho, E. Colás, A. Cordeiro-da Silva, S. Fais, J.M. Falcon-Perez, I.M. Ghobrial, B. Giebel, M. Gimona, M. Graner, I. Gursel, M. Gursel, N.H.H. Heegaard, A. Hendrix, P. Kierulf, K. Kokubun, M. Kosanovic, V. Kralj-Iglic, E.-M. Krämer-Albers, S. Laitinen, C. Lässer, T. Lener, E. Ligeti, A. Linē, G. Lipps, A. Llorente, J. Lötvall, M. Manček-Keber, A. Marcilla, M. Mittelbrunn, I. Nazarenko, E.N.M. Nolte-'t Hoen, T.A. Nyman, L. O'Driscoll, M. Olivan, C. Oliveira, É. Pállinger, H.A. Del Portillo, J. Reventós, M. Rigau, E. Rohde, M. Sammar, F. Sánchez-Madrid, N. Santarém, K. Schallmoser, M.S. Ostenfeld, W. Stoorvogel, R. Stukelj, S.G. Van der Grein, M.H. Vasconcelos, M.H.M. Wauben, and O. De Wever. 2015. Biological properties of extracellular vesicles and their physiological functions. *J. Extracell. vesicles*. 4:27066.

106. Ronquist, G., B.O. Nilsson, and S. Hjertën. 1990. Interaction between prostasomes and spermatozoa from human semen. *Arch. Androl.* 24:147–57.

107. Brender, J.R., J. Krishnamoorthy, G.M.L. Messina, A. Deb, S. Vivekanandan, C. La Rosa, J.E. Penner-Hahn, and A. Ramamoorthy. 2013. Zinc stabilization of prefibrillar oligomers of human islet amyloid polypeptide. *Chem. Commun. (Camb).* 49:3339–3341.

108. Skotland, T., K. Sagini, K. Sandvig, and A. Llorente. 2020. An emerging focus on lipids in extracellular vesicles. *Adv. Drug Deliv. Rev.*

109. Brouwers, J.F., M. Aalberts, J.W.A. Jansen, G. van Niel, M.H. Wauben, T.A.E. Stout, J.B. Helms, and W. Stoorvogel. 2013. Distinct lipid compositions of two types of human prostasomes. *Proteomics*. 13:1660–1666.

110. Walters, J.L.H., B.M. Gadella, J.M. Sutherland, B. Nixon, and E.G. Bromfield. 2020. Male Infertility: Shining a Light on Lipids and Lipid-Modulating Enzymes in the Male Germline. *J. Clin. Med.* 9:327.

111. Hines, K.M., A. Waalkes, K. Penewit, E.A. Holmes, S.J. Salipante, B.J. Werth, and L. Xu. 2017. Characterization of the Mechanisms of Daptomycin Resistance among Gram-Positive Bacterial Pathogens by Multidimensional Lipidomics. *mSphere*. 2.

112. Lee, T.H., V. Hofferek, F. Separovic, G.E. Reid, and M.I. Aguilar. 2019. The role of bacterial lipid diversity and membrane properties in modulating antimicrobial peptide activity and drug resistance. *Curr. Opin. Chem. Biol.* 52:85–92.

113. Milutinovic, B., N. Mitic, J. Roncevic, S. Goc, and M. Jankovic. 2016. Glycome complexity of human seminal plasma high molecular mass components: Evaluation of the contribution of acid-soluble glycoproteins/mucins and extracellular vesicles. *Arch. Biochem. Biophys.* 609:20–30.

114. Gerlach, J.Q., and M.D. Griffin. 2016. Getting to know the extracellular vesicle glycome. *Mol. Biosyst.* 12:1071–1081.

115. Tecle, E., and P. Gagneux. 2015. Sugar-coated sperm: Unraveling the functions of the mammalian sperm glycocalyx. *Mol. Reprod. Dev.* 82:635–650.

116. Joo, H.S., C.I. Fu, and M. Otto. 2016. Bacterial strategies of resistance to antimicrobial peptides. *Philos. Trans. R. Soc. B Biol. Sci.* 371.

117. Pulido, D., M. Moussaoui, D. Andreu, M.V. Nogués, M. Torrent, and E. Boix. 2012. Antimicrobial action and cell agglutination by the eosinophil cationic protein are modulated by the cell wall lipopolysaccharide structure. *Antimicrob. Agents Chemother.* 56:2378–2385.

Chapter 3. PROBING THE VESICLE LEAKAGE MECHANISM OF $PAP_{248-286}$ WITH FLUORESCENCE LIFETIME DISTRIBUTION ANALYSIS

[Adapted from Vane, E.W., and A. Nath. 2021. Probing the vesicle leakage mechanism of $PAP_{248-286}$ with fluorescence lifetime distribution analysis. (manuscript to be submitted for publication)]

Abstract:

Membrane permeabilization is important to the beneficial activities of antimicrobial peptides and also the toxicity of amyloid-forming peptides. Therefore, having a more detailed understanding of the mechanisms that these peptides use to permeabilize membranes could be useful in the design of antimicrobials with improved efficacy or potential therapeutic interventions to treat amyloid-associated diseases. We therefore chose to study the membrane permeabilizing activities of the amyloid-forming peptide fragment of the protein prostatic acid phosphatase, $PAP_{248-286}$. $PAP_{248-286}$ disrupts lipid membranes *in vitro* and displays antimicrobial activity through an agglutination mechanism, but interestingly has not been observed to kill bacteria directly when tested against a panel of bacteria. To learn more about $PAP_{248-286}$-induced membrane permeabilization, we combined classical fluorescence dequenching experiments with fluorescence lifetime measurements of liposomes filled with the self-quenching dye calcein. The fluorescence lifetime of calcein is a probe of the local environment within liposomes, enabling us to directly distinguish all-or-none leakage, wherein strong leakage events cause some vesicles to lose all of their contents, from graded leakage, wherein weak leakage events cause all of the vesicles to lose some of their contents, or from more complex mixed mechanisms. We improved the analysis of the fluorescence

lifetime decays by incorporating a gamma distribution to account for heterogeneity in the liposome population in a robust and physically reasonable manner. The combination of dequenching and fluorescence lifetime distribution analysis suggested that $PAP_{248-286}$-induced membrane disruption is consistent with a graded leakage mechanism, suggesting it causes transient, weak leakage events in liposomes. This could explain its lack of detectable direct antibacterial activity and highlights the importance of understanding mechanism to the study of peptide-induced membrane permeabilization.

3.1 Statement of Significance

While membrane disruption induced by peptides is an important and ubiquitous phenomenon, our knowledge of underlying mechanism and the connection to biology is incomplete. Here, we study $PAP_{248-286}$, an amyloid-forming seminal peptide that potently disrupts anionic lipid membranes *in vitro* yet does not display any direct cell-killing activity. We apply fluorescence lifetime analysis, a robust and direct way of assessing kinetic leakage mechanism, to show that $PAP_{248-286}$ causes transient membrane disruptions *in vitro* that may be too weak to kill bacteria *in vivo*. Furthermore, by incorporating distribution analysis in the fitting of our fluorescence lifetime decays, we are able to provide stable fits that can be more widely applied to fit complex and heterogenous leakage processes.

3.2 Introduction

The ability of peptides to remodel and permeabilize membranes is important in many areas of biology. On one hand, membrane permeabilization is essential to the activity of many antimicrobial peptides (AMPs), which are found throughout nature and are integral components

of the innate immune system (1–4). There has been great interest in AMPs and their membrane permeabilizing activity due to their therapeutic potential against antibiotic-resistant bacteria (5–7). Conversely, membrane disruption is thought to be important in amyloid-associated diseases, including Alzheimer's, Parkinson's, and type II diabetes. In these diseases, the cytotoxicity of the amyloid-forming peptides is thought to be due to their membrane permeabilizing activity (8–13).

Given the great importance of membrane permeabilization in both healthy and diseased states, understanding the mechanisms underlying this activity could aid in the design of better AMPs or help to guide therapeutic approaches in the treatment of amyloid-associated diseases. Liposomes or large unilamellar vesicles (LUVs) are a controlled and simplified membrane mimetic that are often used to explore this phenomenon (3). One common framework used to study the leakage of liposomes is the distinction between all-or-none and graded mechanisms (3, 14, 15). The difference between the mechanisms is illustrated in Figure 3.1, where graded leakage results in partial leakage of all liposomes simultaneously, while all-or-none leakage results in 100% leakage of some liposomes while other liposomes remain unleaked. To understand what these mechanisms mean physically, it is helpful to distinguish these mechanisms based on the strength and duration of leakage events involved. All-or-none leakage requires that some liposomes experience a strong or long-lived leakage event, such that the time required for efflux of vesicle contents is much shorter than the lifespan of the leakage event. The leakage event in this case could be due to the formation of a large, long-lived pore or a catastrophic event that destroys the vesicle (16–20). Graded leakage, on the other hand, requires weak and transient leakage events, such that the time required for complete efflux is longer than the lifespan of a single leakage event. Transient pore formation or lipid/peptide rearrangements to relieve bilayer asymmetry have been invoked to

explain graded leakage (16, 17, 20–22), but much about this class of leakage mechanism remains unknown.

Fluorescence has been the most common way to study membrane leakage kinetics and mechanisms. These methods often take advantage of self-quenching fluorophores or dye/quencher pairs that are quenched when encapsulated in liposomes and increase in fluorescence upon efflux into the surrounding solution (3). Many different techniques have been utilized to try to distinguish between graded and all-or-none leakage mechanisms. These include fitting of fluorescence kinetics to analytical models (23), separation and quantification of leaked and unleaked dye from liposomes (14, 24, 25), and an ANTS/DPX re-quenching method wherein the addition of quencher after dye efflux can be used to infer the dye concentration within liposomes (26–28). However, these ensemble methods can be subject to simplifying assumptions (like assuming the population of liposomes are homogenous), are indirect, and time consuming. Newer techniques including single-vesicle microscopy on giant unilamellar vesicles (GUVs) produce more direct and robust measurements and provide useful insight into the stochastic nature of membrane permeabilization in these leakage mechanisms (17, 20, 29). However, a great number of GUVs need to be studied in order to establish mechanism, and the throughput of GUV studies is typically limited unless a specialized microfluidic setup is employed (18). In addition, GUVs have poorer resolution than LUVs when it comes to weak leakage events (16, 20). We therefore chose to work with LUVs and adapted an elegant fluorescence lifetime-based approach introduced by Patel *et. al.* (30) that takes advantage of the fluorescence properties of calcein. Calcein self-quenches at high concentrations, primarily via a dynamic mechanism (30), making the lifetime of vesicle-entrapped calcein a sensitive probe of leakage mechanism. The fluorescence lifetime of calcein is inversely proportional to the amount of quenching it experiences, so the lifetime of calcein in a partially-

leaked vesicle will be higher than the lifetime in an unleaked vesicle. In all-or-none leakage, where the liposomes are either full or completely leaked, the lifetime of the entrapped calcein will not change, since the extent of quenching experienced by calcein inside unleaked liposomes remains the same. For graded leakage, as the fraction of calcein leaked from the liposomes increases with changing concentrations of permeabilizing peptide, the amount of entrapped calcein decreases. This leads to less quenching and a longer fluorescent lifetime. Leakage behavior may also be more complex, with a given peptide inducing all-or-none leakage under certain conditions and graded leakage in others. It is also possible that both mechanisms occur simultaneously or that graded leakage is more heterogeneous than the ideal case. The relationship between the entrapped lifetime and the extent of leakage can be used to distinguish all-or-none from graded mechanisms or more complex scenarios, and to gain insight into the nature of the leakage events (16, 30, 31). We improve on this method by using lifetime distribution analysis to account for liposome heterogeneity (32), providing a more robust and sensitive assay, particularly at low levels of efflux.

Here, we apply this method to an amyloid-forming peptide fragment of the seminal protein prostatic acid phosphatase ($PAP_{248-286}$) that also displays membrane active properties. $PAP_{248-286}$ forms amyloid fibrils that are thought to be responsible for the large enhancement of HIV infectivity observed in seminal fluid, and therefore called semen-derived enhancer of viral infection (SEVI) (33). It is a 39-residue peptide that carries a net charge of +6 at neutral pH, and undergoes a transition from disorder to order as it is disordered in solution but forms a partial amphipathic α-helix upon binding to a lipid membrane (34–36). This binding to the membrane surface is thought to be driven by electrostatic interactions: we and other groups have shown that $PAP_{248-286}$ displays a strong preference for binding to lipid membranes that contain anionic lipids (34, 37). Similarly, Brender *et. al.* showed that its membrane-disrupting activity is also dependent

on the liposome charge. Interestingly, $PAP_{248-286}$ does not seem to penetrate the hydrophobic core of the bilayer to the same extent as other amyloid-forming peptides (34, 35). Additionally, although it displays membrane activity and has a preference for membranes with anionic lipids, $PAP_{248-286}$ does not display direct antimicrobial activity against a panel of gram-positive and -negative bacteria (38). Given the superficial nature of $PAP_{248-286}$'s interaction with membranes and its lack of direct antimicrobial activity, we chose to further investigate its leakage mechanism.

Using liposomes filled with the fluorophore calcein, we have shown that $PAP_{248-286}$-induced liposome leakage is dependent on the overall charge of the liposomes and seems to be very rapid. Fluorescence lifetime analysis showed that $PAP_{248-286}$ displays a graded leakage mechanism. This mechanism suggests that the bulk of $PAP_{248-286}$'s leakage activity is caused by stochastic and weak leakage events, with a preference for membranes containing anionic lipids, somewhat similar to the mechanism observed for the wasp venom peptides, mastoparan and mastoparan X (22). A graded leakage mechanism could also explain its lack of direct antimicrobial activity and demonstrates the importance of mechanism determination for understanding biological activity.

3.3 METHODS

3.3.1 *Materials:*

1-palmitoyl-2-oleoyl-glycero-3-phosphocholine (POPC) and 1-palmitoyl-2-oleoyl-sn-glycero-3-phospho-(1'-rac-glycerol) (POPG) were purchased from Avanti Polar Lipids, Inc. (Alabaster, AL) as a powder. Unless specified otherwise, all other reagents were purchased from Thermo Fisher Scientific (Waltham, MA) and were ACS reagent grade or better.

3.3.2 *Preparation of permeabilizing agents:*

Synthetic $PAP_{248-286}$ (sequence: GIHKQKEKSRLQGGVLVNEILNHMKRATQIPSY KKLIMY) was purchased from New England Peptides (Gardner, MA). Peptide was dissolved as received in a HEPES (4-(2-hydroxyethyl)-1-piperazineethanesulfonic acid) buffer (50 mM HEPES, 100 mM NaCl, 0.3 mM EDTA, pH 7.4), flash frozen, and stored at -80°C. The final concentration of $PAP_{248-286}$ stock was determined by absorbance at 280 nm. Stock solutions of 10% (w/v) 3-[(3-Cholamidopropyl) dimethylammonio]-1-propanesulfonate (CHAPS) and 2% (w/v) sodium dodecyl sulfate (SDS) were prepared in HEPES buffer immediately before each experiment. These stocks were diluted down to the appropriate concentration for their respective experiments.

3.3.3 *Liposome preparation:*

LUVs were prepared with either 1:1 POPC:POPG (mol:mol) or 100% POPC (Avanti Polar Lipids). Stock lipid solutions were prepared from purchased lipid powders at 19 mg/mL in chloroform and stored at -20°C for 6 months–1 year. The total phosphorous content of the lipid stocks was verified using the "Determination of Total Phosphorus" analytical procedure outlined by Avanti Polar Lipids (37, 39–41) and adapted for a Biotek Synergy HTX multi-mode plate reader (Winooski, VT).

Briefly, liposomes were prepared by measuring the appropriate amount of each lipid stock in chloroform and evaporating bulk chloroform with nitrogen gas to form lipid films. These films were left under vacuum for at least 14 hours and then hydrated with a HEPES buffer containing 50 mM HEPES, 0.3 mM EDTA, and 70 mM calcein (MP Biomedicals, Irvine, CA) at pH 7.4. The rehydrated lipid film was then subjected to 10 freeze-thaw cycles, followed by 23 passes through a mini-extruder (Avanti Polar Lipids) with a 0.1 μm polycarbonate membrane (Avanti Polar

Lipids). While extrusion is a widely used method for preparation of LUVs, a significant fraction of multilamellar vesicles can remain (42). This could be an important contributor to liposome heterogeneity. The liposomes were then separated from unencapsulated calcein using a 5 mL HiTrap desalting column (GE Healthcare, Marlborough, MA) and eluted with the calcein-free HEPES buffer. This was followed by four sequential 1:1000 dialysis steps in a 0.5 mL 7K MWCO Slide-A-Lyzer dialysis cassette (Thermo Fisher) against the calcein-free HEPES buffer at 4°C for at least four hours for each step. All other preparation steps were performed at room temperature. The final concentration of LUVs was determined using the total phosphorous assay, described earlier.

3.3.4 *Fluorimeter leakage kinetics:*

1:1 POPC:POPG or POPC liposomes were diluted down to 200 μM and 20 μL of this solution was added to 170 μL of HEPES buffer. This solution was equilibrated for 20 minutes before the addition of 10 μL of 20x the desired concentration of $PAP_{248-286}$. As soon as $PAP_{248-286}$ was added, the solution was mixed by pipetting, added to a 3 mm spectrosil quartz fluorometer cell (Starna Cells, Inc., Atascadero, CA), placed in its 3 mm cuvette compatible adaptor, and added to a Varian Cary Eclipse fluorescence spectrophotometer (Varian, Palo Alto, CA). Up to 4 cuvettes were run simultaneously at 25°C, with measurements taken every 30 seconds for 1 hour using an excitation of 495 nm and an emission of 515 nm, 2.5 nm slit widths, and a PMT detector voltage of 700 volts. 10 μL of HEPES buffer was added as a 0% control and run side-by-side with other samples to account for baseline leakage of liposomes over time.

The fraction leaked was calculated as the fluorescence of each sample at each time point divided by the average fluorescence of 20 μM liposomes in the presence of 0.1% Triton X-100 (Sigma-Aldrich, St. Louis, MO). For the kinetic measurements, the mean and standard deviation

of four independent experiments for 1:1 POPC:POPG liposomes was plotted using GraphPad Prism (GraphPad, San Diego, CA). For the endpoint values, the last value calculated from the fraction leaked kinetics was plotted against the concentration of $PAP_{248-286}$ for both 1:1 POPC:POPG and POPC liposomes.

3.3.5 *Time-correlated single photon counting (TCSPC):*

For $PAP_{248-286}$ and SDS, 1:1 POPC:POPG liposomes containing calcein were diluted so that their final concentration was 20 μM and left to equilibrate at room temperature for 20 minutes. For membrane permeabilization by CHAPS, POPC liposomes were diluted to a final concentration of 300 μM to replicate results from a previous study showing all-or-none activity (30). These liposomes were also left to equilibrate at room temperature for 20 minutes. During this time 20x the desired concentration of $PAP_{248-286}$, SDS, and CHAPS stock solutions were prepared. For three of the four independent replicates of $PAP_{248-286}$, the $PAP_{248-286}$ was first centrifuged at 21100*g* at 4°C for 10 minutes in a Sorvall Legend 21R microcentrifuge (Thermo Fisher Scientific) to remove any large aggregates. As described in Chapter 4, under similar conditions we did not observe the formation of large soluble oligomers by $PAP_{248-286}$. Each stock was then added to the equilibrated liposomes, bringing them to the desired concentration and mixed by pipetting. These mixtures were then left to incubate at room temperature for either 30 minutes for SDS or 60 minutes for $PAP_{248-286}$ and CHAPS.

The samples were then placed onto a coverslip on a home-built instrument consisting of an inverted Zeiss Axio Observer D1 (Carl Zeiss Microscopy) microscope equipped with a Picoquant PDL 828 Sepia II pulsed laser driver (PicoQuant GmbH, Berlin, Germany), Hydra-Harp 400 detection electronics (PicoQuant), and a Tau-SPAD photon counting detector (PicoQuant). The laser was passed through a 488 nm/10 nm excitation filter and collected by a 488 nm dichroic

mirror and 535 nm/70 nm emission filter (all filters from Chroma Technology Corp., Bellows Falls, VT). The neutral density filter (Thorlabs, Inc., Newton, NJ) was changed in order to keep the photon count rate below 1% of the excitation rate. 3-5 consecutive measurements of 30-90 seconds were collected, yielding fluorescence decays with at least ~10,000 counts in the highest bin. For timed TCSPC experiments with $PAP_{248-286}$, the preparation was the same but aliquots were placed onto the microscope and measured at 5, 30, 60, and 120 minutes and 3 consecutive measurements were collected for 90 seconds each. Autocorrelation and TCSPC of the fluorescence signal from the detector were performed using the HydraHarp 400 and SymphoTime 64 software (PicoQuant). The prompt was collected by performing TCSPC on 200 nM Alexa Fluor 488 NHS Ester (Life Technologies, Carlsbad, CA) in a concentrated solution, 1.3 g/mL, of Potassium Iodide (J.T. Baker, Phillipsburg, NJ).

3.3.6 *Fitting fluorescence decays collected by TCSPC:*

The fluorescence decays and prompts were imported into a modified version of the DLTReconvolution open software (43) for analysis. This package does an iterative reconvolution of the prompt with the true decay. First, the program was modified to allow the user to fix the value for the lifetime of free calcein. This value was determined to be 4.073 ns by fitting the tail of the free calcein fluorescence decay with a single component exponential decay. This lifetime was independent of the concentration of calcein and the presence of the CHAPS, SDS, and $PAP_{248-286}$ (data not shown) and was similar to the 4.0 ns lifetime determined in (30). The fluorescence decays were fit with a double exponential decay:

$$Y = A_0\left[(1-w)\left(e^{(-x/\tau_1)}\right) + (w)\left(e^{(-x/\tau_2)}\right)\right] + P \quad , \tag{3.1}$$

where A_0 reflects the amplitude of the fluorescence decay, τ_1 describes the lifetime of the entrapped calcein, w describes the fractional contribution of the free calcein, τ_2 is the lifetime of free calcein, which is fixed to 4.073 ns, and P describes the plateau of the decay.

To improve the fitting and account for heterogeneity, the program was modified to include a gamma distribution of lifetimes convolved with an exponential decay as described in Fogarty *et. al.* (32). The benefits of using a gamma distribution, as opposed to a Gaussian distribution, are that it is bounded so that the lifetime cannot be infinite and it simplifies to a simple fitting expression (32). The decays were fit with the general fitting equation derived from (32) for a gamma distribution expressed in terms of the mean and standard deviation of the decay constant distribution:

$$Y = A_0 \left\{ \left[(1-w) \frac{1}{\left(1 + \frac{sd^2 x}{m}\right)^{\frac{m^2}{sd^2}}} \right] + \left[(w) e^{-\frac{x}{\tau}} \right] \right\} + P \quad , \tag{3.2}$$

where A_0 again reflects the amplitude of the fluorescence decay, and m and sd describe the mean and standard deviation of the distribution of decay constants for entrapped calcein, respectively. The second half of the equation remains the same as the second part of equation 3.1, where free calcein is described by a discrete lifetime. Therefore, w and τ describe the fractional contribution and the lifetime of free calcein, respectively. τ is again fixed to 4.073 ns and P is the plateau of the decay.

Since equation 3.2 describes the mean and standard deviation of the gamma distribution of decay constants, the modified code calculates the mean and standard deviation of the corresponding distribution of lifetimes using the relationships given in (32). First, the shape (α)

and scale (κ) parameters of the gamma distribution were calculated from the mean (m_k) and standard deviation (sd_k) of the decay constant distribution:

$$\alpha = \frac{m_k^2}{sd_k^2} - 1 \quad , \tag{3.3}$$

$$\kappa = \frac{sd_k^2}{m_k} \quad . \tag{3.4}$$

From these same shape (α) and scale (κ) parameters, the mean (m_τ) and standard deviation (sd_τ) of the corresponding lifetime distribution can be calculated:

$$m_\tau = \frac{1}{\alpha\kappa} \, , \tag{3.5}$$

$$sd_\tau = \frac{1}{\sqrt{\alpha^2(\alpha - 1)\kappa^2}} \, . \tag{3.6}$$

The negative reciprocal of the mean lifetime and the efflux were then calculated for each decay. The efflux was determined by subtracting the fraction leaked in the absence of permeabilizing agent from the fraction of calcein leaked (w) in the presence of permeabilizing agent. This data was used to construct an efflux vs. lifetime plot with the lifetime plotted on a negative reciprocal scale. As demonstrated by Patel, static quenching of calcein is minimal and was therefore not included in our efflux calculations (30).

In addition, the code was modified to re-fit the data with different initial guesses for fraction leaked if the adjusted chi-square was greater than 2 to encourage the model to find a better fit. The goodness of each fit was evaluated using the reduced χ^2 statistic, Akaike's information criterion (AIC), and Bayesian information criterion (BIC).

3.4 RESULTS

3.4.1 *$PAP_{248-286}$-induced membrane disruption is dependent on membrane charge*

To understand the membrane disruption capabilities of $PAP_{248-286}$, it was incubated with 100 nm lipid vesicles composed of 1:1 POPC:POPG filled with 70 mM calcein. At 70 mM, calcein is self-quenching, and therefore displays low fluorescence. However, addition of $PAP_{248-286}$ releases the contents of these lipid vesicles, resulting in dilution of the calcein, de-quenching, and an increase in the fluorescence signal. $PAP_{248-286}$ has potent membrane permeabilizing activity against 1:1 POPC:POPG liposomes, with approximately 200 nM $PAP_{248-286}$ causing about 50% leakage (Figure 3.2). This corresponds to a 1:100 peptide to lipid (P:L) ratio and is within the range of other known and designed membrane permeabilizing peptides (3, 44). Kinetic traces show an initial burst of fluorescence occurring mostly within the first 5 minutes, followed by a plateau (Figure 3.2a). This behavior is consistent with transient permeabilization, as seen for several other membrane permeabilizing peptides (3). Since it is known that the membrane charge is important to the disruption activities of AMPs and some toxic amyloid oligomers (3, 15, 45), we examined the role of membrane charge in $PAP_{248-286}$'s permeabilization activity. When incubated with POPC liposomes, $PAP_{248-286}$ becomes virtually inactive (Figure 3.2b). This is in agreement with work from the Ramamoorthy group and is likely due to its greatly diminished affinity for neutral liposomes (34, 37).

3.4.2 *Using fluorescence lifetime of calcein-filled liposomes to probe leakage mechanism*

To further delve into the leakage mechanism of $PAP_{248-286}$, we employed the time-resolved fluorescence spectroscopy method developed by the Heerklotz group in 2009 (Figure 3.3a). As described previously, for all-or-none leakage, the lifetime of the entrapped calcein will not change,

since the extent of quenching experienced by calcein inside unleaked liposomes remains the same. For graded leakage, the lifetime of the entrapped calcein increases with leakage, since it experiences less quenching. Thus, the lifetime of the calcein entrapped within the liposomes can be used to directly distinguish between the two mechanisms (30).

To determine the lifetime of the entrapped calcein, the fluorescence decay must be fit with the appropriate equation. Normally the fluorescence decay is fit with a double exponential decay convolved with the instrument response function (IRF): one component describes the lifetime and contribution of the entrapped calcein and the other component describes the lifetime and contribution of the free calcein. However, this model yielded poor fits of the liposomes alone, evidenced by non-random deviations in the residuals and goodness-of-fit metrics (Figure 3.3b and 3.3c). We believe that this could be due to heterogeneity in the liposome preparation (perhaps due to a multilamellar component) or a distribution in the amount of calcein entrapped within the vesicles. In line with this thinking, the fits improve with higher concentrations of permeabilizing agent potentially because the contribution of the entrapped calcein to the decay is diminished (Figure 3.3c and 3.4). To account for this heterogeneity, the discrete lifetime component describing the entrapped calcein was replaced with a gamma distribution of decay constants as described by Fogarty and colleagues (32). Unlike a Gaussian distribution, which is the typical choice in the field, a gamma distribution is bounded by zero so that the lifetime cannot be infinite. A gamma distribution also provides a more robust fit than a Gaussian because it yields a simpler analytical expression when convolved with an exponential. Comparing the fit residuals shows that the use of the gamma distribution is superior to a double-exponential model (Figure 3.3b), and is supported by values of the reduced χ^2 statistic (Figure 3.3c), as well as Akaike (AIC) and Bayesian information criteria (BIC) metrics, which more strongly penalize overfitting (Figure 3.4). All

criteria support the use of the gamma distribution, despite the addition of another fitting parameter to capture the width of the distribution.

3.4.3 *Model selection*

We fit the fluorescence decays of 1:1 POPC:POPG liposomes with $PAP_{248-286}$ using both double exponential (eq. 3.1) and gamma distribution (eq. 3.2) models, and plotted the calculated efflux against the calculated lifetime of the entrapped calcein on a reciprocal scale, as introduced by Patel *et. al*. (30). On this plot, an all-or-none mechanism will yield a vertical line at the lifetime of the entrapped calcein. A homogenously graded mechanism, where the decay constant scales linearly with the efflux, will yield a diagonal line connecting the lifetime of the entrapped calcein and the lifetime of free calcein at 100% leaked. This analysis suggests that, under our experimental conditions, $PAP_{248-286}$ induces graded leakage (Figure 3.7a).

To explore if different models influence the conclusion that is reached, the fluorescence decays were analyzed with both models. A comparison of the fluorescence decays of 1:1 POPC:POPG liposomes with $PAP_{248-286}$ analyzed with both models shows a minor change in the efflux and lifetimes, especially in the low efflux values where the double exponential decay fit is poor. However, the change in the efflux vs. entrapped lifetime plot was so minute that it didn't affect the overall qualitative conclusion of a graded leakage mechanism (Figure 3.6a).

3.4.4 *Leakage mechanism of detergents*

Fluorescence decays were also collected and analyzed with the lifetime distribution (eq. 3.2) analysis for 1:1 POPC:POPG liposomes with SDS and POPC liposomes with CHAPS, as controls for graded and all-or-none leakage mechanisms, respectively (Figure 3.5). As has previously been shown in both GUVs and LUVs, we observe a nearly perfect vertical line on the

efflux vs. lifetime plot for CHAPS with the POPC liposomes corresponding to an all-or-none leakage mechanism (16, 46). As expected for SDS, it displays a graded leakage mechanism (47). Although it doesn't fall on the homogenously graded diagonal line on the efflux vs. lifetime plot, anything below the diagonal graded leakage line is considered to be heterogeneously graded, meaning that there is partial leakage of some vesicles (16, 30). As with $PAP_{248-286}$, fits of decays at low efflux values with the double exponential decay (eq. 3.1) model were poor, even with a different lipid composition and concentration (data not shown). Comparisons between the double exponential decay and gamma distribution model again show small differences in the efflux and lifetime, especially at low concentrations (Figures 3.6b and 3.6c). It is important to note that the reciprocal scale magnifies differences in lifetime on the left-hand side of the efflux vs. lifetime graph. Therefore, while differences in lifetime for low efflux values with SDS seem quite different between the two models, the difference between these mean lifetimes is ~0.07 ns. This analysis suggests that for each of the mechanisms tested, fitting with the more complex model does not dramatically change the qualitative conclusion.

3.4.5 *$PAP_{248-286}$ displays a graded leakage mechanism*

The results of fitting the fluorescence decays of varying concentrations of $PAP_{248-286}$ with 1:1 POPC:POPG lie very near to the homogenously graded leakage line, suggesting a graded leakage mechanism. However, it should be noted that, although both $PAP_{248-286}$ and the graded control detergent SDS display "graded" leakage mechanisms with 1:1 POPC:POPG liposomes, their efflux vs. lifetime plots look very different (Figure 3.5b and 3.7a). The points for $PAP_{248-286}$ lie at or near the homogenously graded leakage line, while the points for SDS are below this line until about 50% efflux. This could mean that leakage events caused by $PAP_{248-286}$ are weaker than those from SDS, as demonstrated by simulations from the Hoernke group (16).

Because $PAP_{248-286}$ causes a small change in efflux over time, we monitored the lifetime at different time points (Figure 3.7b) to see if there is a dependence of leakage mechanism on $PAP_{248-286}$ concentration or an evolution in mechanism with time. For example, some permeabilizing agents like the honeybee toxin melittin display a graded transient mechanism at all concentrations, with additional formation of equilibrium pores at higher concentrations (48). Depending on the timing of these activities and the strength of the pore, measuring the fluorescence decay at different concentrations and times could help elucidate complex mechanisms (Figure 3.8). For example, if a given peptide caused short-lived homogeneous graded leakage followed by all-or-none equilibrium pores then we would expect the early time points on a plot of efflux vs. lifetime to start on the graded leakage diagonal and later time points to deviate vertically from the diagonal. A pore that displayed a graded leakage mechanism would be expected to instead fall on the graded leakage diagonal line across all timepoints. With $PAP_{248-286}$, each of the timepoints falls on or near the homogenously graded leakage line consistent with a graded leakage mechanism across all of the tested concentrations. This data is consistent with the kinetic leakage data from the fluorimeter (Figure 3.2a), showing that most of the leakage occurs within the first 5 minutes following the addition of $PAP_{248-286}$, although there is a small amount of additional leakage between 5 and 30 minutes. Over a two-hour time period we did not observe evidence of equilibrium pore formation, as leakage seemed to plateau by 30 minutes, although it is possible that pore formation occurs on a longer time scale. Putting this lifetime data together with the kinetic data (Figure 3.2a) suggests a transient graded leakage mechanism, similar to other AMPs (3). In this mechanism stochastic, weak leakage events result in small amounts of leakage from all of the vesicles over a short period of time where increasing concentrations of $PAP_{248-286}$ cause more leakage because the number of weak leakage events that occur in each vesicle increase.

3.5 DISCUSSION

Here we have shown that $PAP_{248-286}$ can be a potent membrane disruptor, but this activity is highly dependent on the membrane composition. In addition, we utilized time-resolved fluorescence to show that $PAP_{248-286}$ displays a homogenously graded leakage mechanism. The shape of the kinetic trace along with the leakage evolution by TCSPC further suggest that the bulk of this leakage is due to a transient mechanism dominated by stochastic weak leakage events. In the process of determining this mechanism, we found that conventional fits using two exponential decays did not fully capture the complexity of the decay, leading us to incorporate a gamma distribution following the approach of Fogarty *et. al*. (32). It should be noted that, despite the assumed liposome heterogeneity, the fraction of effluxed dye approaches 100% by both dequenching and lifetime approaches, indicating there is no appreciable population of leakage-resistant vesicles. The gamma distribution is analytically robust and physically better justified than a single lifetime in this context. Although we did not observe a *qualitative* difference in leakage mechanism when comparing our fit results to a simple double exponential decay, there are some differences in the resultant efflux and lifetime values for each of the permeabilizing agents we tested representing different mechanisms. Hoernke and colleagues have developed simulations that aid in *quantitative* interpretation of the data from fluorescence lifetime experiments (16). However, these simulations are dependent on having determinations of efflux and lifetime that are as accurate as possible, and we believe that improving the fit of the model to the data can improve the accuracy and conclusions drawn going forward.

A great strength of fluorescence lifetime analysis is that it is a robust and direct way to differentiate between all-or-none and graded leakage mechanisms. Furthermore, it can interrogate more complex behaviors, such as leakage caused by a combination of multiple mechanisms or

intermediate-strength leakage events. As has been demonstrated previously (16, 46), CHAPS displays an all-or-none leakage mechanism with POPC liposomes, as little change is observed in the entrapped lifetime with increased calcein efflux (Figure 3.5a). Fluorescence lifetime is also able to distinguish between different types of graded leakage. As explained in the results, both SDS and $PAP_{248-286}$ display graded leakage mechanisms (Figures 3.5b and 3.7). However, on the plot of efflux vs. lifetime $PAP_{248-286}$ lies near the homogenously graded line while SDS causes a large deviation from the line where we observe much bigger changes in the fluorescence lifetime of the entrapped calcein for a much smaller amount of dye released. In this case, "homogenously graded" leakage would be caused by weak leakage events across all liposomes, where increasing concentrations of $PAP_{248-286}$ increase the number of leakage events that occur. The behavior observed for SDS has been described as "heterogeneously graded" or "some-or-none" leakage (30, 47). It was further suggested by Hoernke *et. al*. that this type of curve is the result of SDS causing strong but incomplete leakage events in some liposomes (16).

We have also demonstrated that a kinetic component can be added to the study of leakage mechanism by fluorescence lifetime analysis. This is not necessarily as easy with conventional ensemble methods. Although we did not see a change in mechanism and the timed fluorescence analysis with $PAP_{248-286}$ was consistent with a graded leakage mechanism across a range of concentrations, this may not always be the case. For example, it has been demonstrated that other membrane permeabilizing peptides including the melittin and islet amyloid polypeptide (IAPP) display different leakage mechanisms at different concentrations of peptide (19, 48). Therefore, if the leakage is slow enough, measuring lifetimes at different timepoints can help to dissect complex leakage mechanisms.

The results we have presented here, along with previous work describing the superficial interactions of $PAP_{248-286}$ with lipid membranes driven by electrostatics suggests that the binding of $PAP_{248-286}$ to membranes causes transient, graded leakage. Although this type of mechanism has been proposed for other membrane permeabilizing peptides (15, 21, 22, 49, 50), very little is known about how it physically occurs. Speculatively, this binding would lead to a mass imbalance of $PAP_{248-286}$ across the bilayer. This asymmetry could potentially be relieved by $PAP_{248-286}$ translocating across the membrane or a structural rearrangement in the membrane accompanied by a small amount of leakage. However, once translocation of $PAP_{248-286}$ or structural rearrangement of the membrane occurs and membrane asymmetry is no longer a driving force, and leakage ceases. This explanation has been proposed for other membrane permeabilizing peptides (21, 22, 50). Our assay suggests that $PAP_{248-286}$ is quite potent, with a peptide:lipid ratio of 1:100 causing about 50% leakage of LUVs, well within the 1:1 – 1:10,000 regime of other known membrane permeabilizing peptides (3). However, against a panel of bacteria, $PAP_{248-286}$ did not display any direct antimicrobial activity (38). While this could be due to a difference in membrane composition, as the system used here is extremely simplified, it may also highlight the importance of understanding leakage mechanism. In addition to differences in membrane complexity and composition, there is also a vast difference in the membrane size of the two systems. The same molecular mechanism of leakage can result in very different behavior depending on the size (or, more specifically, the ratio of volume to surface area) of a model membrane or target cell. For example, an agent like $PAP_{248-286}$ that displays a homogenously graded leakage mechanism in LUVs produces numerous, weak leakage events. However, in a bigger target compartment with a larger surface area and larger total volume, like a bacterial cell with a diameter that is at least 10x larger than an LUV, although the efflux increases due to the larger surface area, the strength of each leakage event relative to the

volume would be diminished. This is because the ratio of volume to surface area is larger in the larger bacterial cell than an LUV. Therefore, while $PAP_{248-286}$ might cause weak leakage in LUVs, the diminished effect in bacteria might not be enough to result in cell death. This size dependence has been discussed at length in Braun *et. al.* (16) and is consistent with previous observations that the all-or-none LUV-permeabilizing lipopeptide fengycin is fungicidal, while surfactin, the seemingly more potent graded LUV-permeabilizing surfactant, is less biologically active (31). Therefore, a mechanism that is determined to be graded in the context of LUVs may be an indicator that the candidate membrane permeabilizer might not be as useful in a biological setting.

3.6 FIGURES

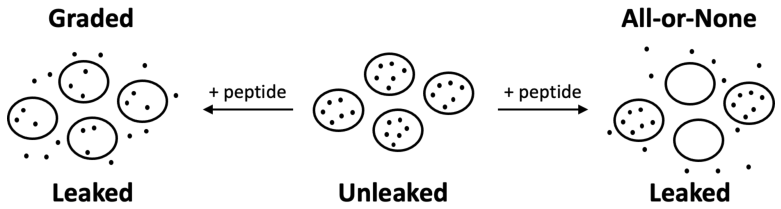

Figure 3.1: Schematic comparing 50% leakage for all-or-none and graded leakage mechanisms.

The cartoon depicts the two different leakage mechanisms. The center of the cartoon shows unleaked liposomes. Upon addition of a membrane permeabilizing peptide that induces liposome leakage, the left side shows a graded leakage mechanism where 50% of the contents from inside each of the liposomes leak out into solution, while the right side shows an all-or-none leakage mechanism where 100% of the contents leaks from 50% of liposomes while the other 50% of liposomes remain intact.

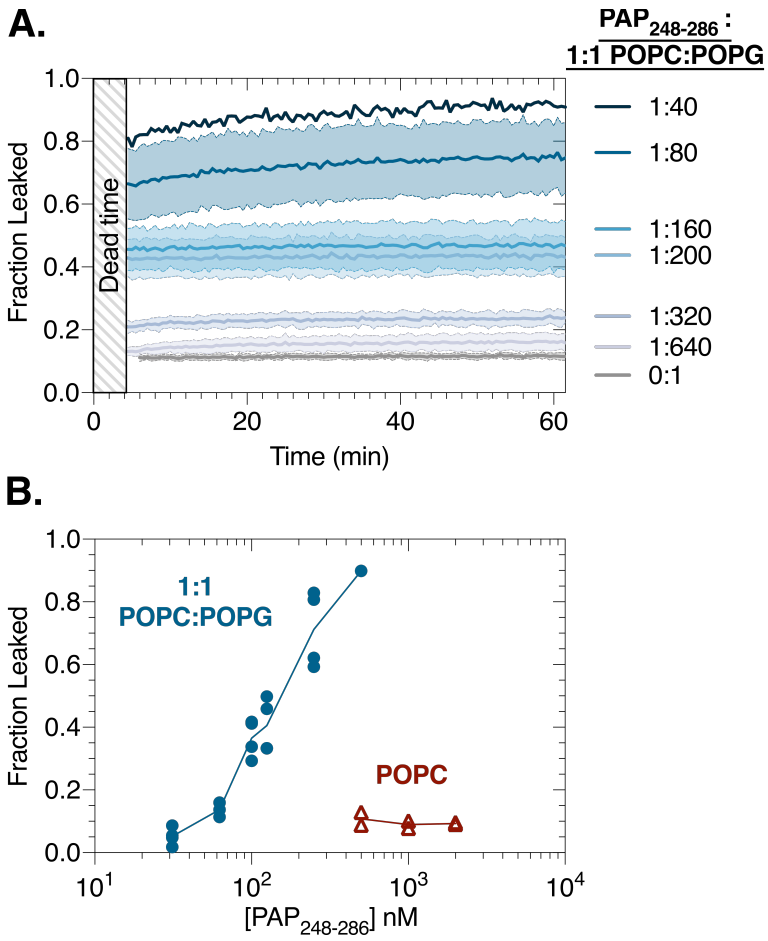

Figure 3.2: $PAP_{248-286}$ disruption of lipid membranes is dependent on lipid headgroup charge.

(A) Calcein fluorescence de-quenching showing the leakage kinetics of 20 μM calcein-filled 1:1 POPC:POPG liposomes with 0 nM to 500 nM $PAP_{248-286}$ (*light blue to dark blue*). The dead time of the measurement is marked as a striped box in the graph. Bars represent the mean and standard deviation of four independent experiments conducted on different days. This data shows that, over the course of an hour, the bulk of the leakage occurs within the dead time of the experiment and the signal shows little to no subsequent change. (B) Fraction of calcein leaked after an hour incubation of $PAP_{248-286}$ with 20 μM calcein-filled 1:1 POPC:POPG liposomes (blue circles) or 20 μM calcein-filled POPC liposomes (red triangles). Each point represents an independent experiment and lines connect the means. This indicates that $PAP_{248-286}$-induced membrane disruption is highly dependent on the membrane charge.

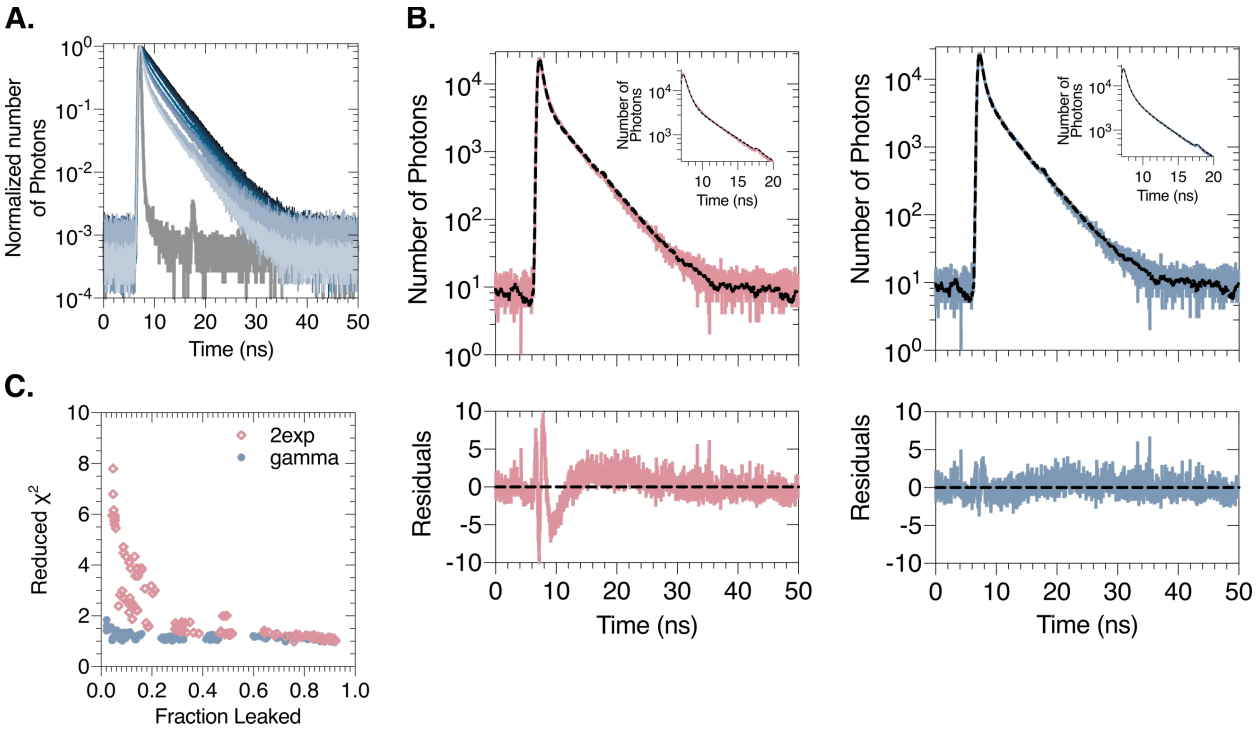

Figure 3.3: Re-convolution of a gamma distribution with an exponential decay improves fitting of complex fluorescence decays.

(A) Representative normalized fluorescence decays measured an hour after mixing 20 μM calcein-filled 1:1 POPC:POPG liposomes with 0-500 nM $PAP_{248-286}$ (*light blue* to *dark blue*). The gray trace is the measured instrumental response function (IRF). Curves show 3 technical replicates and are representative of 4 independent experiments conducted on different days. (B) Representative fluorescence decay of 20 μM calcein-filled 1:1 POPC:POPG liposomes in the absence of any $PAP_{248-286}$ (top) fit with a double exponential decay (left, pink) and a convolution of an exponential decay with a gamma distribution (right, *blue*). The dashed black line on each curve represents the fit for each model. The residuals of the fit are plotted below each graph and the inset in the corner of each graph is a magnification to highlight the area that the double exponential decay model struggles to capture. (C) Plot of the reduced χ^2 as a function of the calculated fraction of calcein leaked for the double exponential decay (2exp; *open pink diamonds*) and gamma distribution (gamma; *blue circles*) fits of all 4 independent data sets.

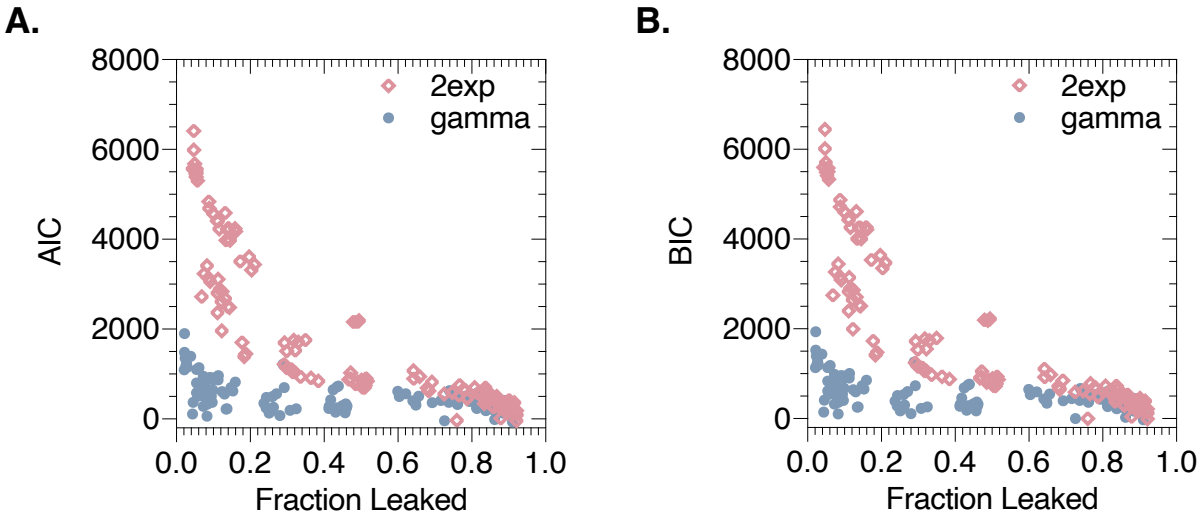

Figure 3.4: AIC and BIC both agree that gamma distribution convolved with an exponential decay model fits complex fluorescence decays better than a double exponential decay model.

Plots of calculated AIC (A) and BIC (B) values as a function of the fraction of calcein leaked at various concentrations of $PAP_{248-286}$ for the double exponential decay (2exp; *open pink diamonds*) and gamma distribution (*blue circles*) fits of the 4 independent data sets described in Figure 3.3.

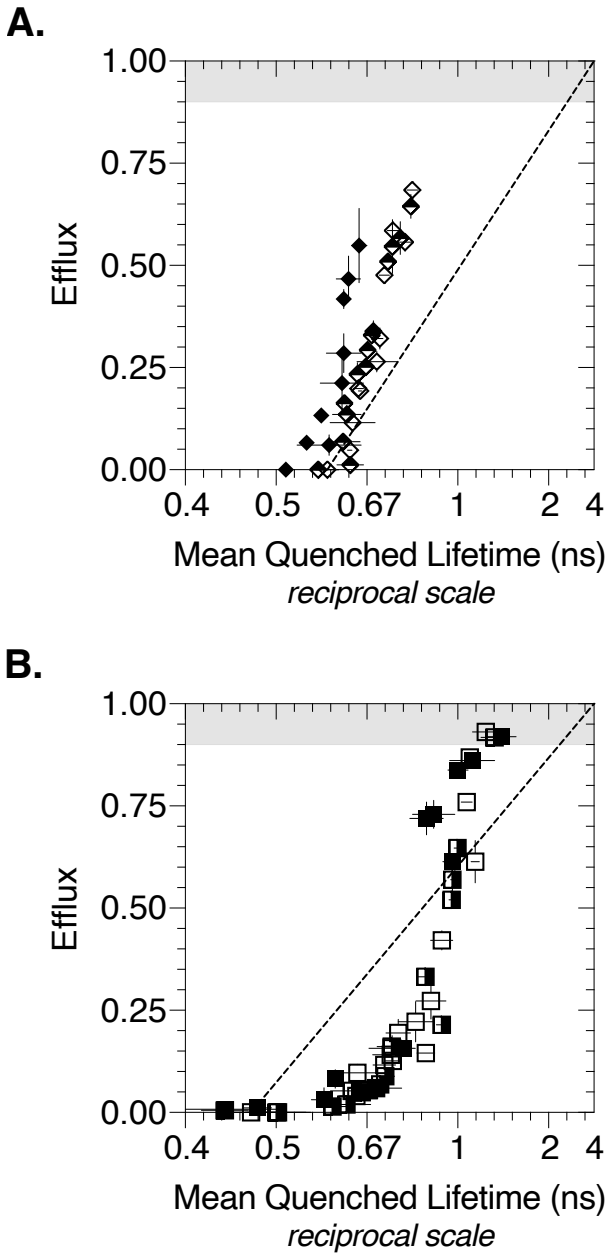

Figure 3.5: TCSPC can distinguish between an all-or-none and graded leakage mechanism.

Plots of the calcein efflux vs. mean quenched lifetime (on a reciprocal scale) calculated after fitting the fluorescence lifetime decays of 300 μM calcein-filled POPC liposomes incubated for 1 hour with 0-0.13% (w/v) CHAPS (A) or of 20 μM calcein-filled 1:1 POPC:POPG liposomes incubated for half an hour with 0-0.04% (w/v) SDS (B) with the gamma distribution model. The shading of the diamonds (A) or squares (B) distinguishes results from three independent experiments. The diagonal dashed line in each graph shows the expected efflux vs. lifetime for a homogenous graded leakage mechanism and the shaded area at an efflux greater than 0.9 represents data for which the fitting becomes unreliable. The bars on each point represents the mean and standard deviation of 5 replicate measurements.

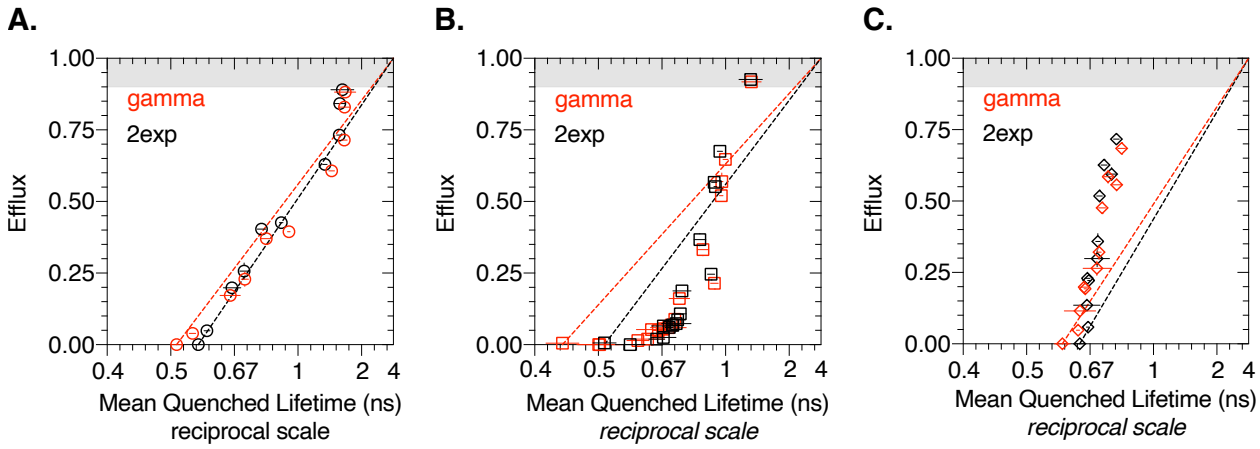

Figure 3.6: Model selection does not dramatically affect qualitative conclusion.

Plots of the calcein efflux vs. mean quenched lifetime (on a reciprocal scale) calculated for 20 μM calcein-filled 1:1 POPC:POPG liposomes incubated with 0-500 nM $PAP_{248-286}$ (A) or 0-0.04% SDS (B) and 300 μM calcein-filled POPC liposomes incubated with 0-0.13% CHAPS (C) calculated with the gamma distribution (*red*) or double exponential decay (2exp; *black*) models. Black and red diagonal lines correspond to a homogenous graded leakage mechanism for the double exponential decay and gamma distribution fits, respectively. Experimental data from a single day was used for clarity and is representative of 3 independent experiments. Bars represent the mean and standard deviation of 3-5 replicate measurements.

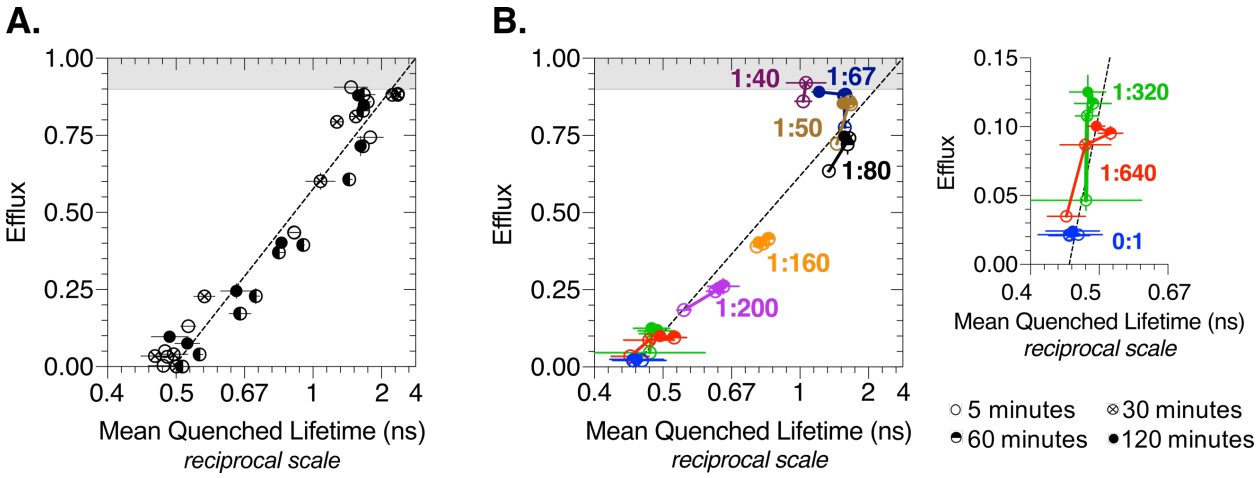

Figure 3.7: $PAP_{248-286}$ displays a graded leakage mechanism.

(A) Plot of the calcein efflux vs. mean quenched lifetime (on a reciprocal scale) obtained from fitting the fluorescence lifetime decays of 0-500 nM $PAP_{248-286}$ incubated for 1 hour with 20 μM calcein-filled 1:1 POPC:POPG liposomes with the gamma distribution model. The shading of the circles distinguishes four independent experiments, and the error bars represent the mean and standard deviation of 3-5 replicate measurements. (B) Plot of the calcein efflux vs. mean quenched lifetime (reciprocal scale) over time to show evolution of leakage mechanism. Fluorescence lifetime decays of 20 μM calcein-filled 1:1 POPC:POPG liposomes incubated with 0-500 nM $PAP_{248-286}$ were measured after a 5 (*open circle*), 30 (*circle with cross*), 60 (*half-filled circle*), and 120-minute (*filled circle*) incubation. Lines connect the points in chronological order. Data are representative of 3 independent experiments, and error bars represent the mean and standard deviation of 3-5 replicate measurements. The panel to the right is a magnification to clarify changes occurring at low efflux values. The diagonal dashed line in each graph shows the expected efflux vs. lifetime for a homogenous graded leakage mechanism and the shaded area at an efflux greater than 0.9 represents data for which the fitting becomes unreliable.

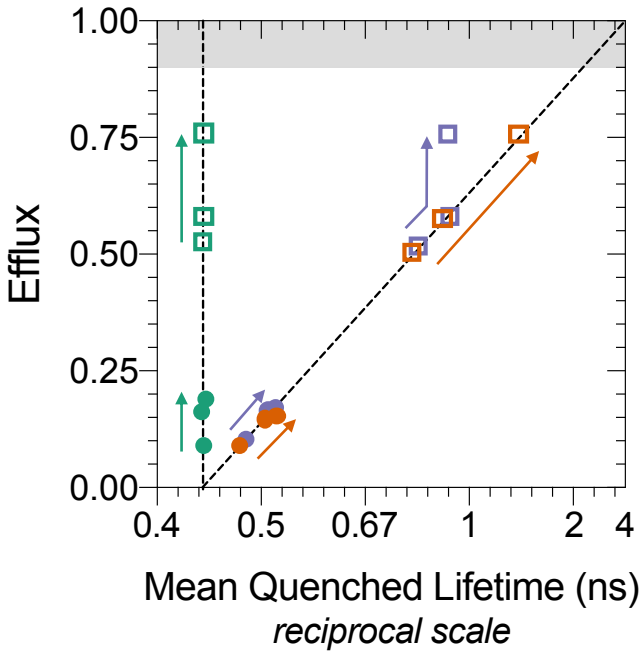

Figure 3.8: Illustration on how different hypothetical two-phase mechanisms might look in a timed fluorescence lifetime experiment on the efflux vs. lifetime plot.

Each of these two-phased mechanisms displays a transient phase at a low peptide concentration (filled circles) and additionally form equilibrium pores at a higher peptide concentration (empty squares). Arrows point in the direction of increasing time, with hypothetical time points marking an early time in the transient phase, one after the transient phase, and one at equilibrium. Examples here include an all-or-none transient phase and equilibrium pore (green), a graded transient phase with an all-or-none equilibrium pore (purple), or a graded transient phase and equilibrium pore (orange).

3.7 REFERENCES

1. Zasloff, M. 2002. Antimicrobial Peptides of Multicellular Organisms. *Nature*. 415:389–395.
2. Nguyen, L.T., E.F. Haney, and H.J. Vogel. 2011. The expanding scope of antimicrobial peptide structures and their modes of action. *Trends Biotechnol.* 29:464–472.
3. Guha, S., J. Ghimire, E. Wu, and W.C. Wimley. 2019. Mechanistic Landscape of Membrane-Permeabilizing Peptides. *Chem. Rev.* 119:6040–6085.
4. Wang, G. 2014. Human antimicrobial peptides and proteins. *Pharmaceuticals*. 7:545–594.
5. Lázár, V., A. Martins, R. Spohn, L. Daruka, G. Grézal, G. Fekete, M. Számel, P.K. Jangir, B. Kintses, B. Csörgo, Á. Nyerges, Á. Györkei, A. Kincses, A. Dér, F.R. Walter, M.A. Deli, E. Urbán, Z. Hegedus, G. Olajos, O. Méhi, B. Bálint, I. Nagy, T.A. Martinek, B. Papp, and C. Pál. 2018. Antibiotic-resistant bacteria show widespread collateral sensitivity to antimicrobial peptides. *Nat. Microbiol.* 3:718–731.
6. Lazzaro, B.P., M. Zasloff, and J. Rolff. 2020. Antimicrobial peptides: Application informed by evolution. *Science (80-.).* 368.
7. Bahar, A.A., and D. Ren. 2013. Antimicrobial peptides. *Pharmaceuticals*. 6:1543–1575.
8. Bucciantini, M., E. Giannoni, F. Chiti, F. Baroni, L. Formigli, J. Zurdo, N. Taddei, G. Ramponi, C.M. Dobson, and M. Stefani. 2002. Inherent toxicity of aggregates implies a common mechanism for protein misfolding diseases. *Nature*. 416:507–511.
9. Kayed, R., E. Head, J.L. Thompson, T.M. McIntire, S.C. Milton, C.W. Cotman, and C.G. Glabel. 2003. Common structure of soluble amyloid oligomers implies common mechanism of pathogenesis. *Science (80-.).* 300:486–489.
10. Caughey, B., and P.T. Lansbury. 2003. Protofibrils , Pores, Fibrils, and Neurodegeneration: Separating the Responsible Protein Aggregates from The Innocent Bystanders. *Annu. Rev. Neurosci.* 26:267–298.
11. Ke, P.C., R. Zhou, L.C. Serpell, R. Riek, T.P.J. Knowles, H.A. Lashuel, E. Gazit, I.W. Hamley, T.P. Davis, M. Fändrich, D.E. Otzen, M.R. Chapman, C.M. Dobson, D.S. Eisenberg, and R. Mezzenga. 2020. Half a century of amyloids: Past, present and future. *Chem. Soc. Rev.* 49:5473–5509.
12. Hebda, J. a, and A.D. Miranker. 2009. The interplay of catalysis and toxicity by amyloid intermediates on lipid bilayers: insights from type II diabetes. *Annu. Rev. Biophys.* 38:125–52.
13. Cascella, R., M. Perni, S.W. Chen, G. Fusco, C. Cecchi, M. Vendruscolo, F. Chiti, C.M. Dobson, and A. De Simone. 2019. Probing the Origin of the Toxicity of Oligomeric Aggregates of α-Synuclein with Antibodies. *ACS Chem. Biol.* 14:1352–1362.
14. Weinstein, J.N., R.D. Klausner, T. Innerarity, E. Ralston, and R. Blumenthal. 1981. Phase transition release, a new approach to the interaction of proteins with lipid vesicles Application to lipoproteins. *BBA - Biomembr.* 647:270–284.
15. Almeida, P.F., and A. Pokorny. 2012. Interactions of antimicrobial peptides with lipid bilayers. .
16. Braun, S., Š. Pokorná, R. Šachl, M. Hof, H. Heerklotz, and M. Hoernke. 2018. Biomembrane Permeabilization: Statistics of Individual Leakage Events Harmonize the Interpretation of Vesicle Leakage. *ACS Nano*. 12:813–819.
17. Apellániz, B., J.L. Nieva, P. Schwille, and A.J. García-Sáez. 2010. All-or-none versus graded: Single-vesicle analysis reveals lipid composition effects on membrane permeabilization. *Biophys. J.* 99:3619–3628.

18. Paterson, D.J., M. Tassieri, J. Reboud, R. Wilson, and J.M. Cooper. 2017. Lipid topology and electrostatic interactions underpin lytic activity of linear cationic antimicrobial peptides in membranes. *Proc. Natl. Acad. Sci. U. S. A.* 114:E8324–E8332.

19. Last, N.B., E. Rhoades, and A.D. Miranker. 2011. Islet amyloid polypeptide demonstrates a persistent capacity to disrupt membrane integrity. *Proc Natl Acad Sci U S A*. 108:9460–9465.

20. Wheaten, S.A., A. Lakshmanan, and P.F. Almeida. 2013. Statistical analysis of peptide-induced graded and all-or-none fluxes in giant vesicles. *Biophys. J.* 105:432–443.

21. Yandek, L.E., A. Pokorny, A. Florén, K. Knoelke, Ü. Langel, and P.F.F. Almeida. 2007. Mechanism of the cell-penetrating peptide transportan 10 permeation of lipid bilayers. *Biophys. J.* 92:2434–2444.

22. Yandek, L.E., A. Pokorny, and P.F.F. Almeida. 2009. Wasp mastoparans follow the same mechanism as the cell-penetrating peptide transportan 10. *Biochemistry*. 48:7342–7351.

23. Schwarz, G., and C.H. Robert. 1992. Kinetics of pore-mediated release of marker molecules from liposomes or cells. *Biophys. Chem.* 42:291–296.

24. Parente, R.A., S. Nir, and F.C. Szoka. 1990. Mechanism of Leakage of Phospholipid Vesicle Contents Induced by the Peptide GALA. *Biochemistry*. 29:8720–8728.

25. Ostolaza, H., B. Bartolomé, I.O. de Zárate, F. de la Cruz, and F.M. Goñi. 1993. Release of lipid vesicle contents by the bacterial protein toxin α-haemolysin. *BBA - Biomembr.* 1147:81–88.

26. Wimley, W.C., M.E. Selsted, and S.H. White. 1994. Interactions between human defensins and lipid bilayers: Evidence for formation of multimeric pores. *Protein Sci.* 3:1362–1373.

27. Ladokhin, A.S., W.C. Wimley, and S.H. White. 1995. Leakage of membrane vesicle contents: determination of mechanism using fluorescence requenching. *Biophys. J.* 69:1964–71.

28. Ladokhin, A.S., W.C. Wimley, K. Hristova, and S.H. White. 1997. Mechanism of leakage of contents of membrane vesicles determined by fluorescence requenching. *Methods Enzymol.* 278:474–486.

29. Tamba, Y., and M. Yamazaki. 2005. Single giant unilamellar vesicle method reveals effect of antimicrobial peptide magainin 2 on membrane permeability. *Biochemistry*. 44:15823–15833.

30. Patel, H., C. Tscheka, and H. Heerklotz. 2009. Characterizing vesicle leakage by fluorescence lifetime measurements. *Soft Matter*. 5:2849.

31. Patel, H., C. Tscheka, K. Edwards, G. Karlsson, and H. Heerklotz. 2011. All-or-none membrane permeabilization by fengycin-type lipopeptides from Bacillus subtilis QST713. *Biochim. Biophys. Acta - Biomembr.* 1808:2000–2008.

32. Fogarty, A.C., A.C. Jones, and P.J. Camp. 2011. Extraction of lifetime distributions from fluorescence decays with application to DNA-base analogues. *Phys. Chem. Chem. Phys.* 13:3819–3830.

33. Münch, J., E. Rücker, L. Ständker, K. Adermann, C. Goffinet, M. Schindler, S. Wildum, R. Chinnadurai, D. Rajan, A. Specht, G. Giménez-Gallego, P.C. Sánchez, D.M. Fowler, A. Koulov, J.W. Kelly, W. Mothes, J.C. Grivel, L. Margolis, O.T. Keppler, W.G. Forssmann, and F. Kirchhoff. 2007. Semen-Derived Amyloid Fibrils Drastically Enhance HIV Infection. *Cell*. 131:1059–1071.

34. Brender, J.R., K. Hartman, L.M. Gottler, M.E. Cavitt, D.W. Youngstrom, and A. Ramamoorthy. 2009. Helical conformation of the SEVI precursor peptide PAP248-286, a dramatic enhancer of HIV infectivity, promotes lipid aggregation and fusion. *Biophys. J.* 97:2474–2483.

35. Nanga, R.P.R., J.R. Brender, S. Vivekanandan, N. Popovych, and A. Ramamoorthy. 2009. NMR structure in a membrane environment reveals putative amyloidogenic regions of the SEVI precursor peptide PAP248-286. *J. Am. Chem. Soc.* 131:17972–17979.

36. Brender, J.R., R.P.R. Nanga, N. Popovych, R. Soong, P.M. Macdonald, and A. Ramamoorthy. 2011. The amyloidogenic SEVI precursor, PAP248-286, is highly unfolded in solution despite an underlying helical tendency. *Biochim. Biophys. Acta - Biomembr.* 1808:1161–1169.

37. Vane, E.W., S. He, L. Maibaum, and A. Nath. 2020. Rapid Formation of Peptide/Lipid Coaggregates by the Amyloidogenic Seminal Peptide PAP248-286. *Biophys. J.* 119:924–938.

38. Easterhoff, D., F. Ontiveros, L.R. Brooks, Y. Kim, B. Ross, J.N. Silva, J.S. Olsen, C. Feng, D.J. Hardy, P.M. Dunman, and S. Dewhurst. 2013. Semen-derived enhancer of viral infection (SEVI) binds bacteria, enhances bacterial phagocytosis by macrophages, and can protect against vaginal infection by a sexually transmitted bacterial pathogen. *Antimicrob. Agents Chemother.* 57:2443–2450.

39. Chen, P.S., T.Y. Toribara, and H. Warner. 1956. Microdetermination of Phosphorus. *Anal. Chem.* 28:1756–1758.

40. Chifflet, S., A. Torriglia, R. Chiesa, and S. Tolosa. 1988. A method for the determination of inorganic phosphate in the presence of labile organic phosphate and high concentrations of protein: Application to lens ATPases. *Anal. Biochem.* 168:1–4.

41. Fiske, C.H., and Y. Subbarow. 1925. The Colorimetric Determination of Phosphorus. *J. Biol. Chem.* 66:374–389.

42. Scott, H.L., A. Skinkle, E.G. Kelley, M.N. Waxham, I. Levental, and F.A. Heberle. 2019. On the Mechanism of Bilayer Separation by Extrusion, or Why Your LUVs Are Not Really Unilamellar. *Biophys. J.* 117:1381–1386.

43. Petschke, D. 2019. dpscience/DLTReconvolution: DLTReconvolution v1.2. .

44. Wimley, W.C. 2010. Describing the mechanism of antimicrobial peptide action with the interfacial activity model. *ACS Chem. Biol.* 5:905–917.

45. Andreasen, M., N. Lorenzen, and D. Otzen. 2015. Interactions between misfolded protein oligomers and membranes: A central topic in neurodegenerative diseases? *Biochim. Biophys. Acta - Biomembr.* 1848:1897–1907.

46. Patel, H., Q. Huynh, D. Bärlehner, and H. Heerklotz. 2014. Additive and synergistic membrane permeabilization by antimicrobial (LIPO)peptides and detergents. *Biophys. J.* 106:2115–2125.

47. Hovakeemian, S.G., R. Liu, S.H. Gellman, and H. Heerklotz. 2015. Correlating antimicrobial activity and model membrane leakage induced by nylon-3 polymers and detergents. *Soft Matter*. 11:6840–6851.

48. Krauson, A.J., J. He, and W.C. Wimley. 2012. Determining the mechanism of membrane permeabilizing peptides: Identification of potent, equilibrium pore-formers. *Biochim. Biophys. Acta - Biomembr.* 1818:1625–1632.

49. Rex, S., and G. Schwarz. 1998. Quantitative studies on the melittin-induced leakage mechanism of lipid vesicles. *Biochemistry*. 37:2336–2345.

50. Pokorny, A., and P.F.F. Almeida. 2004. Kinetics of dye efflux and lipid flip-flop induced by δ-lysin in phosphatidylcholine vesicles and the mechanism of graded release by amphipathic, α-helical peptides. *Biochemistry*. 43:8846–8857.

Chapter 4. OPEN QUESTIONS

4.1 INTRODUCTION

While previous chapters have explored many aspects of $PAP_{248-286}$-lipid membrane interactions, many questions still remain. The goal of this chapter is to provide additional characterizations of the self-assembly and membrane interactions of $PAP_{248-286}$ as well as give experimental insights that will hopefully be of use to future researchers who may build on this project. This chapter focuses on work that attempts to improve understanding of the oligomeric state of $PAP_{248-286}$ in solution, $PAP_{248-286}$'s membrane binding cooperativity, the effect of the oligomeric state and SEVI amyloid on its ability to disrupt membranes, and the antimicrobial activity of $PAP_{248-286}$. Some of these questions, like the oligomeric state of $PAP_{248-286}$ in solution, requires an additional experiment as elucidated below, while others, like the effect of SEVI amyloid formation on membrane disruption or the antimicrobial activities could be the basis for a totally new project. In particular, I believe that the observation of anti-biofilm activity by $PAP_{248-286}$ opens up many new questions and interesting and exciting new areas of study.

4.2 RESULTS AND DISCUSSION

4.2.1 *Oligomeric state of $PAP_{248-286}$ in solution*

A common problem with intrinsically disordered peptides and amyloid-forming proteins that are prone to aggregate, is that the peptides will form oligomers and aggregates in solution. Treatment of peptides with fluorinated alcohols like HFIP is one common method that has been utilized to break up pre-formed aggregates into monomers. Other groups have used this method

for the preparation of $PAP_{248-286}$ (1, 2). However, HFIP treatment is not without its drawbacks, as the presence of residual HFIP has been shown to affect the lipid membrane integrity (3, 4) as well as amyloid formation (5, 6). Other methods to remove aggregates include centrifuging the peptide solution at high speeds and filtering the peptide solution. Autocorrelation curves from DLS measurements suggest the presence of large aggregated species in a solution of 1 mg/mL $PAP_{248-286}$ (Figure 4.1a). Interestingly, treatment with HFIP did not seem to have a large effect on the presence of the aggregate. Filtering the peptide with a 0.22 μm syringe filter eliminated most of the aggregated species, but some of the oligomeric species seemed to remain in solution. Based on this data, it seems that the most effective way to remove the large species was by centrifuging the solutions at 21100*g* at 4°C for 30 minutes (Figure 4.1a).

SEC-MALS was then employed to determine the oligomeric state of $PAP_{248-286}$ in solution. While the molecular weight of $PAP_{248-286}$ is 4.6 kDa, SEC-MALS shows a molecular weight (MW) of 8.4 ± 0.1 kDa (Figure 4.1b). This is ~1.8x bigger than monomeric $PAP_{248-286}$, suggesting that $PAP_{248-286}$ may exist as a dimer in solution. However, it should be noted that the SEC column used for this experiment has a MW range of 5-1,250 kDa. Therefore, $PAP_{248-286}$ monomer is slightly too small to be resolved and came off the column very close to the buffer peak, making it hard to obtain a reliable MW. Overall, these results suggest that $PAP_{248-286}$ forms large aggregates that can be removed by spinning and that the remaining $PAP_{248-286}$ in solution is either a monomer or dimer. To verify if $PAP_{248-286}$ is dimeric in solution or not, it should be a run on a column with smaller pores that does not interact with intrinsically disordered peptides.

4.2.2 *$PAP_{248-286}$ binding cooperativity*

Excess unlabeled $PAP_{248-286}$ was added to fluorescently-labeled $PAP_{248-286}$ in FCS lipid binding experiments to prevent instability in measurements due to non-specific binding of the

intrinsically disordered peptide to the coverslip. To assess whether or not the excess $PAP_{248-286}$ affects the binding affinity, liposome binding experiments were performed in the presence of varying concentrations of unlabeled $PAP_{248-286}$. Figure 4.2 shows the binding curves and the corresponding binding affinities calculated from a one-site binding model from titrations of POPG and 1:1 POPC:POPG liposomes in the presence of 2, 5, and 10 μM unlabeled $PAP_{248-286}$. For both POPG and 1:1 POPC:POPG liposomes, increasing the concentration of unlabeled $PAP_{248-286}$ from 2 to 10 μM decreases the binding affinity ~6.5-fold and ~3.4-fold, respectively. A small decrease in the binding affinity in the presence of increased concentrations of peptide suggests modest negative cooperativity. Although the binding curves are quite noisy and the fits to a simple 1:1 binding model are not perfect, the differences in the fraction of peptide bound at each lipid concentration make it clear that binding affinity decreases with increasing peptide concentration. Negative cooperativity is a bit unexpected considering that some other amyloid-forming peptides, like IAPP, display positive cooperativity when binding to lipid membranes, due to favorable peptide-peptide interactions on the membrane (7). Relatedly, positive cooperativity is often invoked to explain the non-linear dependence of membrane disruption on AMP or amyloid-forming peptide concentration and is thought to be important to their antimicrobial mechanism (8, 9). The observed cooperativity in membrane disruption could either be due to cooperative binding or cooperativity in forming a lytic species (10, 11). However, if we consider that electrostatics drive the binding of $PAP_{248-286}$ to lipid membranes, then the binding of highly cationic $PAP_{248-286}$ to the membranes would neutralize some of these charges, resulting in a weaker binding affinity for the next peptide (12). Therefore, successive binding events would not be independent.

4.2.3 *SEVI fibril-induced membrane disruption*

It has been shown for many amyloid-forming peptides that pre-amyloid oligomers display cytotoxicity and cell lysis (13, 14). Further, in some cases the amyloid form of peptide does not display these activities and is thought to be inert (15). Therefore, I investigated whether $PAP_{248-286}$ displays a similar dependence of membrane-disrupting activity on its oligomeric state. To do this, different timepoints during the SEVI fibril formation reaction were added to the liposome leakage assay. Surprisingly, Figure 4.3 shows that the oligomeric state of $PAP_{248-286}$ ($PAP_{248-286}$ monomer or SEVI fibril) does not consistently affect the leakage kinetics or the fraction leaked after two hours. If an effect is observed, it is very minor. Even timepoints collected during the elongation phase of the sigmoidal fibril formation curve, which should contain primarily oligomers, do not affect the kinetics or fraction leaked (Figure 4.3b).

There could be many explanations for this unexpected lack of observed difference between distinct oligomeric states of $PAP_{248-286}$. First, it is possible that very little of the $PAP_{248-286}$ monomer was incorporated into the fibrils. However, concentration calculations of $PAP_{248-286}$ monomer left in solution after spinning down SEVI fibrils showed that only 15-20% of the $PAP_{248-286}$ monomer remains in solution (data not shown). This small amount of $PAP_{248-286}$ monomer is not expected to cause liposome leakage, especially not to the extent that is observed, making this explanation unlikely. Another possibility is that 2 hours is not long enough to capture differences in fraction leaked. It could be that monomeric or oligomeric $PAP_{248-286}$ undergo longer structural rearrangements on the membranes that result in pore formation while the amyloid fibrils are unable to undergo this rearrangement. Another possibility is that diluting the fibrils down to 2 μM causes them to disassemble, as the low concentration may mean that the amyloid state is no longer the most thermodynamically stable state of the peptide (16). Previous experience with SEVI fibrils

showed that diluting fibrils from a PBS buffer into a HEPES buffer resulted in a decrease in ThT fluorescence. This decrease is presumably from a dissociation of amyloid fibrils, although there is the unlikely possibility that the fibers remain, but with a different morphology that does not fluoresce in the presence of ThT (17, 18). Fibrils diluted to 2 μM in PBS still displayed ThT fluorescence, suggesting that fibrils remain intact (data not shown). However, this measurement was taken at a single timepoint after dilution and it remains possible (depending on the off rate of the monomer) that, over time, shaking or the presence of lipid vesicles results in the dissociation of less thermodynamically favorable fibrils.

It is of course possible that amyloid fibrils have the same capacity to disrupt membranes as the $PAP_{248-286}$ monomer. This could mean that over the course of the leakage experiment $PAP_{248-286}$ forms amyloid fibrils. However, given the very stringent requirements for SEVI amyloid formation discussed in 2.4.3 and the low concentrations used in these experiments, this seems less likely. It could also mean that either the fibrils are able to utilize different mechanisms to disrupt membranes to the same extent as $PAP_{248-286}$ monomer or they utilize the same mechanisms. Under these experimental conditions, a $PAP_{248-286}$:lipid ratio of 1:10 is required to cause 50% liposome leakage. This is very high and could indicate that the observed membrane disruption is due to an artifact like liposome aggregation and fusion (19). More work is needed to try to parse out whether the fibrils remain stable or if vesicle aggregation could be responsible for the perceived activity.

One note of caution for comparing these results to the kinetic leakage in Chapter 3: This experiment was carried out on a Biotek plate reader due to its improved throughput. However, experience with these plate reader kinetic assays has shown that, while the trends remain the same, the results are less reproducible than in a quartz cuvette in a fluorimeter probably due to instability of the liposomes in the plates. Therefore, day to day variability makes it difficult to quantitatively

compare one day's experiments to another. This drawback should be weighed against the plate reader's greater throughput compared to the fluorimeter.

4.2.4 *Antimicrobial activity of $PAP_{248-286}$*

As described in section 1.3, the overlap in not only physicochemical properties but also in functional activities of amyloid-forming peptides and AMPs has just recently begun to be appreciated (20). Easterhoff *et. al.* demonstrated that SEVI fibrils displayed antimicrobial activity, not by directly killing bacteria, but by causing agglutination and increasing bacterial uptake into macrophages. Importantly, they found that monomeric $PAP_{248-286}$ does not display any antimicrobial activity (21). In agreement with this work, table 4.1 shows that even at very high, non-physiological concentrations, $PAP_{248-286}$ still does not display direct antimicrobial against any of the gram positive (*E. faecalis* and *S. aureus*) nor gram negative (*E. coli*) organisms as assessed by MIC.

Another mechanism that antimicrobial amyloid-forming peptides like Aβ can use is by preventing the adhesion of bacteria to their target cells (22). Established AMPs are also known to disrupt bacterial biofilm formation (23, 24). A microtiter plate (MtP) biofilm assay was used to assess the effect of $PAP_{248-286}$ on the biofilm formation of two bacteria, *E. faecalis* (S613) and *S. aureus* (SH1000). Interestingly, $PAP_{248-286}$ inhibits biofilm formation of *E. faecalis* at below physiological concentrations but does not affect *S. aureus* biofilm (Figure 4.4a). It should be noted that low concentrations of $PAP_{248-286}$ appear to increase *S. aureus* biofilm while high, non-physiological concentrations of $PAP_{248-286}$ are required to see any inhibitory activity.

Daptomycin is an FDA approved drug that is thought to kill bacteria through a membrane disruption mechanism (25, 26). Bacteria that become resistant to daptomycin often develop cross-resistance to cationic AMPs as well (27). The anti-biofilm activity of $PAP_{248-286}$ against clinically

isolated *E. faecalis* strains that are susceptible (S613) and resistant (R712) to daptomycin was also assessed using the MtP biofilm assay. These results suggest that $PAP_{248-286}$ is only slightly less active against the daptomycin resistant R712 as compared to susceptible S613, although $PAP_{248-286}$ is active against both at physiological concentrations (Figure 4.4b). This result was somewhat unexpected given that genome sequencing and lipid profiling have shown that R712 gains resistance by modifying its cell membrane to decrease the anionic phospholipid content (28–30), but it suggests instead that electrostatic membrane interactions may not drive $PAP_{248-286}$'s anti-biofilm activity. It is important to note that the MtP biofilm assay was only run with R712 once. However, if the lack of cross-resistance holds, this could be an interesting result and direction for future studies.

This work introduces many new and exciting questions. What causes the discrepancy between potent lipid membrane disruption *in vitro* and apparent lack of direct antimicrobial activity with bacteria? What is the oligomeric state of $PAP_{248-286}$ in these experiments? What is the oligomeric state that is responsible for the biofilm inhibition activity? In these experiments $PAP_{248-286}$ is added as a monomer, but it is known that bacterial and lipid membranes can accelerate amyloid formation (31–33). Also, why is $PAP_{248-286}$ active against *E. faecalis* and not *S. aureus*? Does membrane fluidity affect $PAP_{248-286}$'s anti-biofilm activity? What is the mechanism by which $PAP_{248-286}$ inhibits biofilm formation of both daptomycin resistant and susceptible *E. faecalis*? Does addition of $PAP_{248-286}$ monomer also result in bacterial agglutination? Answering these questions could improve our understanding of the role for $PAP_{248-286}$ in innate immunity and could also potentially inform the design of future antimicrobials against multiple drug-resistant pathogens.

4.3 MATERIALS AND METHODS

4.3.1 *Materials:*

1-palmitoyl-2-oleoyl-glycero-3-phosphocholine (POPC) and 1-palmitoyl-2-oleoyl-sn-glycero-3-phospho-(1'-rac-glycerol) (POPG) were purchased from Avanti Polar Lipids, Inc. (Alabaster, AL) as a powder. Unless specified otherwise, all other reagents were purchased from Thermo Fisher Scientific (Waltham, MA) and were ACS reagent grade or better.

4.3.2 *$PAP_{248-286}$ preparation:*

Synthetic $PAP_{248-286}$ was purchased from Genscript (Piscataway, NJ) and New England Peptides (Gardner, MA). Peptide was dissolved as received in Tris buffer (20 mM Tris, 100 mM NaCl, pH 7.4) or MilliQ water, flash frozen, and stored at -80°C. The final concentration of $PAP_{248-286}$ stock was determined by absorbance at 280 nm. For $PAP_{248-286}$ treated with hexafluoroisopropanol (HFIP), $PAP_{248-286}$ was dissolved in HFIP at 1 mg/mL, incubated at room temperature, and aliquoted, followed by removal of residual solvent with a Savant SC210A SpeedVac Concentrator with in-line Savant RVT5105 Ultra-low Temp Refrigerated Vapor Trap (Thermo Fisher Scientific). Aliquots of dried, HFIP-treated $PAP_{248-286}$ were stored at -20°C and resuspended in Tris buffer immediately prior to experiments.

4.3.3 *Dynamic light scattering (DLS):*

DLS was used to assess the effect of different peptide treatments on the oligomeric state of $PAP_{248-286}$ and the presence of large aggregates. For this experiment, DLS measurements on aliquots of thawed 1 mg/mL $PAP_{248-286}$ in Tris buffer, 1 mg/mL HFIP-treated $PAP_{248-286}$ brought up in Tris buffer, and 1 mg/mL $PAP_{248-286}$ filtered through a 0.22 μm syringe filter were collected.

Aliquots from the same samples were then centrifuged on a Sorvall Legend 21R at 21100*g* at 4°C for 30 minutes and DLS measurements were collected again. For each measurement, samples were added into a 1 µL Quartz Cuvette (Wyatt Technology, Goleta, CA) and measurements were collected with a DynaPro NanoStar (Wyatt Technology). Ten to fifteen 10-second acquisitions were measured at 25°C and averaged. The resulting average autocorrelation curves were then transferred to GraphPad Prism (GraphPad, San Diego, CA) where the curves were normalized and plotted.

4.3.4 *Size-exclusion chromatography multi-angle light scattering (SEC-MALS):*

Prior to use, the SEC-MALS was equilibrated with twice filtered 150 mM NaPi buffer and calibrated with 4 mg/mL BSA. $PAP_{248-286}$ was dissolved in Tris buffer at 3 mg/mL and centrifuged at 25000*g* on an Eppendorf Centrifuge 5417R (Eppendorf North America, Hauppauge, NY) for 10 minutes. The centrifuged $PAP_{248-286}$ solution was injected onto a Sepax SRT-C SEC 300 (Sepax Technologies, Newark, DE) column and separated by high pressure liquid chromatography (HPLC) (Agilent Technologies, Santa Clara, CA) with in line miniDAWN TREOS MALS detector and Optilab T-rEX refractometer (Wyatt Technology). The refractive index (RI) was set to 0.185 and the molecular mass was calculated in the ASTRA software package (Wyatt Technology). The data was transferred to GraphPad Prism (GraphPad) for plotting.

4.3.5 *Liposome preparation:*

POPG and 1:1 POPC:POPG (mol:mol) liposomes for FCS experiments were prepared in tris buffer as in section 2.3.3. Calcein-filled 1:1 POPC:POPG liposomes for fibril leakage experiments were prepared as in section 3.3.3, except the buffer that the lipid films were brought up in was a PBS buffer containing 10 mM Na_2HPO_4, 1.8 mM KH_2PO_4, 2.7 mM KCl, 0.3 mM

EDTA, and 70 mM calcein (MP Biomedicals, Irvine, CA) at pH 7.4. Rehydrated lipid films were freeze-thawed, extruded, separated from excess calcein, and dialyzed against PBS buffer without calcein (137 mM NaCl, 2.7 mM KCl, 10 mM Na_2HPO_4, 1.8 mM NaH_2PO_4, 0.3 mM EDTA, pH 7.4). Since the buffer contained phosphate, the concentration was unable to be quantified with the same "Determination of Total Phosphorous" analytical procedure detailed in section 2.3.3. Therefore, the static light scattering of the calcein-filled liposomes in PBS was measured on a DynaPro NanoStar (Wyatt Technology) DLS and compared to a standard curve created from liposomes of known concentration made in the HEPES buffer.

4.3.6 *Fluorescence correlation spectroscopy (FCS):*

$PAP_{248-286}$ was labeled with Alexa Fluor 488 NHS Ester and liposome binding experiments were performed as in the "fluorescence correlation spectroscopy" section of 2.3.11. The only difference for these experiments is that the amount of unlabeled $PAP_{248-286}$ was varied from 2 μM to 5 μM and 10 μM for both POPG and 1:1 POPC:POPG lipid compositions. The data were analyzed in the same manner as in section 2.3.11.

4.3.7 *ThT monitoring of SEVI fibril formation:*

SEVI fibrils were formed and their formation was monitored by ThT fluorescence in a manner similar to section 2.3.9. Briefly, 10 mg/mL $PAP_{248-286}$ was prepared in MilliQ water and diluted to 5 mg/mL in a 2x PBS buffer (274 mM NaCl, 5.4 mM KCl, 20 mM Na_2HPO_4, 3.6 mM KH_2PO_4, pH 7.4). The 5 mg/mL solution of $PAP_{248-286}$ in PBS buffer was centrifuged at 21100*g* at 4°C for 30 minutes in a Sorvall Legend 21R microcentrifuge (Thermo Fisher Scientific) to remove any aggregates. Some of the remaining solution was removed for concentration determination by its absorbance at 280 nm to account for loss of peptide during sample preparation.

The remaining solution was agitated 1200 RPM on an Eppendorf Thermomixer C (Eppendorf) at 37°C. At each time point, the background fluorescence (excitation at 440 nm and emission at 482 nm) of 25 μM ThT solution in PBS buffer was subtracted from the fluorescence of the ThT solution in the presence ~10 μM fibril formation reaction on a Molecular Devices Spectramax Gemini EM (Molecular Devices, San Jose, CA) plate reader. An aliquot of the fibril formation reaction at each timepoint was flash frozen and stored at -80°C until ready for use in fibril leakage experiments. Tests were done to verify that freezing the fibrils does not dramatically affect the ThT fluorescence. For the correlation with fraction leaked plot, the ThT signal was normalized.

4.3.8 *Fibril leakage kinetics:*

First, the monomer concentration required to cause about 50% leakage of 20 μM 1:1 POPC:POPG liposomes was determined. To do this, liposome stocks were diluted to 20 μM in PBS buffer, added to a 96-well plate (Corning 3651, Corning, NY), sealed with clear polyolefin sealing tape (Thermo Fisher Scientific), and placed into a BioTek Synergy HTX plate reader (BioTek, Winooski, VT). The liposomes were equilibrated and monitored at 25°C for 20 minutes with linear shaking at 567 cpm for 5 seconds followed by measurement of the calcein fluorescence in each well using a 485 nm excitation and 528 nm emission each minute. During this time, 20x the desired concentrations of $PAP_{248-286}$ were prepared. After the 20 minutes, the plate was removed from the BioTek plate reader and 10 μL of the 20x $PAP_{248-286}$ stocks were added to the 20 μM equilibrated liposome solutions. The plate was returned to the plate reader, shaken orbitally at 425 cpm for 30 seconds, and the calcein fluorescence was measured every minute following a 5 second linear shake for 2 more hours. PBS buffer or 0.05% triton were added as 0% and 100% leaked controls, respectively, and the fraction leaked at each time point was calculated using the equation:

$$F(t) = \frac{I(t) - I_b(t)}{I_{max} - I_b(t)}, \quad (4.1)$$

where *F(t)* is the fraction leaked at each time point, *I(t)* and $I_b(t)$ are the fluorescence intensity of the sample and the buffer control at each time point, respectively, and I_{max} is the fluorescence intensity of liposomes with 0.05% triton. From this analysis, it was concluded that 2 μM $PAP_{248-286}$ monomer causes about 50% leakage of 20 μM 1:1 POPC:POPG liposomes.

The same leakage experiment and analysis was then repeated for SEVI fibril leakage, but here previously prepared SEVI fibril formation timepoints were thawed and prepared at 20x the desired concentration, diluted to 2 μM upon addition to 20 μM equilibrated liposomes, and observed over 2 hours.

4.3.9 *Minimum inhibitory concentration (MIC) and microtiter plate (MtP) biofilm assays:*

Organisms were streaked out onto tryptic soy agar and incubated overnight at 37°C. For MIC experiments, the organisms used include gram negative *E. coli* (K-12) (34), a clinically derived isogenic strain pair of daptomycin susceptible *E. faecalis* (S613) and daptomycin resistant *E. faecalis* (R712) (29), a well characterized strain of methicillin-resistant *S. aureus* (MRSA) (N315) (35), and *N315* that was passaged in escalating concentrations of daptomycin by Dr. Brian Werth to select for a mutant that has a 64-fold increase in MIC (N315 Dap-8) (28). For MtP biofilm experiments, the commonly used laboratory strain *S. aureus* (SH1000) (36), daptomycin susceptible *E. faecalis* (S613), and daptomycin resistant *E. faecalis* (R712) were used.

The next day a 0.5-1 McFarland solution of the organism in saline solution was prepared and diluted 1:100 into the appropriate media (Mueller-Hinton Broth for MICs and 1% glucose supplemented tryptic soy broth for biofilm quantification). 25 μL of media was added to all of the wells of a sterile 96-well, microtiter plate (round bottom for MICs, flat bottom for biofilm

quantification assays). A $PAP_{248-286}$ stock was prepared at 8x the final desired concentration in tris buffer, and 25 µL of this stock was added to the first column of wells. Two-fold serial dilutions were made by removing 25 µL from the first column, adding it to the next column, mixing that solution, and then removing 25 µL and repeating the process. One column was always left without any drug (growth control) and one did not have any bacteria or drug (media control). For MtP biofilm assays, additional buffer controls were made to assess the effect of vehicle on biofilm formation. 50 µL of media was then added to all of the wells, followed by the addition of 25 µL of the organism stock to all wells except the media control. The plates were then incubated at 37°C for approximately 16-24 hours.

After incubation, the MIC of $PAP_{248-286}$ with each organism was assessed by determining the lowest concentration of drug in which bacterial growth could not be detected by visual inspection. As a positive control, the MIC of the antibiotic vancomycin with N315 was determined to be the expected 0.5 mg/mL. For the MtP biofilm assay, the contents were emptied into a waste container. To remove residual planktonic bacteria, the plate was then washed by submersion into deionized water, emptied, and tapped onto paper towels to remove excess water. This process was repeated three more times and air dried. 200 µL of 0.1% crystal violet solution was then added to all of the wells, incubated for 10 minutes at room temperature, and then emptied from the wells. The plate was then washed using the same method as before and left for at least 30 minutes to dry completely. 200 µL of 33% acetic acid was then added to each well, mixed, transferred to a new plate, and the absorbance at 542 nm was measured on a Benchmark Microplate Reader (Bio-Rad, Hercules, CA). The fraction adhered was determined by subtracting the average absorbance of the media control and then dividing by the average absorbance of the growth control.

4.4 ACKNOWLEDGEMENTS:

I would like to thank Professor Miklos Guttman for his help and advice with the SEC-MALS analysis on $PAP_{248-286}$, Professor Brian Werth for his expertise, advice, and engaging discussions about the antimicrobial activity of $PAP_{248-286}$, and Dr. Eri Nakatani Webster for teaching me how to run the MIC and MtP biofilm assays. I would also like to thank Supriya Ravishankar for preparing some buffers and calcein-filled liposomes for fibril leakage experiments.

4.5 TABLES & FIGURES

Table 4.1: $PAP_{248-286}$ does not display direct antimicrobial activity against a panel of bacteria as determined by MIC.

Organism	Strain	MIC (μg/mL)
E. coli	K12	> 512
E. faecalis	S613	> 512
E. faecalis	R712	> 512
S. aureus	N315	> 512
S. aureus	N315 Dap 8	~ 512

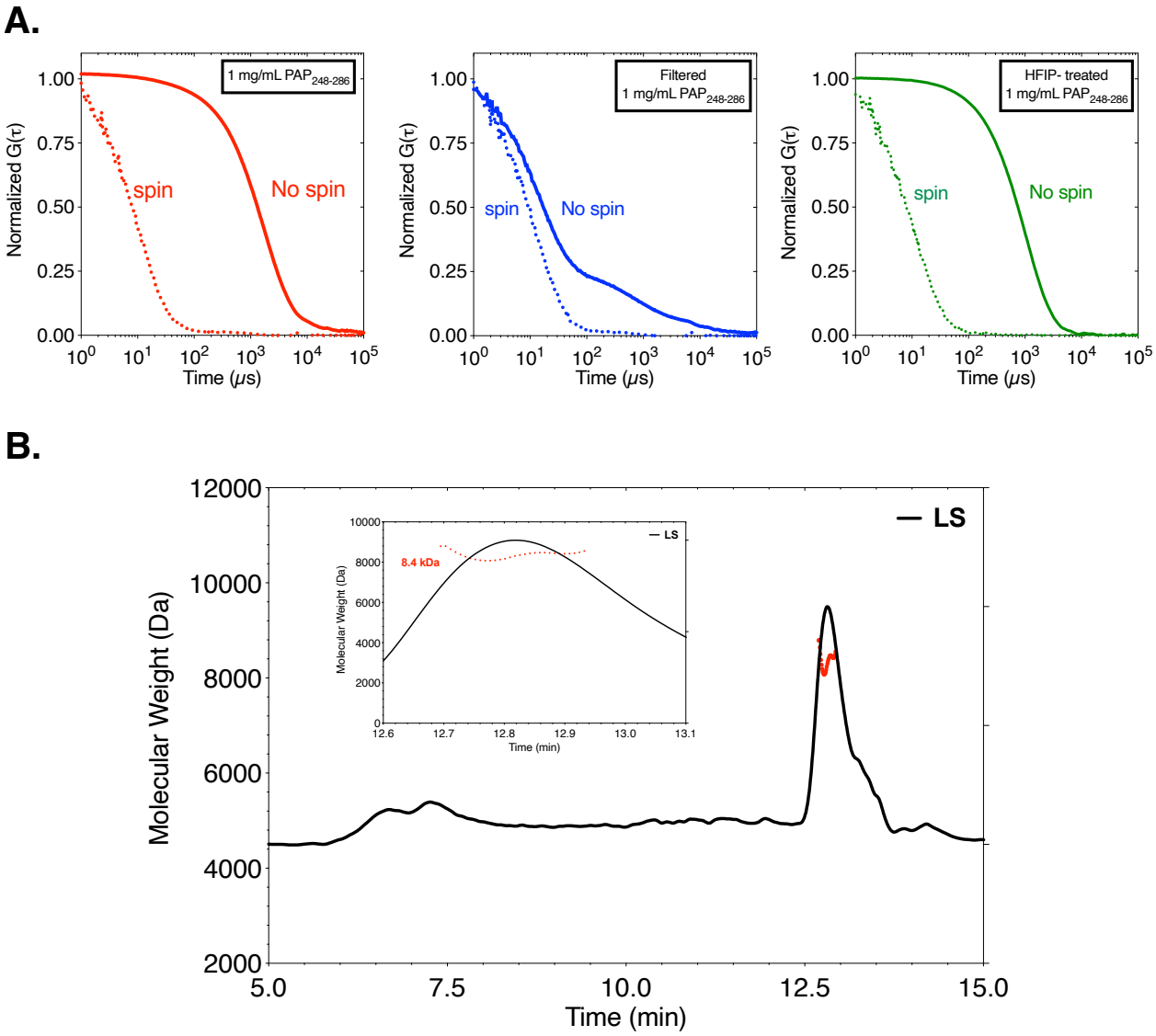

Figure 4.1: $PAP_{248-286}$ is oligomeric and forms large aggregates in solution.

(A) Pairwise comparisons of methods for removing large oligomers and aggregates as assessed by autocorrelation curves from dynamic light scattering. The curves show that for 1 mg/mL $PAP_{248-286}$ in buffer (left), 1 mg/mL $PAP_{248-286}$ filtered through a 0.22 µm syringe filter, and 1 mg/mL HFIP-treated $PAP_{248-286}$, centrifuging the solution for 30 minutes at 21100*g* is the most effect way to remove large aggregates. (B) SEC-MALS trace showing the calculated molecular weight (MW) in red over the light scattering (LS) curve in black. With a monomer MW of 4.55 kDa, a molecular weight of 8.4 kDa would suggest that $PAP_{248-286}$ is a dimer in solution. However, it should be noted that $PAP_{248-286}$ came off the column near the buffer front making it hard to get an accurate molecular weight.

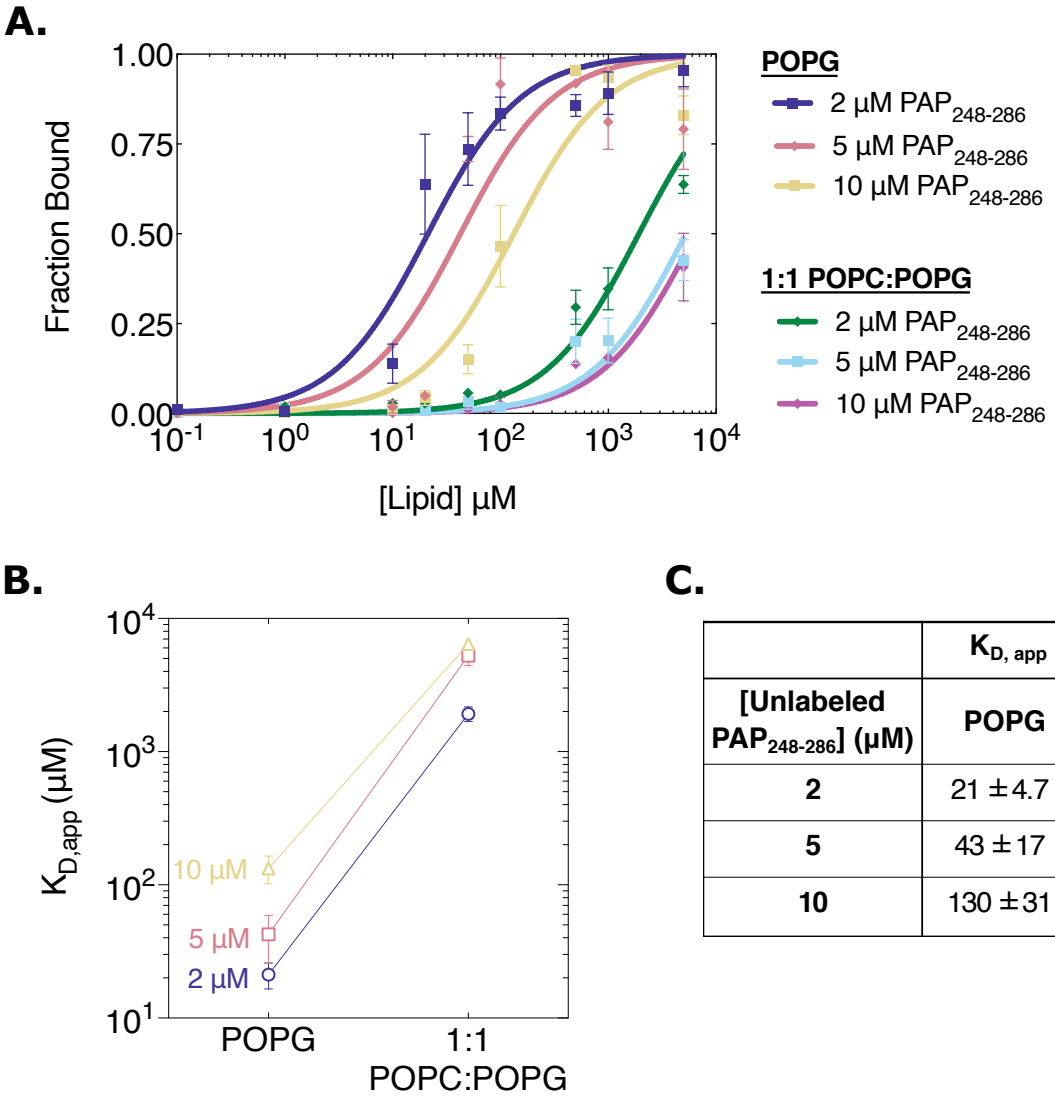

C.

	$K_{D,\,app}$ ± SEM (µM)	
[Unlabeled $PAP_{248-286}$] (µM)	POPG	1:1 POPC:POPG
2	21 ± 4.7	1900 ± 240
5	43 ± 17	5300 ± 830
10	130 ± 31	6400 ± 590

Figure 4.2: $PAP_{248-286}$ appears to display modest negative cooperativity in binding to both POPG and 1:1 POPC:POPG liposomes.

Binding curves were created from FCS titrations of POPG with 2 µM (purple square), 5 µM (pink diamond), and 10 µM (yellow square) unlabeled $PAP_{248-286}$ and 1:1 POPC:POPG with 2 µM (green diamond), 5 µM (blue square), and 10 µM (magenta diamond) unlabeled $PAP_{248-286}$ (A). The solid lines show the binding curve calculated from a one site binding model as in section 2.3.11. A plot (B) and the corresponding numerical values (C) of the resulting apparent binding affinities ($K_{D,app}$) for each of these conditions shows that the $K_{D,app}$ increases slightly with increasing concentrations of $PAP_{248-286}$, suggesting modest negative cooperativity for both lipid compositions. Data are shown as the mean and standard error of the mean (SEM) of at least three independent experiments for all conditions except for 10 µM unlabeled $PAP_{248-286}$ with 1:1 POPC:POPG liposomes which is the result of two independent experiments.

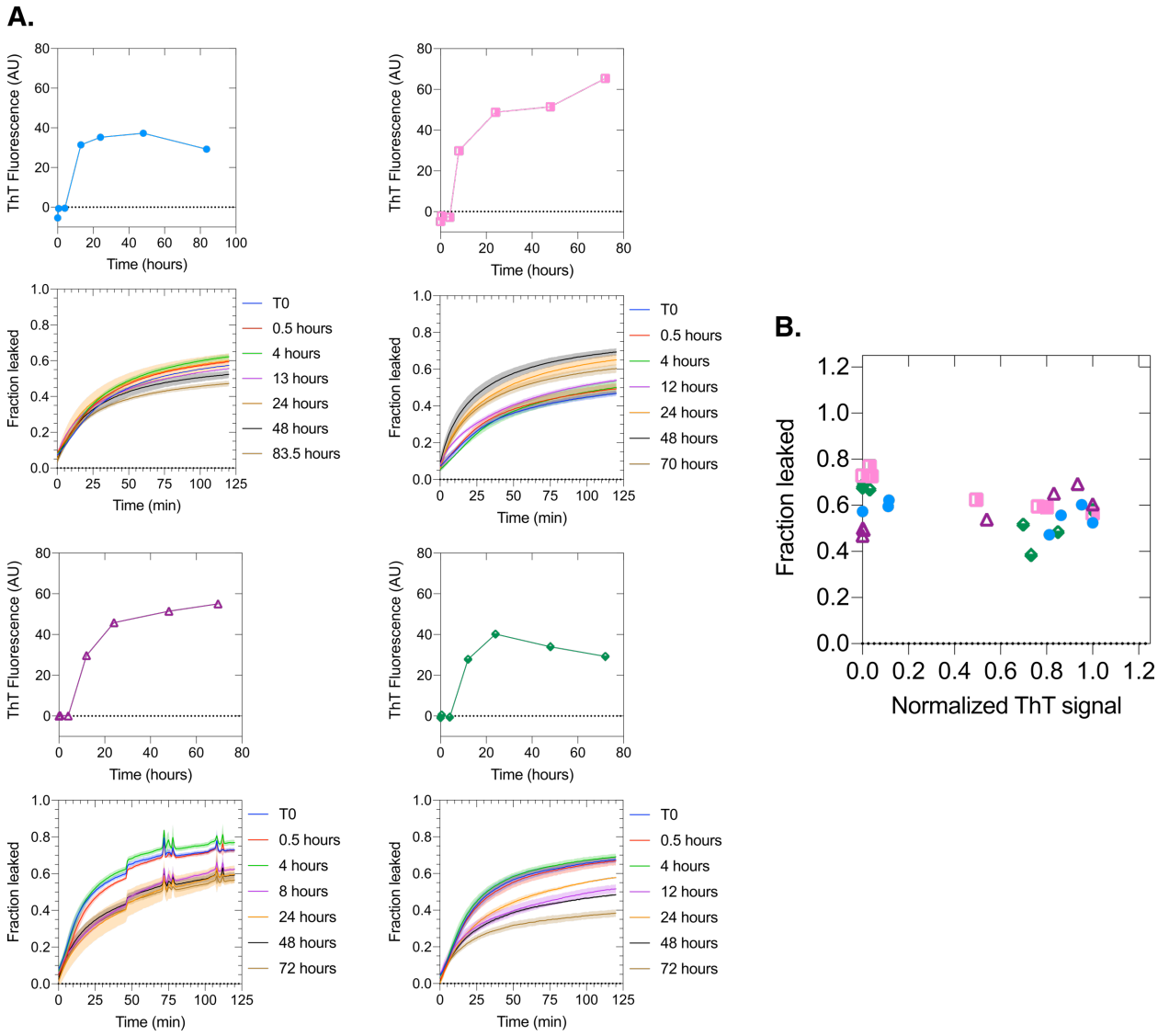

Figure 4.3: Presence of SEVI fibrils does not seem to affect liposome leakage.

(A) For each of the four independent experiments, the top panel shows ThT fluorescence of time points from the SEVI fibril formation reaction while the bottom panel shows the liposome leakage kinetics with aliquots taken at these time points. For all ThT curves, each point shows the mean of duplicate measurements. For all liposome leakage kinetics, lines and the shaded area indicate the mean and standard deviation of triplicate measurements. It should be noted that the spikes in the liposome leakage kinetics in the bottom left panel are artifacts due to lamp issues in the plate reader. (B) Plot comparing the fraction leaked at the end of the kinetic measurement to the normalized ThT signal with different colors and shading corresponding to each of the independent replicates from (A). This shows that there is not a strong or consistent correlation between ThT signal and fraction of calcein leaked.

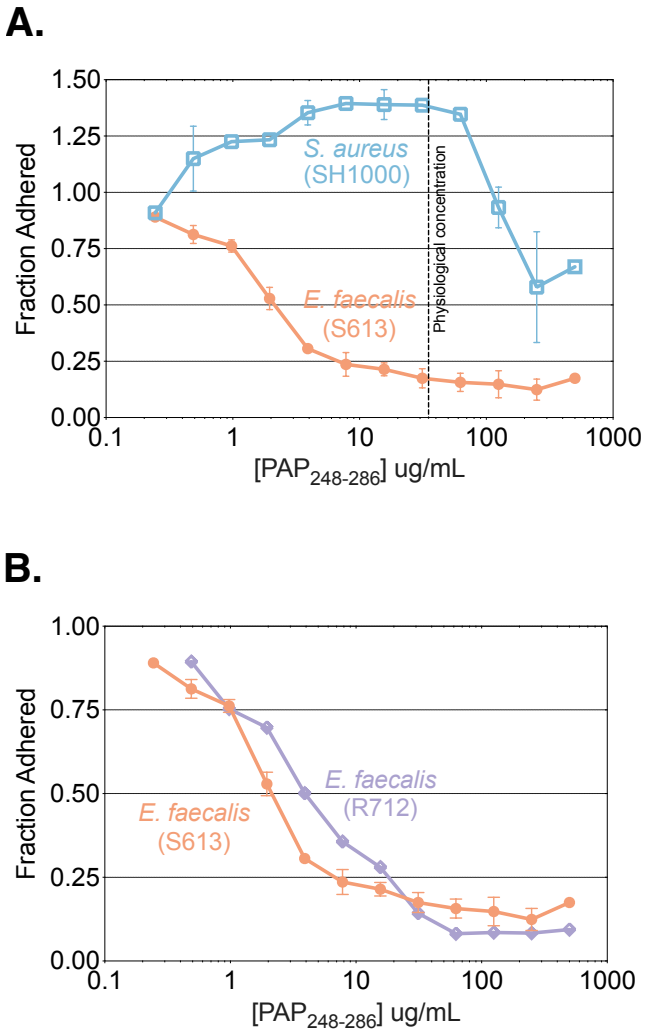

Figure 4.4: $PAP_{248-286}$ inhibits biofilm formation of some organisms.

(A) MtP biofilm inhibition assay of $PAP_{248-286}$ with *E. faecalis* (S613) (orange, filled circles) and *S. aureus* (SH1000) (blue, open squares) shows that $PAP_{248-286}$ is active against *E. faecalis* and not *S. aureus*. Error bars represent mean and standard deviation of two independent experiments and the dashed vertical line represents the physiological concentration of $PAP_{248-286}$, 35 µg/mL (37). (B) MtP biofilm inhibition assay of $PAP_{248-286}$ with daptomycin-susceptible *E. faecalis* (S613) (orange, filled circles) and daptomycin-resistant *E. faecalis* (R712) (purple diamonds) suggests that $PAP_{248-286}$ may be slightly less active against the daptomycin-resistant strain, though this effect is not very large. The data from *E. faecalis* (S613) is the same as in (A). For *E. faecalis* (R712), points represent the mean of triplicate replicates from a single experiment.

4.6 REFERENCES

1. Arnold, F., J. Schnell, O. Zirafi, C. Stürzel, C. Meier, T. Weil, L. Ständker, W.-G. Forssmann, N.R. Roan, W.C. Greene, F. Kirchhoff, and J. Münch. 2012. Naturally Occurring Fragments from Two Distinct Regions of the Prostatic Acid Phosphatase Form Amyloidogenic Enhancers of HIV Infection. *J. Virol.* 86:1244–1249.
2. Castellano, L.M., S.M. Bart, V.M. Holmes, D. Weissman, and J. Shorter. 2015. Repurposing Hsp104 to Antagonize Seminal Amyloid and Counter HIV Infection. *Chem. Biol.* 22:1074–1086.
3. Capone, R., F.G. Quiroz, P. Prangkio, I. Saluja, A.M. Sauer, M.R. Bautista, R.S. Turner, J. Yang, and M. Mayer. 2009. Amyloid-β-induced ion flux in artificial lipid bilayers and neuronal cells: Resolving a controversy. *Neurotox. Res.* 16:1–13.
4. Zhang, M., T. Peyear, I. Patmanidis, D. V. Greathouse, S.J. Marrink, O.S. Andersen, and H.I. Ingólfsson. 2018. Fluorinated Alcohols' Effects on Lipid Bilayer Properties. *Biophys. J.* 115:679–689.
5. Nichols, M.R., M.A. Moss, D.K. Reed, S. Cratic-McDaniel, J.H. Hoh, and T.L. Rosenberry. 2005. Amyloid-β protofibrils differ from amyloid-β aggregates induced in dilute hexafluoroisopropanol in stability and morphology. *J. Biol. Chem.* 280:2471–2480.
6. Ryan, T.M., J. Caine, H.D.T. Mertens, N. Kirby, J. Nigro, K. Breheney, L.J. Waddington, V.A. Streltsov, C. Curtain, C.L. Masters, and B.R. Roberts. 2013. Ammonium hydroxide treatment of Aβ produces an aggregate free solution suitable for biophysical and cell culture characterization. *PeerJ*. 2013:e73.
7. Knight, J.D., J.A. Hebda, and A.D. Miranker. 2006. Conserved and cooperative assembly of membrane-bound α-helical states of islet amyloid polypeptide. *Biochemistry*. 45:9496–9508.
8. Huang, H.W. 2006. Molecular mechanism of antimicrobial peptides: The origin of cooperativity. *Biochim. Biophys. Acta - Biomembr.* 1758:1292–1302.
9. Hebda, J. a, and A.D. Miranker. 2009. The interplay of catalysis and toxicity by amyloid intermediates on lipid bilayers: insights from type II diabetes. *Annu. Rev. Biophys.* 38:125–52.
10. Rautenbach, M., G.D. Gerstner, N.M. Vlok, J. Kulenkampff, and H. V. Westerhoff. 2006. Analyses of dose-response curves to compare the antimicrobial activity of model cationic α-helical peptides highlights the necessity for a minimum of two activity parameters. *Anal. Biochem.* 350:81–90.
11. Valincius, G., F. Heinrich, R. Budvytyte, D.J. Vanderah, D.J. McGillivray, Y. Sokolov, J.E. Hall, and M. Lösche. 2008. Soluble amyloid β-oligomers affect dielectric membrane properties by bilayer insertion and domain formation: Implications for cell toxicity. *Biophys. J.* 95:4845–4861.
12. Beschiaschvili, G., and J. Seelig. 1990. Melittin Binding to Mixed Phosphatidylglycerol/Phosphatidylcholine Membranes. *Biochemistry*. 29:52–58.
13. Ke, P.C., R. Zhou, L.C. Serpell, R. Riek, T.P.J. Knowles, H.A. Lashuel, E. Gazit, I.W. Hamley, T.P. Davis, M. Fändrich, D.E. Otzen, M.R. Chapman, C.M. Dobson, D.S. Eisenberg, and R. Mezzenga. 2020. Half a century of amyloids: Past, present and future. *Chem. Soc. Rev.* 49:5473–5509.
14. Bucciantini, M., E. Giannoni, F. Chiti, F. Baroni, L. Formigli, J. Zurdo, N. Taddei, G. Ramponi, C.M. Dobson, and M. Stefani. 2002. Inherent toxicity of aggregates implies a common mechanism for protein misfolding diseases. *Nature*. 416:507–511.
15. Caughey, B., and P.T. Lansbury. 2003. Protofibrils , Pores, Fibrils, and Neurodegeneration: Separating the Responsible Protein Aggregates from The Innocent Bystanders. *Annu. Rev. Neurosci.* 26:267–298.

16. Baldwin, A.J., T.P.J. Knowles, G.G. Tartaglia, A.W. Fitzpatrick, G.L. Devlin, S.L. Shammas, C.A. Waudby, M.F. Mossuto, S. Meehan, S.L. Gras, J. Christodoulou, S.J. Anthony-Cahill, P.D. Barker, M. Vendruscolo, and C.M. Dobson. 2011. Metastability of Native Proteins and the Phenomenon of Amyloid Formation. *J. Am. Chem. Soc*. 133.

17. Biancalana, M., and S. Koide. 2010. Molecular mechanism of Thioflavin-T binding to amyloid fibrils. *Biochim. Biophys. Acta - Proteins Proteomics*. 1804:1405–1412.

18. Qiao, X., J. Jeon, A.L. Cole, J.O. Matos, S. Bautista, J. Castillo, I. Hung, Z. Gan, S.A. Tatulian, A.M. Cole, and B. Chen. 2015. Morphology-dependent HIV-enhancing effect of semen-derived enhancer of viral infection. *Biophys. J.* 108:2028–2037.

19. Wimley, W.C. 2010. Describing the mechanism of antimicrobial peptide action with the interfacial activity model. *ACS Chem. Biol.* 5:905–917.

20. Kagan, B.L., H. Jang, R. Capone, F. Teran Arce, S. Ramachandran, R. Lal, and R. Nussinov. 2012. Antimicrobial properties of amyloid peptides. *Mol. Pharm.* 9:708–717.

21. Easterhoff, D., F. Ontiveros, L.R. Brooks, Y. Kim, B. Ross, J.N. Silva, J.S. Olsen, C. Feng, D.J. Hardy, P.M. Dunman, and S. Dewhurst. 2013. Semen-derived enhancer of viral infection (SEVI) binds bacteria, enhances bacterial phagocytosis by macrophages, and can protect against vaginal infection by a sexually transmitted bacterial pathogen. *Antimicrob. Agents Chemother.* 57:2443–2450.

22. Kumar, D.K. V., S.H. Choi, K.J. Washicosky, W.A. Eimer, S. Tucker, J. Ghofrani, A. Lefkowitz, G. McColl, L.E. Goldstein, R.E. Tanzi, and R.D. Moir. 2016. Amyloid-B peptide protects against microbial infection in mouse and worm models of Alzheimers disease. *Sci. Transl. Med.* 8:340ra72-340ra72.

23. Wang, G., B. Mishra, K. Lau, T. Lushnikova, R. Golla, and X. Wang. 2015. Antimicrobial peptides in 2014. *Pharmaceuticals*. 8:123–150.

24. Yasir, M., M.D.P. Willcox, and D. Dutta. 2018. Action of antimicrobial peptides against bacterial biofilms. *Materials (Basel).* 11.

25. 2017. Cubicin: Highlights of Prescribing Information. Whitehouse Station, NJ: Merck Sharp and Dohme Corp.

26. Chen, C.H., and T.K. Lu. 2020. Development and Challenges of Antimicrobial Peptides for Therapeutic Applications. *Antibiotics*. 9:24.

27. Lazzaro, B.P., M. Zasloff, and J. Rolff. 2020. Antimicrobial peptides: Application informed by evolution. *Science (80-.).* 368.

28. Hines, K.M., A. Waalkes, K. Penewit, E.A. Holmes, S.J. Salipante, B.J. Werth, and L. Xu. 2017. Characterization of the Mechanisms of Daptomycin Resistance among Gram-Positive Bacterial Pathogens by Multidimensional Lipidomics. *mSphere*. 2.

29. Arias, C.A., D. Panesso, D.M. McGrath, X. Qin, M.F. Mojica, C. Miller, L. Diaz, T.T. Tran, S. Rincon, E.M. Barbu, J. Reyes, J.H. Roh, E. Lobos, E. Sodergren, R. Pasqualini, W. Arap, J.P. Quinn, Y. Shamoo, B.E. Murray, and G.M. Weinstock. 2011. Genetic Basis for In Vivo Daptomycin Resistance in Enterococci. *N. Engl. J. Med.* 365:892–900.

30. Mishra, N.N., A.S. Bayer, T.T. Tran, Y. Shamoo, E. Mileykovskaya, W. Dowhan, Z. Guan, and C.A. Arias. 2012. Daptomycin Resistance in Enterococci Is Associated with Distinct Alterations of Cell Membrane Phospholipid Content. *PLoS One*. 7:e43958.

31. Gorbenko, G.P., and P.K.J. Kinnunen. 2006. The role of lipid-protein interactions in amyloid-type protein fibril formation. *Chem. Phys. Lipids*. 141:72–82.

32. Zhao, H., E.K.J. Tuominen, and P.K.J. Kinnunen. 2004. Formation of amyloid fibers triggered by phosphatidylserine-containing membranes. *Biochemistry*. 43:10302–10307.

33. Torrent, M., D. Pulido, M.V. Nogués, and E. Boix. 2012. Exploring New Biological Functions of Amyloids: Bacteria Cell Agglutination Mediated by Host Protein Aggregation. *PLoS Pathog.* 8:1–8.

34. Blattner, F.R., G. Plunkett, C.A. Bloch, N.T. Perna, V. Burland, M. Riley, J. Collado-Vides, J.D. Glasner, C.K. Rode, G.F. Mayhew, J. Gregor, N.W. Davis, H.A. Kirkpatrick, M.A. Goeden, D.J. Rose, B. Mau, and Y. Shao. 1997. The complete genome sequence of Escherichia coli K-12. *Science (80-.).* 277:1453–1462.

35. Kuroda, M., T. Ohta, I. Uchiyama, T. Baba, H. Yuzawa, I. Kobayashi, N. Kobayashi, L. Cui, A. Oguchi, K.I. Aoki, Y. Nagai, J.Q. Lian, T. Ito, M. Kanamori, H. Matsumaru, A. Maruyama, H. Murakami, A. Hosoyama, Y. Mizutani-Ui, N.K. Takahashi, T. Sawano, R.I. Inoue, C. Kaito, K. Sekimizu, H. Hirakawa, S. Kuhara, S. Goto, J. Yabuzaki, M. Kanehisa, A. Yamashita, K. Oshima, K. Furuya, C. Yoshino, T. Shiba, M. Hattori, N. Ogasawara, H. Hayashi, and K. Hiramatsu. 2001. Whole genome sequencing of meticillin-resistant Staphylococcus aureus. *Lancet*. 357:1225–1240.

36. Horsburgh, M.J., J.L. Aish, I.J. White, L. Shaw, J.K. Lithgow, and S.J. Foster. 2002. δb modulates virulence determinant expression and stress resistance: Characterization of a functional rsbU strain derived from Staphylococcus aureus 8325-4. *J. Bacteriol.* 184:5457–5467.

37. Münch, J., E. Rücker, L. Ständker, K. Adermann, C. Goffinet, M. Schindler, S. Wildum, R. Chinnadurai, D. Rajan, A. Specht, G. Giménez-Gallego, P.C. Sánchez, D.M. Fowler, A. Koulov, J.W. Kelly, W. Mothes, J.C. Grivel, L. Margolis, O.T. Keppler, W.G. Forssmann, and F. Kirchhoff. 2007. Semen-Derived Amyloid Fibrils Drastically Enhance HIV Infection. *Cell*. 131:1059–1071.

VITA

EDUCATION

Clarkson University, Potsdam, NY, 2014
B.S. in Biomolecular Sciences (with Honors), Mathematics Minor

University of Washington, Seattle, WA, 2021
Ph.D. in Medicinal Chemistry

PUBLICATIONS

Vane, E.W., and A. Nath. 2021. Probing the vesicle leakage mechanism of $PAP_{248-286}$ with fluorescence lifetime distribution analysis. [in preparation]

Vane, E.W., S. He, L. Maibaum, and A. Nath. 2020. Rapid Formation of Peptide/Lipid Coaggregates by the Amyloidogenic Seminal Peptide $PAP_{248-286}$. *Biophys. J.* 119:924–938.

CONFERENCES

64th Annual Meeting of the Biophysical Society, San Diego, CA, February 2020
Poster presentation: "Membrane Disruption and Peptide/Lipid Co-assembly by the Amyloid-forming Peptide, $PAP_{248-286}$"

33rd Annual Symposium of the Protein Society, Seattle, WA, July 2019
Poster presentation: "Discovery and Characterization of an Amyloid-like $PAP_{248-286}$/Lipid Co-assembly"

2018 ASBMB Annual Meeting, San Diego, CA, April 2018
Poster presentation: "Investigating Effects and Determinants of $PAP_{248-286}$-Membrane Interactions: Membrane Leakage and Peptide/Lipid Co-Aggregation"

31st Annual Symposium of the Protein Society, Montreal, CA, July 2017
Poster presentation: "Investigating Determinants of the Membrane Activities of $PAP_{248-286}$"